

Technische Universität München  
Lehrstuhl für Theoretische Chemie

**Hydrocarbon conversion over transition metal catalysts:  
A mechanistic study from first-principles calculations**

Zhijian Zhao

Vollständiger Abdruck der von der Fakultät für Chemie der Technischen Universität München zur Erlangung des akademischen Grades eines

Doktors der Naturwissenschaften (Dr. rer. nat.)

genehmigten Dissertation.

Vorsitzender:

Univ.-Prof. Dr. K. Köhler

Prüfer der Dissertation:

1. Univ.-Prof. Dr. Dr. h.c. N. Rösch, i. R.

2. Univ.-Prof. Dr. J. A. Lercher

Die Dissertation wurde am 02.07.2012 bei der Technischen Universität München eingereicht und durch die Fakultät für Chemie am 04.09.2012 angenommen.



## Acknowledgment

First and foremost, I would like to thank my Doktorvater, Prof. Dr. Dr. h.c. Notker Rösch for giving me the opportunity to do my doctoral thesis in his research group. I am grateful for his support throughout these years. I learned a lot not only limited to the scientific area, but also on many other aspects, which a lot of other professors will not concern. Thank you! This is the most important four years of my life and I really grow up a lot during this abroad studying period. I believe this experience will help me in my whole life.

I would also like to thank Dr. Lyudmila V. Moskaleva for her guidance and helping me to improve my English, and Ass. Prof. Hristiyan A. Aleksandrov who had not only introduced me to this topic, but also taught me to run VASP code on various platforms. I thank to Dr. Alexander Genest and Dr. Benjami Martorell for the help in the frequency analysis topic; to Duygu Başaran and Cheng-chau Chiu for the daily discussions on my topic; to Dr. Sven Krüger for many administrative supports and scientific discussions; to Dr. Miraim Häberle, Dr. Agnes Mirescu, Ms. Barbara Asam and Ms. Elisabeth Wurm for many administrative supports.

I appreciate the camaraderie shared among the past and present research group members: Dr. Üzengi Olcay Aktürk, Dr. Ethem Aktürk, Chun-Ran Chang, Dr. Ion Chiorescu, Dr. Konstantina Damianos, Gopal Dixit, Dr. Wilhelm Eger, Dr. Virve Karttunen, Sergey M. Kozlov, Dr. Alena Kremleva, Bo Li, Shane Parker, Dr. Raghunathan Ramakrishnan, Dr. Rupashree Shyama Ray, Dr. Rémi Marchal, Dr. Juan Santana, Thomas Martin Soini, Dr. Jing Su, Dr. Egor Vladimirov, Yin Wu, Yun Zhang and those not mentioned here. They have not only made my stay here enjoyable, but also taught me many things.

I am grateful too, for the support from Deutsche Forschungsgemeinschaft (DFG) and Nanodesign of High Performance Catalysts (NanoCat). The staff from NanoCat was helpful during my stay in Germany.

Zhi-Jian Zhao

Garching, Germany

June 28, 2012



## **Zusammenfassung**

Das selektive Cracken von Naphthalenringen ist ein wichtiger Prozess in der modernen Erdölindustrie geworden, um die Cetanzahl von Dieselmotorkraftstoffen zu erhöhen. In dieser Arbeit wurden zwei Modellreaktionen, die Konversion von Ethylen zu Ethinyl und die Ringöffnungsreaktion von Methylcyclopentan (MCP), mit periodischen Dichtefunktionalrechnungen untersucht. Die Arbeit hat folgende Sachverhalte erfolgreich aufgeklärt: i) Der Mechanismus der Transformierung von Ethylen zu Ethinyl auf Pt(111). Die Reaktion durchläuft eine Serie von Hydrierungs-/Dehydrierungsschritten ohne direkte 1,2-H Umlagerungsreaktionen. ii) Der Partikelgrößeneffekt auf die Selektivität der durch geträgerte Pt, Rh, Ir oder Pd Partikel katalysierte MCP-Ringöffnung. Die Selektivität hängt von der Höhe der Barrieren für den C-C-Bindungsbruch auf der Terrasse oder an einer Stufe auf dem Reaktionsweg zu den drei Hexanisomeren ab.

## **Abstract**

Selective cracking of naphthenic rings to raise the cetane number of diesel fuels is an important issue for modern petroleum industry. In this thesis, two model reactions, ethylene conversion to ethynyl as well as ring-opening of methylcyclopentane (MCP), were examined using periodic density functional calculations. This work successfully clarified the following issues: i) the mechanism of transforming ethylene to ethynyl on Pt(111). The reaction comprises a series of hydrogenation / dehydrogenation steps, without direct 1,2-H shift reactions. ii) The particle-size effect on the selectivity of MCP ring-opening catalyzed by supported Pt, Rh, Ir or Pd particles. The selectivity depends on the C–C bond breaking barrier heights at terrace or step sites on the way to three isomeric hexanes.



# Hydrocarbon conversion over transition metal catalysts: A mechanistic study from first-principles calculations

<b>CHAPTER 1 INTRODUCTION .....</b>	<b>1</b>
<b>CHAPTER 2 COMPUTATIONAL APPROACH .....</b>	<b>4</b>
<b>CHAPTER 3 ETHYLENE TRANSFORMATIONS OVER PT(111).....</b>	<b>8</b>
3.1. BACKGROUND .....	8
3.1.1 <i>Experimental research</i> .....	8
3.1.2 <i>Previous theoretical research</i> .....	10
3.1.3 <i>Models in the current study</i> .....	11
3.2. STRUCTURE AND ENERGETICS OF SURFACE SPECIES AND TRANSITION STATES .....	11
3.2.1 <i>Structure and energetics of surface species</i> .....	11
3.2.2 <i>Transition State Structures for Ethylene Conversion to Ethylidyne</i> .....	18
3.2.3 <i>Coverage effect on the individual reactions</i> .....	24
3.3. THREE MECHANISMS OF ETHYLENE CONVERSION TO ETHYLIDYNE.....	25
3.3.1 <i>Reaction in the absence of hydrogen</i> .....	25
3.3.2 <i>Reaction under hydrogenation conditions.</i> .....	29
3.4. REMARK ON A SPECTROSCOPICALLY IDENTIFIED TRANSIENT INTERMEDIATE. ....	30
3.4.1 <i>C<sub>2</sub>H<sub>x</sub> (x = 3–4) on the Pt(111) surface</i> .....	32
3.4.2 <i>C<sub>2</sub>H<sub>x</sub> (x = 3–4) in organometallic clusters</i> .....	36
3.4.3 <i>Comparison between C<sub>2</sub>H<sub>x</sub> moieties (x = 3–4) on the surface and in a complex</i> .....	39
3.4.4 <i>Final remark on a spectroscopically identified transient intermediate</i> .....	41
3.5. SUMMARY .....	45
<b>CHAPTER 4 METHYLCYCLOPENTANE RING-OPENING REACTIONS.....</b>	<b>47</b>
4.1. INTRODUCTION.....	47
4.1.1 <i>Experimental research</i> .....	47
4.1.2 <i>Former theoretical studies</i> .....	50
4.1.3 <i>Reaction network investigated in the current study</i> .....	50
4.2. RING-OPENING REACTIONS CATALYZED BY PT .....	51
4.2.1 <i>Reactions on large Pt particles</i> .....	51
4.2.2 <i>Reactions on small Pt particles</i> .....	67
4.2.3 <i>Alternative reaction to form nHx on small Pt particles</i> .....	75
4.2.4 <i>Selectivity of the ring-opening on single-crystal surfaces</i> .....	80
4.2.5 <i>Selectivity of ring-opening products on supported Pt particles</i> .....	82
4.3. RING-OPENING REACTIONS CATALYZED BY RH, IR AND PD.....	83
4.3.1 <i>First dehydrogenation reaction (D1)</i> .....	84
4.3.2 <i>C–C bond breaking reactions</i> .....	86
4.3.3 <i>Activity on Pt, Pd, Ir, Rh surfaces</i> .....	92
4.3.4 <i>Particle size effect on the ring-opening products selectivity</i> .....	96
4.3.5 <i>Final comments on the particle size effect</i> .....	99
4.4. SUMMARY .....	101
<b>CHAPTER 5 SUMMARY OF THE THESIS.....</b>	<b>104</b>
<b>APPENDIX: LIST OF ABBREVIATIONS.....</b>	<b>108</b>
<b>REFERENCES .....</b>	<b>109</b>



# Chapter 1

## Introduction

Nowadays, an important issue for a lot of countries all over the world is to reduce the air pollution. Such pollution is harmful to the human health and to the local environment. A large part of air pollution is caused by modern transport systems. The combustion of fuels, e.g. gasoline, diesel, aviation fuel etc., not only generates the power for the transportation but also emits various kinds of pollutants, like nitrogen oxides, sulfur oxides, hydrocarbons, carbon monoxide and particulate matter (PM), to the atmosphere. For example, road transport is considered to be the main contributor to the emission of nitrogen dioxide and benzene in cities.<sup>1</sup> 30% of fine PM (less than 2.5  $\mu\text{m}$  in aerodynamic diameter) is also produced by the tailpipe emissions from road transport in urban areas.<sup>1</sup> Additionally, the efficiency of the transport system becomes an important issue due to the global warming caused by the accumulation of carbon dioxide which is produced by the combustion of fuels.

Therefore, it is expected that stricter requirements will be imposed on fuels regarding their content of sulfur and polynuclear aromatics, the content of lead for gasoline as well as the cetane number (CN) for diesel.<sup>1</sup> In the past several decades, the allowed maximum lead content in Europe has decreased from 0.15-0.4  $\text{g l}^{-1}$  in 1980s to 0.005  $\text{g l}^{-1}$  at 2000.<sup>1</sup> A similar regulation is set to control the sulfur content to 10  $\text{mg kg}^{-1}$  for both gasoline and diesel. Besides the limitations to the particular element in the fuel, another important issue to measure the quality of the fuels is related to the structure of the hydrocarbon, octane number (ON) for gasoline and CN for diesel. The ON has an almost negligible effect on pollution emission. However, the emission of hydrocarbons and carbon monoxide from diesel vehicles is strongly influenced by the CN.<sup>1</sup>

One method to improve diesel fuels is provided by modern upgrading technologies, e.g.

aromatics saturation and hydrocracking.<sup>2,3</sup> Aromatics, which are associated with relatively low CN, can be hydrogenated to saturated cyclic components (cycloalkanes) by hydrodearomatization catalysts. However, increasing of CN in this process is limited by the cyclic structure even when most of the aromatics are saturated. With the help of hydrocracking catalysts, the CN of cycloalkanes could be further increased by breaking the ring structure to form (linear) alkanes. The ideal case is that cycloalkanes are converted to more paraffinic compounds with a low degree of branching while preserving the initial molecular weights. Therefore, finding approaches to selectively open cycloalkane rings with minimum cleavage and side chains are much desired for generating products that meet (or exceed) the ever-tightening environmental regulations.

Due to the complexity of the involved chemistry, the mechanism of selectively ring-open (SRO) reactions has not clearly been elucidated experimentally and thus far remains at a hypothetical level. On the other hand, computational studies based on methods of density functional theory (DFT) provide tools to gain more insight into elementary reaction steps of a complex reaction network.<sup>4-8</sup>

In order to reach a detailed understanding at the atomic level of the hydrogenation-dehydrogenation reactions, in Chapter 3, a simpler and widely investigated system, the conversion of ethylene to ethylidyne on Pt(111), is studied. Ethylene is known to form two types of adsorption complexes,  $\pi$  adsorbed and di- $\sigma$  adsorbed on Pt(111)<sup>9-16</sup> at low temperatures. After the system is further heated, ethylene begins to convert to ethylidyne,  $\text{CH}_3\text{-C}\equiv$ , which is the only stable surface species at room temperature under ultra high vacuum (UHV) conditions.<sup>9,17</sup> In Chapter 3, the complete reaction network from ethylene to ethylidyne is studied at three different coverages over Pt(111) surface. All the transition states are located at 1/3 and 1/9 coverage and to help identify the mechanism of this conversion.

Chapter 4 turns back to the discussion of SRO reactions. As a model system, ring-opening (RO) of methylcyclopentane (MCP) on supported metal catalysts has extensively been studied in experiments.<sup>18-22</sup> Three RO products, linear *n*-hexane (*n*Hx) as well as branched 2-methylpentane (2MP) and 3-methylpentane (3MP) can be produced. However, to my knowledge, the best selectivity to the linear product, *n*Hx, is about 40% when the reaction is catalyzed by the supported highly dispersed Pt catalyst. Other catalysts, like Rh and Ir, have higher activities towards the RO reactions but only selectively produce 2MP and 3MP. In Chapter 4, the complete reaction network for the conversion of MCP to its ring-opening

products on Pt is studied. Three other metal catalysts, Pd, Rh, and Ir, are also investigated, only with the C–C scission step, which is believed to be crucial for the distribution of the products. The results show how the selectivity is controlled by the surface geometry and rationalizes the experimentally observed particle-size dependence of the selectivity on supported metal catalysts.

## Chapter 2

# Computational approach

Density functional theory (DFT)<sup>23</sup> is one of the most important quantum mechanical modeling methods developed in the last century since the 1970s, especially in the solid-state area. The idea to describe the total energy as a functional of the electron density roots in the Thomas-Fermi model of atoms, developed as early as the 1920s.<sup>24,25</sup> In the 1960s, the modern formulation of DFT is built up based on the two theorems.<sup>26</sup> The first one shows that the ground state properties of a many-electron system are uniquely determined by the electron density, a quantity that depends on only three spatial coordinates. The second theorem defines an energy functional for the system and proves that the correct ground state electron density minimizes this energy functional. Then, the formulation of DFT addressed by Kohn and Sham (KS) becomes the basis of current routinely used computational methods.<sup>27</sup> In the KS theory, the entire unknown part of the energy functional is collected in the exchange-correlation energy  $E_{XC}$ , where approximations are used, e.g. the generalized gradient approximation (GGA), or hybrid functionals.

In this thesis, slab-model calculations were carried on the basis of DFT with the plane-wave based Vienna *ab initio* simulation package (VASP).<sup>28,29</sup> The GGA was used in the form of the (approximate) exchange-correlation functional PW91.<sup>30</sup> The interaction between atomic cores and electrons was described by the projector augmented wave (PAW) method.<sup>31,32</sup> In the structure optimizations the Brillouin zone was sampled using  $k$  point meshes of Monkhorst-Pack type:<sup>33</sup>  $5 \times 5 \times 1$  for M(111) and M(211),  $5 \times 3 \times 1$  for M(322) surfaces, with first-order Methfessel-Paxton smearing (smearing width of 0.15 eV).<sup>34</sup> Total energies were evaluated with the broadening extrapolated to zero. After structure optimization, the energies were refined in single-point fashion employing a denser  $k$  point grid,  $7 \times 7 \times 1$  for M(111) and M(211), or  $7 \times 5 \times 1$  for M(322) surfaces. The valence wave functions were expanded in a plane-wave basis with a cutoff energy of 400 eV. The SCF energy was converged to  $10^{-4}$  eV.

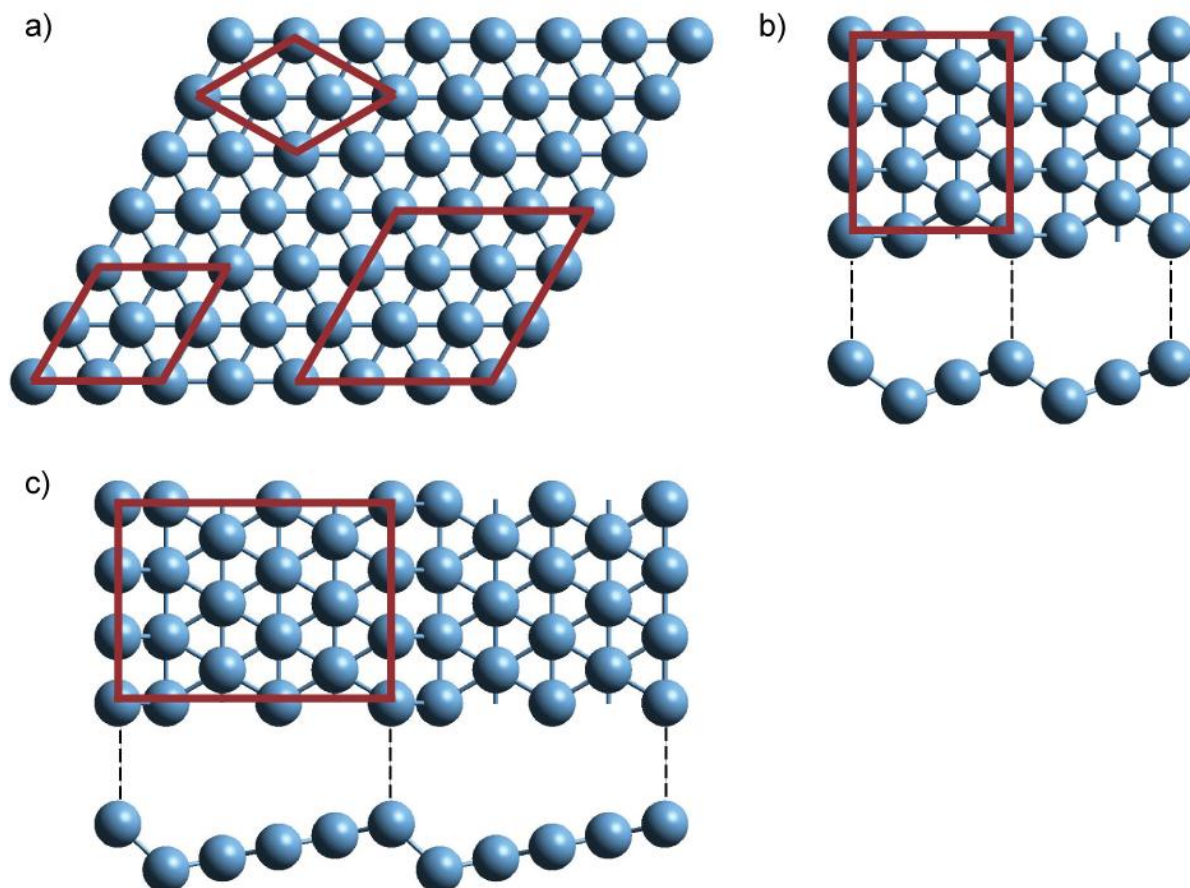


**Figure 2.1** Surface models used in this thesis: a) top view of M(111); top and side views of b) M(211) and c) M(322). Selected unit cells are outlined in red.

The parameters for calculations on organometallic compounds in the solid phase are similar to the slab model calculations except the  $k$  points mesh is changed to  $3 \times 3 \times 3$ . All of them were carried out with tetrahedron method with the Blöchl correction, which can reduce the number of  $k$  points with required accuracy for metal systems.<sup>35</sup> The shape and size of the unit cell was set according to X-ray diffraction (XRD) results<sup>36-38</sup> (Table 2.1) and not optimized during the optimization.

The ideal M(111), M(211) and M(322) surfaces are modeled by periodic five-layer slabs repeated in a supercell geometry. In the case of the stepped surface M(211) and M(322), a slab comprises five layers of (111) orientation, but formally contains 15 and 25 layers perpendicular to the surface normal, respectively. The surface is expanded periodically in two dimensions, and in the third dimension, a vacuum region is added to separate two adjacent slabs. The vacuum spacing, determined by the nucleus distance between the highest adsorbed atom and the lowest slab atom in the upper unitcell plus the diameter of a metal atom, is at

**Table 2.1** Unit cell parameters (Å and degree) of selected organometallic compounds in this thesis.

	<i>a</i>	<i>b</i>	<i>c</i>	$\alpha$	$\beta$	$\gamma$
$\text{Co}_3(\text{CO})_9(\text{CCH}_3)^a$	8.80	9.33	12.34	93.0	93.3	128.8
$\text{Os}_2(\text{CO})_6(\text{CH}_2\text{CH}_2)^b$	7.36	13.52	13.54	90.0	101.0	90.0
$\text{Os}_3(\text{CO})_{10}(\mu\text{-H})(\text{CHCH}_2)^c$	9.91	14.40	12.42	90.0	99.8	90.0

<sup>a</sup> Ref.36.   <sup>b</sup> Ref. 37.   <sup>c</sup> Ref. 38.

least 1 nm. The three “bottom” layers [of (111) orientation] of a slab were kept fixed at the theoretical bulk-terminated geometry and the two “upper” layers of metal atoms were allowed to relax during the geometry optimizations, together with the adsorbate, until the force on each atom was less than  $2 \times 10^{-4}$  eV/pm. The adsorbates were bound to “top” side of the slab models. Three different unit cells were used on M(111) surface,  $(\sqrt{3} \times \sqrt{3})R30^\circ$ ,  $(2 \times 2)$ , and  $(3 \times 3)$ , corresponding to surface coverages 1/3, 1/4, and 1/9, respectively (Fig. 2.1). On M(211) and M(322), a  $(3 \times 1)$  unit cell was used corresponding to the surface coverage 1/9, and 1/15, respectively.

The binding energy (BE) of an adsorbate was determined from  $\text{BE} = E_{\text{ad}} + E_{\text{sub}} - E_{\text{ad/sub}}$ , where  $E_{\text{ad/sub}}$  is the total energy of the slab model, covered with the adsorbate in the optimized geometry;  $E_{\text{ad}}$  and  $E_{\text{sub}}$  are the total energies of the adsorbate in the gas phase (ground state) and of the clean substrate, respectively. Calculations on gas-phase hydrocarbon species with open shells were carried out in spin-polarized fashion. With the above definition, positive values of BE imply a release of energy or a favorable interaction.

Transition states (TS) of reactions were determined by applying the dimer method<sup>39</sup> or the nudged elastic band method.<sup>40,41</sup> In the latter case eight images of the system were used to form a discrete approximation of the path between fixed end points. The TS structures obtained in this way were further refined until the forces on atomic centers dropped below  $2 \times 10^{-4}$  eV/pm. For each optimized TS structure, a normal mode analysis was done to confirm that only a single imaginary frequency exists.

The vibrational frequencies were obtained from a normal mode analysis where the elements of the Hessian were approximated as finite differences of analytical gradients,

displacing each atomic center by 1.5 pm either way along each Cartesian direction. In these calculations the energy cut-off was increased to 520 eV and tightened the SCF energy convergence to  $10^{-6}$  eV. Checks showed that the resulting frequency should be accurate to 2–3  $\text{cm}^{-1}$  in the selected model.

## Chapter 3

# Ethylene transformations over Pt(111)

### 3.1. Background

#### 3.1.1 Experimental research

Due to the worldwide growing demand in energy, the price of energy sources, e.g. petroleum, is pushed up steadily. Recently, other alternatives of energy sources, like biomass, solar energy, attract attention by a large group of people from governments and research facilities. However, one should not ignore that petroleum currently is still the largest energy source.<sup>42</sup> Therefore, how to convert more efficiently petroleum to the desired products is still an important issue for petroleum industry.

The hydrogenation-dehydrogenation reactions of hydrocarbons catalyzed by noble metal particles are one of the most important reaction series in the petroleum industry. As the simplest molecule with a C=C double bond, the transformations of ethylene on the Pt(111) surface serve as a simple model system for hydrogenation-dehydrogenation reactions which recently are attracting renewed interest, as reflected in several experimental<sup>43–46</sup> and theoretical<sup>46–54</sup> studies.

There are two types of adsorption complexes of ethylene on Pt(111).<sup>9–16</sup> At very low temperatures (< 52 K),<sup>15</sup>  $\pi$ -adsorbed ethylene has been observed. After the system is heated above 52 K,  $\pi$ -adsorbed ethylene started to transform to a di- $\sigma$  bonded species<sup>12–14</sup> at low pressures of ethylene. Further heating of the system to a higher temperature (~250 K) will irreversibly convert ethylene to a strongly bound species, ethylidyne ( $\text{CH}_3\text{-C}\equiv$ ), which is the only stable surface species at room temperature under UHV conditions.<sup>9, 17</sup> A similar process

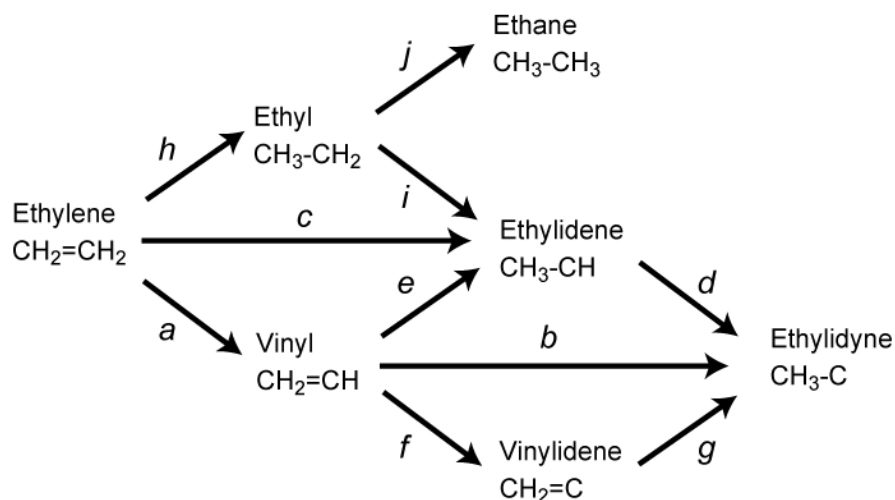


**Figure 3.1** Reaction scheme of the conversion from ethylene to ethylidyne

from ethylene to ethylidyne has also been observed on other transition metal surfaces such as Rh(111),<sup>55</sup> Pd(111),<sup>56</sup> Ir(111),<sup>57</sup> and Ru(0001).<sup>58</sup> The formation of ethylidyne, which is a strongly bound species, can block active sites on metal surfaces and thus affect the activity of the catalyzed reactions.

In order to find a way to prevent the formation of ethylidyne, the reaction mechanism of this conversion is extensively studied since the 1970s. Four kinds of C<sub>2</sub> species were proposed as intermediate during the conversion: ethyl (CH<sub>3</sub>CH<sub>2</sub>),<sup>59</sup> vinyl (CH<sub>2</sub>CH),<sup>60</sup> vinylidene (CH<sub>2</sub>C),<sup>61</sup> and ethylidene (CH<sub>3</sub>CH),<sup>62, 63</sup>. A summarized reaction scheme during this conversion, including hydrogenation, dehydrogenation and 1,2-hydrogen shift reactions, is shown in Fig. 3.1. For easy comparison, I assigned the labels of the various elementary reactions consistent with those of earlier publications on the analogous reaction mechanisms on Pd(111).<sup>64, 65</sup> The first proposed intermediate was ethyl<sup>59</sup> based on the calculated activation energies via different intermediates. However, Zaera<sup>66, 67</sup> found that an ethyl group can easily convert to ethylene via  $\beta$ -elimination on Pt(111). At the same time, he also suggested that vinyl could be a possible intermediate because H<sub>2</sub> desorption was enhanced from trideuterioethylene compared with the expected selectivity on purely stoichiometric grounds.<sup>60</sup> Later calculations at the extended Hückel level by Ditlevsen et al.<sup>61</sup> suggested a mechanism with two subsequent dehydrogenation steps via vinyl and vinylidene followed by the hydrogenation to ethylidyne. However, both vinyl and vinylidene were ruled out by Zaera and Bernstein later because vinyl could convert back to ethylene via the intermediate

vinylidene and acetylene at temperature as low as 200 K.<sup>68</sup> Finally, ethylidene is the last survivor. Both Cremer et al.<sup>62</sup> and Deng et al.<sup>63</sup> reported to have detected ethylidene during the conversion of ethylene to ethylidyne via sum frequency generation (SFG) and reflection adsorption infrared spectroscopy (RAIRS), respectively. For an overview of pertinent experimental results, see Refs. 69,70.

Zaera et al. carried out extensive kinetic and spectroscopic studies<sup>68-71</sup> related to the thermal chemistry of adsorbed ethylene on Pt(111) and suggested a two-step mechanism of ethylidyne formation (Pathway *c-d*, Fig. 3.1): (1) ethylene converts to ethylidene through a direct 1,2-H shift reaction, and (2) ethylidene dehydrogenates to ethylidyne. However, such a mechanism would tentatively fit available experimental results on this system only by invoking a fast pre-equilibrium between ethylene and ethylidene in conjunction with a slow second step at coverages close to saturation.

### 3.1.2 Previous theoretical research

It seems that the two step mechanism successfully explains most of the important experimental observation and the corresponding reaction intermediate was also observed by other experiments. However, theoretical studies found a conflicting result. Anghel et al.<sup>72,73</sup> studied several reactions related to ethylene on the Pt(110) surface with density functional calculations. The barriers of the hydrogenation or dehydrogenation reactions related to ethylene are mostly between 25–70 kJ mol<sup>-1</sup>, but the reaction barrier for the 1,2-H shift reaction from ethylene to ethylidene is as high as 223 kJ mol<sup>-1</sup>, which is too high for the reaction step to occur at room temperature. Another study on the ethylene conversion to ethylidyne over Pd(111) obtained similar results, where the barrier of the direct conversion of ethylene to ethylidene was as high as 200 kJ mol<sup>-1</sup>.<sup>65</sup>

However, the above mentioned theoretical studies slightly differ from the experimental results discussed in Section 3.1.1. For example, the Pt(110) surface, used in Refs. 72 and 73, is more reactive than the Pt(111) surface used in most experimental studies. The Pd(111) surface, used in Refs. 64 and 65, also has a close-packed surface structure as Pt(111), but the reaction mechanism might be different due to the fact that no intermediate has been observed in the experimental studies on this conversion over Pd(111). Former theoretical studies of ethylene transformations on the Pt(111) are mainly limited to the adsorption properties of C<sub>2</sub>H<sub>n</sub> species,<sup>46-54</sup> while they seldom touch on the reaction mechanism of ethylidyne

formation.

### 3.1.3 Models in the current study

In order to gain direct theoretical evidence on the reaction mechanism of the conversion from ethylene to ethylidyne over Pt(111), I studied all possible types of reactions, hydrogenation, dehydrogenation, and 1,2 H-shift reactions (Fig. 3.1). One of the important goals of the present theoretical study was to show that the mechanism with 1,2-H shift reaction can unequivocally be ruled out on the basis of calculated barriers. Instead, more complicated three-step pathways which avoid direct H-shift reactions appear plausible on Pt(111).

This section presents a systematic computational study with three three-step routes, Reactions *a-e-d*, *a-f-g* and *h-i-d* in Fig. 3.1, for the transformation of ethylene to ethylidyne. Four different intermediates, ethylidene, vinyl, vinylidene and ethyl, were considered in the calculation. The calculations were carried out with a plane-wave based density functional method and periodic slab models, as described in Chapter 2. Based on the calculated activation energy of each elementary step, the viability of different routes is discussed, suggesting a new interpretation of the existing experimental data. Throughout this work, I will systematically compare the results of our calculations at different adsorbate coverage, 1/3, 1/4, and 1/9.

## 3.2. Structure and energetics of surface species and transition states

Fig. 3.1 shows the reaction network studied in this chapter, comprising 10 different elementary reactions, Reaction *a-j*, including hydrogenation, dehydrogenation and 1,2-H shift reactions with four different intermediates (vinyl, ethylidene, vinylidene, and ethyl).

### 3.2.1 Structure and energetics of surface species

In this section, I mainly introduce the adsorption properties of the C<sub>2</sub> species which were investigated in this thesis. Fig. 3.2 shows the adsorption modes of all these species on Pt(111). One general rule for hydrocarbon adsorption is that C atoms tend to form four bonds with other C, H, or Pt atoms to maintain a sp<sup>3</sup> configuration. In the following, I will discuss these species one by one in detail.

**Ethylene.** Previous experiments identified in total two adsorption modes,  $\pi$  and di- $\sigma$  mode, of ethylene on Pt(111).<sup>9–16</sup> Ethylene in a  $\pi$  adsorption complex is attached to the top site of one Pt atom via a  $\pi$  donor bond, while in the di- $\sigma$  mode, the adsorbate is attached to two adjacent Pt atoms at a bridge site in  $\eta^2$  fashion via two  $\sigma$  bonds.  $\pi$ -bound ethylene is stable only at very low temperatures which is confirmed by the spectroscopic studies.<sup>15</sup> This structure will start to convert to the di- $\sigma$  mode when the temperature of the system is higher than 52 K.

The adsorption sites of ethylene species on Pt(111) and the geometries of the corresponding adsorption complexes are expected to be similar to those identified on the surface Pd(111); therefore, it was assumed in this and other studies<sup>12,46,49,52</sup> that di- $\sigma$  ethylene should also occupy a bridge site on Pt(111). However, in a study that used diffuse low-energy electron diffraction (LEED), Döll et al. reported<sup>74</sup> a structure where ethylene adsorbs above a hollow site on Pt(111). In this structure, the C–C bond was tilted by  $\sim 22^\circ$  with respect to the surface plane. However, later theoretical studies disagreed with that result. Slab-model computational studies<sup>50–52</sup> at 0.25 ML coverage showed that bridge adsorbed di- $\sigma$  ethylene, with the C–C bond parallel to the surface, binds stronger than in the hollow-site complex, by 50–63 kJ mol<sup>-1</sup>. An earlier near-edge X-ray adsorption fine structure (NEXAFS) study<sup>12</sup> assumed the C–C bond parallel to the surface plane without direct information on the adsorption site of the ethylene molecule.

Several theoretical studies<sup>46,49,50,52,53</sup> reported the adsorption geometries of two kinds of adsorption complexes of ethylene on the surface Pt(111). The present results for bond lengths agree with these earlier works within 1–5 pm, Table 3.1. In the di- $\sigma$  ethylene complex, the C–C bond is adsorbed above a bridge position, parallel to the surface plane. The calculated C–C bond length, 149 pm, perfectly falls into the range of the experimental NEXAFS result, 149 $\pm$ 4 pm.<sup>12</sup> The C–C bond length is (almost) comparable with the bond length of gas phase ethane, 154 pm, and is significantly longer than for ethylene in the gas phase, 134 pm. Both of these factors reflect that the carbon centers in the di- $\sigma$  ethylene are already rehybridized toward sp<sup>3</sup>. However, in the  $\pi$ -adsorbed adsorption complex, the calculated C–C bond length is only 141 pm, indicative of sp<sup>2</sup> hybridized carbon centers. This calculated value perfectly agrees with the NEXAFS result, 141 pm.<sup>11</sup> The C–Pt bond lengths are also different in two kinds of adsorption complexes. In the  $\pi$ -adsorbed case, they are 217–220 pm, which are 6–9 pm longer than the corresponding bond of the di- $\sigma$  complex. The geometry is slightly affected by the

**Table 3.1** Calculated structural parameters (pm), and binding energies BE (kJ mol<sup>-1</sup>) of ethylene adsorbed on Pt(111) in di- $\sigma$  and  $\pi$  modes at different surface coverage  $\theta$ .

	$\theta$	C–C	C–Pt	BE
di- $\sigma$ ethylene	1/3	149 <sup>a</sup>	211 <sup>a</sup>	105 <sup>a</sup>
	1/4	149 <sup>a</sup> , 148 <sup>b</sup> , 148 <sup>h</sup> , 148 <sup>k</sup> , 149 <sup>k</sup>	211 <sup>a</sup> , 211 <sup>b</sup> , 210 <sup>h</sup> , 214 <sup>k</sup> , 212 <sup>k</sup>	114 <sup>a</sup> , 117 <sup>b</sup> , 100 <sup>c</sup> , 101 <sup>d</sup> , 122 <sup>h</sup> , 109 <sup>k</sup> , 127 <sup>k</sup>
	1/9	149 <sup>a</sup>	211 <sup>a</sup> , 212 <sup>a</sup>	121 <sup>a</sup>
	exp.	149 <sup>e,f</sup>		71 <sup>c,g</sup>
$\pi$ ethylene	1/3	141 <sup>a</sup>	217 <sup>a</sup>	60 <sup>a</sup>
	1/4	141 <sup>a</sup> , 141 <sup>b</sup> , 140 <sup>h</sup>	217 <sup>a</sup> , 218 <sup>a</sup> , 218 <sup>b</sup> , 222 <sup>h</sup>	70 <sup>a</sup> , 73 <sup>b</sup> , 65 <sup>d</sup> , 54 <sup>h</sup>
	1/9	141 <sup>a</sup>	219 <sup>a</sup> , 220 <sup>a</sup>	84 <sup>a</sup>
	exp.	141 <sup>i</sup>		40±10 <sup>j</sup>

<sup>a</sup>This work. <sup>b</sup>Ref. 49. <sup>c</sup> Ref. 46. <sup>d</sup> Ref. 53. <sup>e</sup> Ref. 12. <sup>f</sup> Ref. 13. <sup>g</sup> Ref. 76. <sup>h</sup> Ref. 52. <sup>i</sup> Ref. 10. <sup>j</sup> Ref. 16. <sup>k</sup> Ref. 50.

coverage. The C–Pt bond lengths slightly increased, by less than 3 pm from 1/3 to 1/9 coverage.

Under UHV conditions,  $\pi$ -bound ethylene is reported to be stable only at low temperatures.<sup>15</sup> After the system is heated above 52 K,  $\pi$ -bound ethylene starts to convert to the di- $\sigma$  mode which dominates between 100–250 K on the Pt(111) surface.<sup>12–14</sup> Further heating of the system irreversibly converts ethylene to ethylidyne.<sup>9,17</sup> However, at different conditions, e.g. high pressure of several hundred Torr other than UHV, the relative surface population of the two types of adsorbed ethylene might change to some extent. For example, studying ethylene hydrogenation on Pt(111), Cremer et al.<sup>75</sup> observed that ethylene could coexist with ethylidyne on the Pt surface when the surface was exposed to ethylene and hydrogen gas at room temperature. Both di- $\sigma$  and  $\pi$ -bound ethylene complexes were detected in comparable concentrations. These authors also pointed out that the precursor for the hydrogenation reaction of ethylene is the weakly adsorbed  $\pi$ -bound ethylene species.

Table 3.1 summarizes several recent theoretical studies that reported binding energies of the two kinds of surface-bound ethylene.<sup>10,12,13,16,46,49,50,52,53,76</sup> The models and methodologies

**Table 3.2** Calculated binding energies BE ( $\text{kJ mol}^{-1}$ ) of ethylene adsorbed on Pt(111) and Pd(111) in di- $\sigma$  and  $\pi$  modes at different surface coverage  $\theta$ .

	$\theta = 1/3$		$\theta = 1/4$		$\theta = 1/9$	
	Pt(111) <sup>a</sup>	Pd(111) <sup>b</sup>	Pt(111) <sup>a</sup>	Pd(111) <sup>b</sup>	Pt(111) <sup>a</sup>	Pd(111) <sup>b</sup>
di- $\sigma$ ethylene	105	71	114	83	121	90
$\pi$ ethylene	60	NA <sup>c</sup>	70	64	84	78

<sup>a</sup>This work. <sup>b</sup>Ref. 64. <sup>c</sup> not available

for these calculation, periodic slab models of 2–4 layers and the exchange-correlation functional PW91, are similar to present work. Similar to the reported experimental energy preference for di- $\sigma$  ethylene, the calculated binding energy of di- $\sigma$  ethylene at 1/4 coverage was 36–68  $\text{kJ mol}^{-1}$  more stable than  $\pi$ -bound ethylene (Table 3.1).<sup>49,52,53</sup> The present study obtained the di- $\sigma$  mode to be more favorable by 37–45  $\text{kJ mol}^{-1}$ , depending on coverage. For di- $\sigma$  ethylene, the calculated adsorption energy increases from 105 to 121  $\text{kJ mol}^{-1}$  with decreasing coverage (Table 3.1). The obtained adsorption energy at 1/4 coverage, 114  $\text{kJ mol}^{-1}$ , perfectly falls into the range of previous theoretical studies, 100–127  $\text{kJ mol}^{-1}$ , of the binding energy on Pt(111).<sup>46,49,50,52,53</sup> Previous calculation with reasonably large cluster models<sup>47</sup> obtained a slightly larger binding energy,  $\sim 130 \text{ kJ mol}^{-1}$ .

Slightly lower binding energies were reported by several different experimental studies. For example, temperature programmed desorption (TPD) measurements yielded the adsorption energy of di- $\sigma$  ethylene on Pt(111) at 71  $\text{kJ mol}^{-1}$  (Table 3.1).<sup>46,76</sup> The calculated value is larger by about 40  $\text{kJ mol}^{-1}$ . A similar smaller TPD-derived binding energy of di- $\sigma$  ethylene was also reported on Pd(111), 68  $\text{kJ mol}^{-1}$ .<sup>77</sup> These results are not surprising because the PW91 GGA functional, used in this calculation, is known to overestimate systematically chemisorption energies by up to 50  $\text{kJ/mol}$ .<sup>78</sup> Another experimental study,<sup>16</sup> with RAIRS, also reported a slightly lower adsorption energy  $40 \pm 10 \text{ kJ mol}^{-1}$  compared with the calculated adsorption energy of  $\pi$  ethylene on Pt(111), 60–84  $\text{kJ mol}^{-1}$  (Table 3.1).

The calculated energy difference between di- $\sigma$  and  $\pi$  species on Pd(111),<sup>64</sup> 12–19  $\text{kJ mol}^{-1}$ , is slightly larger on Pt(111), 37–45  $\text{kJ mol}^{-1}$  (Table 3.2). The adsorption energies of  $\pi$  species on both surfaces are in the similar range, 60–84  $\text{kJ mol}^{-1}$ . However, the adsorption of

di- $\sigma$  species on Pd(111) is weaker than the one on Pt(111). The adsorption energies are calculated only 71–90 kJ mol<sup>-1</sup> on Pd(111) while they are 105–121 kJ mol<sup>-1</sup> on Pt(111). It is interesting to point out that the calculated C–C bond length on Pt(111) is 4–5 pm longer than that determined structure for di- $\sigma$  ethylene adsorbed on Pd(111),<sup>64</sup> in line with the ~30 kJ mol<sup>-1</sup> larger binding energy of the complex on Pt(111). Recall that a slightly higher binding energy on Pt(111) was measured compared to the value on Pd(111) by previous TPD experiment.<sup>46,76,77</sup> In summary, a larger binding energy, 105–121 kJ mol<sup>-1</sup>, of di- $\sigma$  ethylene on Pt(111) is predicted in this thesis, which is 30–40 kJ mol<sup>-1</sup> larger than on Pd(111), see Ref. 64 and references therein.

**Ethylidyne.** Ethylidyne is formed at high temperature after heating adsorbed ethylene on various transition metal surfaces such as Rh(111),<sup>55</sup> Pd(111),<sup>56</sup> Ir(111),<sup>57</sup> and Ru(0001).<sup>58</sup> The structure of ethylidyne on Pt(111) was unclear until the end of the 1970s. With LEED, Kesmodel et al.<sup>17,79</sup> identified that ethylidyne adsorbed at three-fold hollow sites, with the C–C bond perpendicular to the metal surface. A later LEED study<sup>80</sup> supported by density functional calculations<sup>52</sup> suggested a slight preference of the fcc over the hcp site.

In this thesis, the structure of the more stable fcc adsorbed ethylidyne was optimized. The C–C bond is perpendicular to the Pt(111) surface, with the bond length at 149 pm for all the investigated coverages. The C–Pt bonds were calculated at 201–203 pm. All of them are in good agreement with earlier theoretical values.<sup>52</sup> The calculated C–C bond length agrees very well with the one obtained in the LEED study,<sup>80</sup> 149±5 pm, while a slightly shorter C–Pt bond length, 191±5 pm, is reported in that LEED study.

The binding energies of ethylidyne calculated at fcc site on Pt(111) are in the range 575–593 kJ mol<sup>-1</sup> (Table 3.3), with respect to the doublet state of ethylidyne in the gas phase. The binding energy increases with decreasing coverage. Former calorimetric measurements<sup>81</sup> showed that 174±4 kJ/mol of heat are released in the dissociative adsorption of ethylene to form ethylidyne species and surface hydrogen atoms on Pt(111). Slightly lower values, 145–157 kJ mol<sup>-1</sup>,<sup>82,83</sup> resulted from measurements on supported Pt samples. The calculation of this thesis predicts an energy change of 118–160 kJ/mol for this reaction, where the more exothermic process corresponds to lower coverage. Compared with Pd(111), the geometries of ethylidyne on Pt(111) are quite similar; C–Pd bonds are at most 5 pm shorter than the C–Pt bonds. The adsorption energies on Pt(111) were calculated 40–44 kJ mol<sup>-1</sup> larger than those

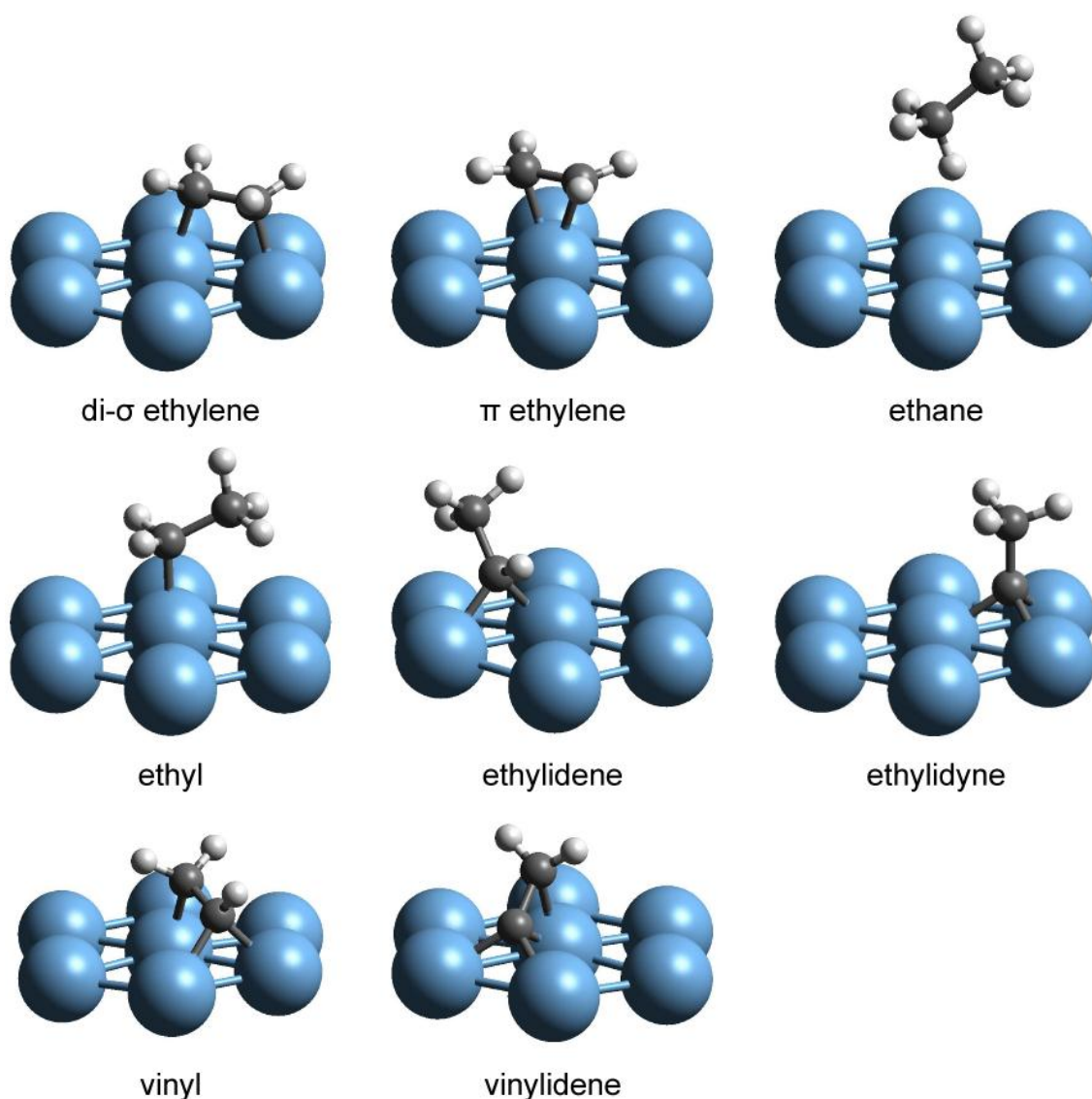


**Figure 3.2** Adsorption complexes of all C<sub>2</sub> species investigated in this thesis

on Pd(111).<sup>64</sup>

**Intermediates: Vinyl, Vinylidene, Ethyl, Ethylidene.** The adsorption of these potential reaction intermediates on Pt(111) has been addressed in previous computational studies.<sup>47,50,54</sup> Generally speaking, the unsaturated C centers tend to form various numbers of C–Pt bonds. The number of C–Pt bonds is determined by the (de-)saturation of the C atoms, with all the C centers turning to sp<sup>3</sup> hybridized on Pt(111). The binding energy of the adsorbate decreases with increasing surface coverage due to the stronger adsorbate-adsorbate repulsion at high coverage. Table 3.3 summarized important geometry properties and adsorption energies of the investigated intermediates.

**Table 3.3** Optimized geometries<sup>a</sup> (pm) and energy characteristics (kJ mol<sup>-1</sup>) of intermediates in the transformation of ethylene to ethylidyne at various coverages  $\theta$ .

	$\theta$	C–C	C–Pt	BE <sup>b</sup>
Vinyl	1/3	147	208, 208, 210	301
	1/4	147	207, 207, 209	318
	1/9	147	207, 207, 209	324
Ethyl	1/3	151	209	186
	1/4	151	210	191
	1/9	151	210	195
Vinylidene	1/3	141	199, 199, 210, 223	415
	1/4	141	198, 198, 212, 221	434
	1/9	141	198, 198, 212, 221	441
Ethylidene	1/3	150	207, 207	373
	1/4	150	207, 207	382
	1/9	150	207, 207	390
Ethylidyne	1/3	149	201, 202, 202	575
	1/4	149	202, 203, 203	584
	1/9	149	202, 202, 202	593
Ethane	1/3	152		7
	1/4	153		8
	1/9	153		6

<sup>a</sup> A–B, distance between atoms A and B. <sup>b</sup> Binding energy (BE) of an adsorbate (see text).

Vinyl (CH<sub>2</sub>CH) prefers to bind over a three-fold site on Pt(111) surface in  $\mu_3\text{-}\eta^2$  fashion. The calculated C–C bond length, 147 pm, is only 2 pm shorter than that of di- $\sigma$  ethylene, indicating rehybridization to sp<sup>3</sup> carbon. The C–Pt bond lengths are 207–210 pm. The binding energies of this species are 301–324 kJ mol<sup>-1</sup> when going from 1/3 to 1/9 coverage.

Similar to vinyl, vinylidene (CH<sub>2</sub>C) also prefers to bind over a three-fold site. It is adsorbed in  $\mu_3\text{-}\eta^2$  fashion on the Pt(111) surface. The calculated C–C bond length, 141 pm, is 6 pm shorter than for adsorbed vinyl, indicating a higher C–C bond order. The C–Pt bond lengths are 198–224 pm. The binding energies of this species are 399–441 kJ mol<sup>-1</sup> from 1/3 to 1/9 coverage. These values are ~100 kJ mol<sup>-1</sup> larger than the binding energies of vinyl due to one more C–Pt interaction for vinylidene.

Ethyl binds at a top site of the Pt(111) surface. The calculated C–C bond length is 151

pm. The C–Pt bond length is 209–210 pm. The binding energies of this species are 186–195 kJ mol<sup>-1</sup> from 1/3 to 1/9 coverage. This interaction is much weaker than that of the two previous intermediates because ethyl forms only one C–Pt bond.

Ethylidene (CH<sub>3</sub>CH) binds at bridge sites of the Pt(111) surface. The calculated C–C bond length is 150 pm. The C–Pt bond lengths are 207 pm. The binding energies of this species are 372–390 kJ mol<sup>-1</sup> from 1/3 to 1/9 coverage.

**Coadsorbrate: Hydrogen.** The hydrogenation / dehydrogenation reactions require additional surface H atoms in the initial / final state, respectively. The structures of C<sub>2</sub>H<sub>n</sub> species with coadsorbed H atoms have also been optimized. The H atoms were placed at free three-fold hollow sites near the C<sub>2</sub>H<sub>n</sub> species.

The geometries of the adsorbed C<sub>2</sub>H<sub>n</sub> species are hardly affected by the coadsorption of the H atoms. In most cases, bond lengths change less than 2 pm. The effect is stronger at high coverage, due to limited free surface area for the newly introduced H atom. For example, in the high coverage case of vinylidene, the coadsorbed H atom is too close to the vinylidene and the repulsion between them pushes vinylidene away from the surface. The H<sub>2</sub>C–Pt bond is elongated by 9 pm with respect to vinylidene adsorbed alone. Another example is di-σ adsorbed ethylene. At 1/3 coverage, the C–C bond is no longer adsorbed parallel to the Pt–Pt bond at the bridge site. Due to the repulsion by the additional coadsorbed H atom these two bonds form an angle of 10°.

The calculated adsorption geometries of the hydrocarbon fragments on Pt(111) are quite close to those calculated on Pd(111).<sup>64,65</sup> At higher coverage, the distortion of vinylidene is also observed on Pd(111) when coadsorbed with hydrogen. The distortion is stronger on Pd(111) which is attributed to the stronger repulsive interaction on Pd(111) due to the slightly smaller atomic radius of Pd (280 pm) compared to Pt (282 pm) as well as the weaker binding of vinylidene on Pd(111) by ~50 kJ mol<sup>-1</sup>.

### 3.2.2 Transition State Structures for Ethylene Conversion to Ethylidyne

In this section, I will discuss the transition states and the corresponding reaction barriers of all elementary reactions shown in Fig. 3.1 (a–j). Similar to the local minima, the transition state structures are only slightly affected by surface coverage. Therefore, I will mainly refer to the results obtained for the coverage 1/9. In the discussion, each transition state is labeled as

“TSx”, where x is the label of the corresponding elementary step used in Fig. 3.1. For the hydrogenation and dehydrogenation reactions, an H atom at a specific site close to the hydrocarbon in its initial or final state, respectively, is part of the model. Previous research<sup>84</sup> showed that the activation energy for the diffusion steps of H atom over Pt(111) is as low as 4 kJ mol<sup>-1</sup>, indicating fast surface diffusion of H atoms. Therefore, modeling of H diffusion steps was skipped. Table 3.4 summarizes reaction energies and barrier heights of all these elementary steps.

**Ethylene to Vinyl (TSa).** The initial state of this reaction is di- $\sigma$  adsorbed ethylene. In the transition state structure TSa (Fig. 3.3), one of the C atoms moves from the top site to an adjoining bridge site, forming the second C–Pt bond, 220 pm. The top site, which is originally occupied by the C atom, interacts with the dissociating H atom with H–Pt = 162 pm. Accordingly the C–H interaction is weakened, which is reflected by the elongation of C–H distance to 155 pm. In the final state, the dissociated H atom arrives at a three-fold site. The reaction is endothermic by 14–51 kJ mol<sup>-1</sup> at different coverages. The activation energy of this elementary reaction is as high as 92 kJ mol<sup>-1</sup> at 1/3 coverage and 75 kJ mol<sup>-1</sup> at 1/9 coverage.

**Vinyl to Ethynidyne (TSb).** During this 1,2-shift reaction, the hydrocarbon does not change the adsorption site. In TSb (Fig. 3.3), the weakened C–H bond is elongated to 123 pm. The H atom, which is shifted in the reaction, moves to the area between the two C atoms, with the newly formed C–H bond at 137 pm. The C atom, which accepts the shifted H atom, moves upwards so that the C–C axis bends toward the surface normal. At 1/3 coverage, the C–Pt bond breaks completely with C–Pt = 332 pm. The other C atom is still located at the bridge site (Fig. 3.4). However, at 1/9 coverage, the H-donating C atom moves to the three-fold site, forming a third C–Pt bond at 208 pm, and the other two C–Pt distances of this carbon shrink to 199 pm, 8 pm shorter than in the reactant vinyl. The migrating H atom travels far above the surface and does not seem to interact directly with Pt atoms. Thus, the reaction does not appear to be surface-assisted. Consequently, the activation energy of this reaction is very high, 195 kJ mol<sup>-1</sup> at 1/3 coverage and 168 kJ mol<sup>-1</sup> at 1/9 coverage. The reaction is exothermic by about 50 kJ mol<sup>-1</sup> at both coverages studied.

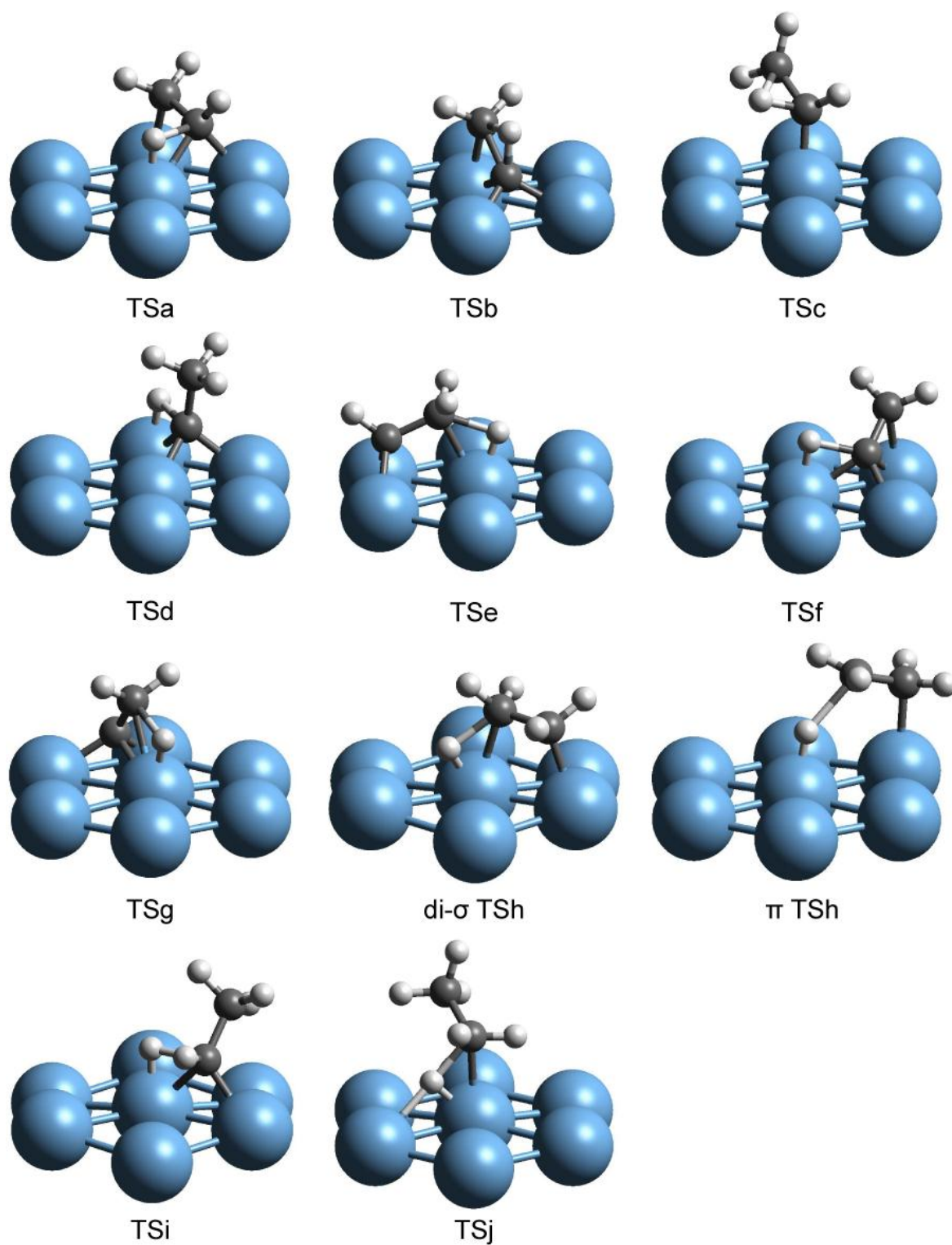


**Figure 3.3** Optimized structures of the transition states of the elementary reactions *a–j* (see Fig. 3.1) at 1/9 coverage.

*Ethylene to Ethylidene (TSc).* This 1,2-H shift reaction was proposed<sup>68–71</sup> as the first step of ethylene conversion to ethylidyne. In the corresponding transition state TSc (Fig. 3.3),

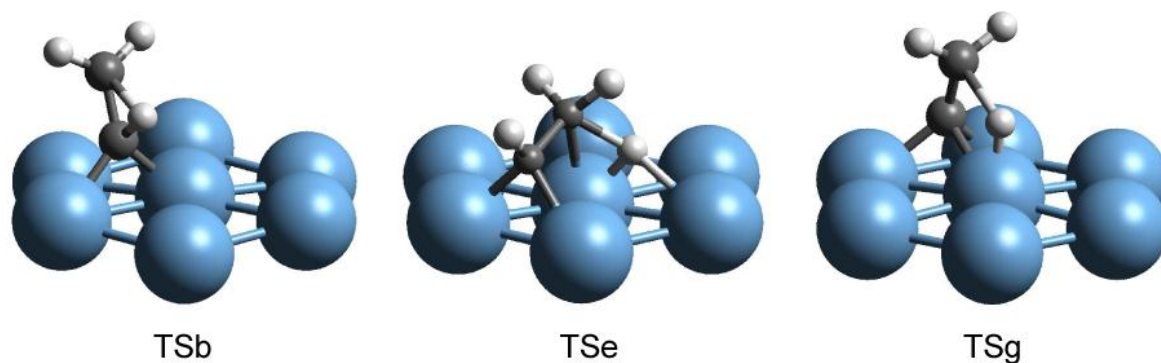


**Figure 3.4** Optimized structures of the transition states of the elementary reactions *b*, *e* and *g* (see Fig. 3.3) at 1/3 coverage.

the reactive H atom moves to the area between the two C atoms, similar to in TSb. The corresponding C–H bond elongates by 16 pm, to 126 pm and a new C–H bond, with the H-accepting C atom, is formed; C–H = 151 pm. Due to this newly formed interaction, the H-accepting C atom detaches from the surface, directing the C–C bond toward an upright orientation. The H-donating C atom still occupies a top site with the C–Pt bond shortened by 10 pm to 200 pm. In the final state, this atom shifts to an adjacent bridge position while the C–H bond is completely broken. Again, due to lack of interaction between the migrating H atom and the metal surface, the activation energy is very high, 229 kJ mol<sup>-1</sup> at 1/3 coverage and 202 kJ mol<sup>-1</sup> at 1/9 coverage. The reaction is endothermic by about 30 kJ mol<sup>-1</sup>.

***Ethylidene to Ethylidyne (TSd).*** Initially, ethylidene is adsorbed at a bridge site. In the transition state TSd, the reactive C atom moves toward a three-fold site. The dissociating H atom of the CH group passes through a top-bound state, with the C–H bond elongated by 27 pm, to 137 pm. The C–C bond is nearly perpendicular to the surface, hence very close to the structure of the product complex of ethylidyne. In the final state, the H atom moves further to a three-fold hollow site. This reaction is strongly exothermic, 44 kJ mol<sup>-1</sup> at 1/3 coverage and 70 kJ mol<sup>-1</sup> at 1/9 coverage. The activation energy is much lower than typical barriers of hydrogenation / dehydrogenation reactions investigated in this thesis, 29 kJ mol<sup>-1</sup> at 1/3 coverage and 19 kJ mol<sup>-1</sup> at 1/9 coverage. Similarly low barriers were also calculated for the same reaction on Pd(111).<sup>64</sup> This low barrier suggests the dehydrogenation of ethylidene to ethylidyne to be fast and irreversible. Our result is consistent with the experimental observation<sup>85</sup> that ethylidene can readily transform to ethylidyne at 150 K.

**Table 3.4** Optimized geometries<sup>a</sup> (pm) and energy characteristics (kJ mol<sup>-1</sup>) of transition states<sup>b</sup> of ethylene transformations to ethynidyne at various coverages  $\theta$ .

		$\theta$	C–C	C–H <sup>c</sup>	H–Pt <sup>c</sup>	C–Pt	$\Delta E^d$	$E_a^e$
TSa	CH <sub>2</sub> CH <sub>2</sub> → CH <sub>2</sub> CH+H	1/3	148	160	161	207, 209, 220	51	92
		1/9	148	155	162	208, 209, 220	14	75
TSb	CH <sub>2</sub> CH → CH <sub>3</sub> C	1/3	140	124, 159		199, 199, 275, 332	-55	195
		1/9	139	126, 151		199, 199, 208, 213	-51	168
TSc	CH <sub>2</sub> CH <sub>2</sub> → CH <sub>3</sub> CH	1/3	141	125, 145		198	31	229
		1/9	139	126, 151		200	30	202
Tsd	CH <sub>3</sub> CH → CH <sub>3</sub> C+H	1/3	152	140	165	202, 202, 222	-44	29
		1/9	151	137	167	203, 203, 226	-70	19
TSe	CH <sub>2</sub> CH+H → CH <sub>3</sub> CH	1/3	149	150	169, 217	207, 208, 226	-20	65
		1/9	149	156	160, 281	206, 206, 225	17	78
TSf	CH <sub>2</sub> CH → CH <sub>2</sub> C+H	1/3	142	148	165	199, 210, 213, 220	32	69
		1/9	142	144	166	199, 210, 215, 217	-15	53
TSg	CH <sub>2</sub> C+H → CH <sub>3</sub> C	1/3	140	181	161	199, 199, 216, 271	-87	58
		1/9	142	165	162	197, 197, 216, 233	-36	80
TSh- $\sigma$	CH <sub>2</sub> CH <sub>2</sub> +H → CH <sub>3</sub> CH <sub>2</sub>	1/3	150	153	162	210, 227	-15	75
		1/9	150	154	162	209, 228	23	88
TSh- $\pi$	CH <sub>2</sub> CH <sub>2</sub> +H → CH <sub>3</sub> CH <sub>2</sub>	1/3	139	190	159	231	-63	37
		1/9	140	180	159	222	-23	61
TSi	CH <sub>3</sub> CH <sub>2</sub> → CH <sub>3</sub> CH+H	1/3	152	153	161	206, 224	33	88
		1/9	151	152	162	207, 225	6	74
TSj	CH <sub>3</sub> CH <sub>2</sub> +H → CH <sub>3</sub> CH <sub>3</sub>	1/3	151	148	169, 214	229	-17	67
		1/9	151	150	168, 216	228	12	77

<sup>a</sup> A–B, distance between atoms A and B in the transition state. <sup>b</sup> For the designation of the reactions and transition states, see also Fig. 3.1. <sup>c</sup> Distances that characterize the bonds that are broken/formed during the reaction. <sup>d</sup> Reaction energy. <sup>e</sup> Activation energy.

**Vinyl to Ethynidyne (TSe).** In this hydrogenation reaction, at low coverage (1/9), the attacking hydrogen is placed at the three-fold site which is in front of the C atom of the CH<sub>2</sub> group. The isolated H atom approaches the C atom of the CH<sub>2</sub> group from a top site in the transition state TSe (Fig. 3.3), with the C–H distance of the bond to be formed decreasing from 270 pm in the initial state to 156 pm. Concurrently, the H–Pt distance stretches to 160 pm. Due to the attacking H atom, the C–Pt bond of the CH<sub>2</sub> group weakens, reflected in the

16 pm longer bond compared with the initial state. The reaction follows a different path at 1/3 coverage due to the high density of adsorbates. Now the hydrogenating H atom approaches the CH<sub>2</sub> group from the side via a bridge site, forming two unequal H–Pt bonds in TSe, 169 pm and 217 pm (Fig. 3.4). The reaction is exothermic by 20 kJ mol<sup>-1</sup> at this coverage (1/3), while the reaction is endothermic by 17 kJ mol<sup>-1</sup> at 1/9 coverage. The activation barrier was calculated at 65 kJ mol<sup>-1</sup> at 1/3 coverage and 78 kJ mol<sup>-1</sup> at 1/9 coverage.

**Vinyl to Vinylidene (TSf).** In the transition state TSf (Fig. 3.3), the dissociating H migrates over a top site, with the C–H bond elongating to 144 pm, and the forming H–Pt bond at 166 pm. The reacting C atom forms a third C–Pt bond, 215 pm, at a three-fold hollow site whereas the other C atom moves upwards and the corresponding C–Pt distance increases to 217 pm. In the final state, the dissociated H atom lands at a three-fold site near the adsorbed vinylidene. The reaction is endothermic by 32 kJ mol<sup>-1</sup> at 1/3 coverage and exothermic by 15 kJ mol<sup>-1</sup> at 1/9 coverage. The barrier of this reaction step is 69 kJ mol<sup>-1</sup> at 1/3 coverage and 53 kJ mol<sup>-1</sup> at 1/9 coverage.

**Vinylidene to Ethylidyne (TSg).** Similar to Reaction *e* at 1/9 coverage, in the initial state, the attacking hydrogen atom is located at a hollow site in front of the CH<sub>2</sub> group. In the transition state TSg (Fig. 3.3), this H atom moves to the top site, originally occupied by the CH<sub>2</sub> group, with H–Pt = 162 pm. In parallel, the CH<sub>2</sub> group is pushed upwards so that the corresponding C–Pt distance elongates, by 10 pm, to 233 pm at 1/9 coverage. At 1/3 coverage, due to a stronger repulsion between neighboring hydrocarbons, (Fig. 3.4), this value changes to 271 pm, from 232 pm in the initial state (Table 3.4). The C–H bond to be formed is still rather long in TSg, 181 pm at 1/3 coverage and 165 pm at 1/9 coverage. This reaction is strongly exothermic, by 87 kJ mol<sup>-1</sup> at 1/3 coverage and 36 kJ mol<sup>-1</sup> at 1/9 coverage. The activation energy of this elementary step changes concomitantly, from 58 kJ mol<sup>-1</sup> at 1/3 coverage to 80 kJ mol<sup>-1</sup> at 1/9 coverage.

**Ethylene to Ethyl (TSh).** An experiment<sup>75</sup> suggests  $\pi$  ethylene to be the key precursor of ethylene hydrogenation. However, at UHV conditions, only the di- $\sigma$  form of adsorbed ethylene was found to be stable on Pt(111) above 100K.  $\pi$  ethylene could be observed on the surface in the presence of hydrogen in notable concentrations. In this thesis, the TS structures of the reactions from both  $\pi$  and di- $\sigma$  ethylene to ethyl are located.

Unlike other three-member-ring transition states, the hydrogenation of the  $\pi$ -adsorbed

species proceeds via a five-member-ring transition state (TSh- $\pi$ , Fig. 3.3), which involves C and H atoms of the forming bond, the other C atom as well as two Pt atoms. In TSh- $\pi$ , the C–H distance of the forming bond is 180 pm, while the C–Pt bond is totally broken, stretching from 220 pm in the reactant state to 291 pm in the transition state. This reaction is strongly exothermic by 63 kJ mol<sup>-1</sup> at 1/3 coverage and 23 kJ mol<sup>-1</sup> at 1/9 coverage. The corresponding activation energy is 37 kJ mol<sup>-1</sup> at 1/3 coverage and 61 kJ mol<sup>-1</sup> at 1/9 coverage.

In the transition state of the hydrogenation for di- $\sigma$  ethylene (TSh- $\sigma$ , Fig. 3.3), the reacting H passes through an intermediate with bridge coordination. The H atom is at an asymmetric position, with H–Pt distances at 162 pm and 235 pm. The newly formed C–H bond is 154 pm. This reaction is exothermic by 15 kJ mol<sup>-1</sup> at 1/3 coverage and endothermic by 23 kJ mol<sup>-1</sup> at 1/9 coverage. The activation energy is 75 kJ mol<sup>-1</sup> at 1/3 coverage and 88 kJ mol<sup>-1</sup> at 1/9 coverage; both values are close to the result, 77 kJ mol<sup>-1</sup>, of an earlier calculation at 1/4 coverage.<sup>53</sup>

***Ethyl to Ethylidene (TSi).*** In the transition state TSi (Fig. 3.3), the hydrocarbon binds at the same bridge site as the product ethylidene. The dissociating H atom from the CH<sub>2</sub> moiety attaches to the surface over a top site whereby the C–H distance elongates to 152 pm and the H–Pt distance decreases to 162 pm. Simultaneously, the reactive C center creates a second C–Pt bond, 225 pm in TSi, at a neighboring bridge site. This reaction is endothermic by 33 kJ mol<sup>-1</sup> at 1/3 coverage and 6 kJ mol<sup>-1</sup> at 1/9 coverage. The calculated activation barriers are 88 kJ mol<sup>-1</sup> at 1/3 coverage and 74 kJ mol<sup>-1</sup> at 1/9 coverage for this reaction.

***Ethyl to Ethane (TSj).*** In the transition state TSj (Fig. 3.3), the attacking H atom moves to a bridge site which shares the Pt atom with ethyl bound on it. The two unequal H–Pt distances are 168 pm and 214 pm, and the newly formed C–H bond length is 148 pm. This reaction is exothermic by 17 kJ mol<sup>-1</sup> at 1/3 coverage and endothermic by 12 kJ mol<sup>-1</sup> at 1/9 coverage. The obtained activation barrier for this reaction step is 67 kJ mol<sup>-1</sup> at 1/3 coverage and 77 kJ mol<sup>-1</sup> at 1/9 coverage for this reaction.

### 3.2.3 Coverage effect on the individual reactions

There are three kinds of reactions: hydrogenation, dehydrogenation and 1,2–H shift reactions. Additional H atoms are needed or produced in the initial or final states for the hydrogenation and dehydrogenation reactions, respectively. A coadsorbed H atom occupies a separate

adsorption site. Consequently, the lateral repulsion between the adsorbates is more prominent at higher than at lower coverage. This is reflected in the coverage-dependence of the reaction energies. In general, as the coverage increases from 1/9 to 1/3, hydrogenation reactions become more exothermic, by 30–50 kJ mol<sup>-1</sup>; the situation is reversed for dehydrogenation reactions (Table 3.4). Meanwhile, barriers for hydrogenation reactions are typically lower at high coverage (1/3), by 10–25 kJ mol<sup>-1</sup>, than the corresponding barriers at low coverage (1/9). In contrast, barriers of dehydrogenation reactions have been calculated 10–20 kJ mol<sup>-1</sup> higher at high coverage (1/3) than at low coverage (1/9). For the 1,2-H shift reactions, the surface coverage is nearly the same during the reaction. In such cases, the reaction energies do not vary a lot. However, the barriers decrease by 27 kJ mol<sup>-1</sup> when the coverage decreases from 1/3 to 1/9; currently, there is no detailed explanation of such coverage dependence.

### 3.3. Three Mechanisms of Ethylene Conversion to Ethylidyne

The geometry and energetics of the individual reactions were described in the previous section. In this section, possible reaction scenarios which connect ethylene to ethylidyne on Pt(111) are analyzed, based on the details of individual reactions.

The reaction network in Fig. 3.1 contains several reaction pathways that connect ethylene and ethylidyne. The calculated results show that the barriers for direct 1,2-H shift reactions are as high as ~170 kJ mol<sup>-1</sup>, i.e., vinyl to ethylidyne, much higher than the barriers of hydrogenation / dehydrogenation reactions. Thus, direct shift reactions, Reactions *b* and *c* (Fig. 3.1), can safely be excluded. Three reaction pathways contain only hydrogenation / dehydrogenation reactions: (M1) ethylene → vinyl → ethylidene → ethylidyne; (M2) ethylene → vinyl → vinylidene → ethylidyne; (M3) ethylene → ethyl → ethylidene → ethylidyne. Some of the elementary steps are shared between these mechanisms. The reaction landscapes of the three mechanisms are depicted in Fig. 3.5.

#### 3.3.1 Reaction in the absence of hydrogen.

After ethylene adsorbs on Pt(111), it can be either dehydrogenated to vinyl or hydrogenated to ethyl. Due to the need of an additional H for the hydrogenation step, at UHV conditions and without hydrogen coadsorbed, ethylene can only be dehydrogenated. Thus, only mechanisms M1 and M2 seem plausible at such conditions. In the following, I will focus on the discussion of the competition between M1 and M2 at various coverages.

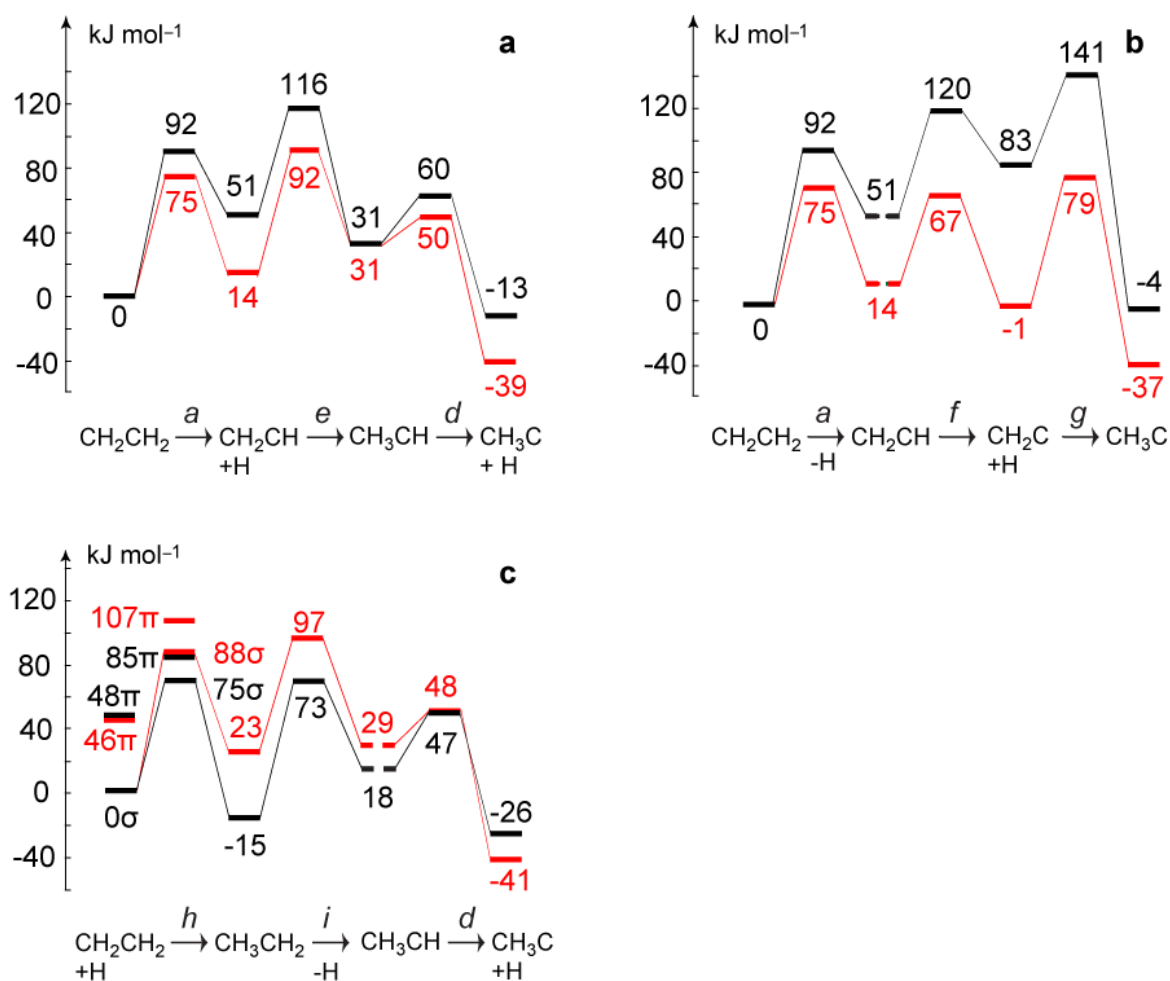


**Figure 3.5.** Reaction energy profiles ( $\text{kJ mol}^{-1}$ ) of ethylene conversion to ethylidyne over Pt(111) via various mechanisms: (a) (M1) ethylene  $\rightarrow$  vinyl  $\rightarrow$  ethylidene  $\rightarrow$  ethylidyne; (b) (M2) ethylene  $\rightarrow$  vinyl  $\rightarrow$  vinylidene  $\rightarrow$  ethylidyne; (c) (M3) ethylene  $\rightarrow$  ethyl  $\rightarrow$  ethylidene  $\rightarrow$  ethylidyne (see Fig. 1), at 1/3 coverage (black) and 1/9 coverage (red). In panels (b) and (c) one state energy is represented as a broken line to indicate a change in reference when calculating relative energies. The relative energies to the left are calculated with respect to di- $\sigma$  ethylene in (a) and (b) or di- $\sigma$  ethylene+H in (c) at the various coverages. The relative energies to the right are shifted by the energy difference of vinyl and vinyl+H in (b) or ethylidene and ethylidene+H in (c).

M1 and M2 share the same first step, the dehydrogenation of ethylene to vinyl (Reaction *a*). After this first dehydrogenation step, vinyl can be hydrogenated to ethylidene (M1) or further dehydrogenated to vinylidene (M2). Both products can be converted to ethylidyne via one step, dehydrogenation or hydrogenation reactions, respectively.

Fig. 3.6 compares the reaction landscapes of these steps. The shared Reaction *a* is not

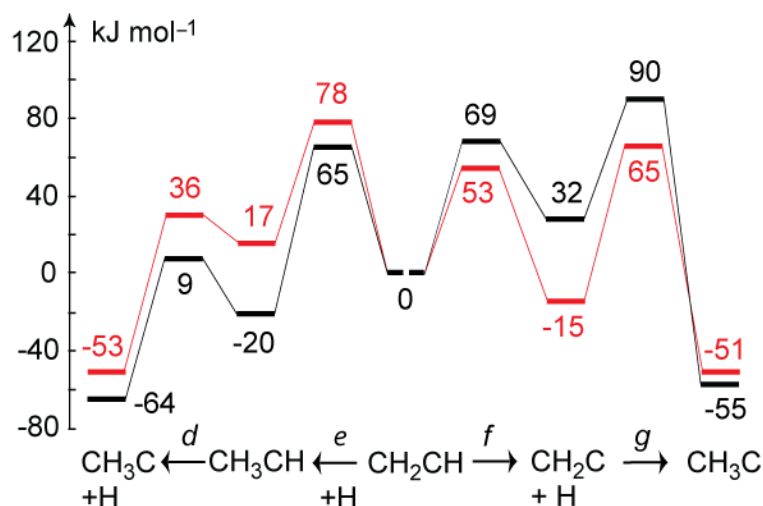


**Figure 3.6.** Reaction energy profiles ( $\text{kJ mol}^{-1}$ ) of vinyl conversion to ethylidyne over Pt(111) at 1/3 coverage (black) and 1/9 coverage (red): comparison of routes via vinylidene ( $e$ - $d$ , energies with respect to  $\eta^2\mu_3$ -vinyl coadsorbed with H) and via ethylidene ( $f$ - $g$ , energies with respect to  $\eta^2\mu_3$ -vinyl).

included in this figure. The barriers of this step are  $75 \text{ kJ mol}^{-1}$  at low (1/9) coverage and  $92 \text{ kJ mol}^{-1}$  at high (1/3) coverage. In both mechanisms, the highest reaction barriers are similar,  $\sim 80 \text{ kJ mol}^{-1}$  at low (1/9) coverage via Reactions  $e$  and  $g$ , respectively, and of  $92 \text{ kJ mol}^{-1}$  via Reaction  $a$  at high (1/3) coverage. These highest barrier values,  $80$ – $92 \text{ kJ mol}^{-1}$ , are very reasonable for a reaction that occurs at  $\sim 250$ – $300 \text{ K}$ , and they are also in good agreement with the reported apparent barrier,  $60$ – $77 \text{ kJ mol}^{-1}$ , from various experiments for the overall transformation to ethylidyne.<sup>86–89</sup> The preference of M1 or M2 at different coverages depends on the second step (Reactions  $e$  and  $f$ ) (Fig. 3.6). Low coverage prefers M1 with  $65 \text{ kJ mol}^{-1}$  barrier (Reaction  $e$ ) followed by Reaction  $d$  with a barrier of only  $29 \text{ kJ mol}^{-1}$ . The barrier of Reaction  $f$  in M2 is slightly higher, by only  $4 \text{ kJ mol}^{-1}$ , than Reaction  $e$  in M1, but the former reaction is strongly endothermic by  $32 \text{ kJ mol}^{-1}$ , indicating that the reverse of that reaction is fast, thus preventing further conversion to ethylidyne via M2. At high coverage, M2 is more preferred due to the  $25 \text{ kJ mol}^{-1}$  lower barriers for Reaction  $f$  compared with Reaction  $e$  in M1 (Fig. 3.6).

The calculated barriers also show that the rate-limiting step of ethylene conversion to ethylidyne evidently changes with coverage. At high coverage, the shared first step, Reaction  $a$ , is rate-limiting; the barrier of this step is at least  $23 \text{ kJ mol}^{-1}$  higher than the barriers of the other steps. However, this barrier is dramatically decreased to  $75 \text{ kJ mol}^{-1}$  at low coverage, which is slightly lower than the barriers of the two subsequent hydrogenation reactions,

Reactions *e* and *g*. Interestingly, a former kinetic study by Zaera and French<sup>70</sup> indicates that the rate-limiting step of the overall conversion indeed changes with coverage. In their study, the ratio of hydrogen to deuterium released in the dehydrogenation of trideuterioethylene was monitored. The release of deuterium was enhanced with respect to the ratio expected from stoichiometry at low coverages, whereas the enhancement in hydrogen was observed at saturation. Based on this observation, these authors proposed a two-step mechanism, via reaction *c* and *d* (Fig. 3.1). The isotope effect makes the reaction go faster with H than with D atoms. Thus, it must be associated with the C–H or C–D bond-breaking steps as rate-limiting in the conversion. They proposed that at low coverage, the isomerization step *c* would become rate-limiting, with an initial pre-equilibrium between ethylene and ethylidene and a rate-limiting H-dissociation step *d* at saturation. This suggestion would be consistent with the enhanced H desorption at saturation because H involved in the rate-limiting dehydrogenation step is faster. However, if a rate-limiting step was hydrogenation at low coverage, faster H consumption could also lead to an enhanced release of deuterium. Hence, this experimental evidence is consistent with both M1 and M2.

Recall that vinyl intermediate as precursor of ethylidyne was ruled out by Zaera et al.<sup>68</sup> because vinyl was shown to convert back to ethylene before producing ethylidyne on Pt(111). To gain further understanding, those TPD results can be discussed in the light of the present theoretical results. The coverage of vinyl iodide as estimated in Ref. 68 ( $\theta = 0.12\text{--}0.13$ ) roughly corresponds to the calculated reaction landscape at 1/9 coverage. According to the calculated reaction barriers, at thermal heating, vinyl on the surface would convert to vinylidene with a relatively low barrier,  $53 \text{ kJ mol}^{-1}$ . Subsequently, it could convert to ethylene with a slightly higher barrier of  $61 \text{ kJ mol}^{-1}$ . Further heating of the system would finally convert surface ethylene to ethylidyne, which can be formed either via vinyl and ethylidene or directly from vinylidene, with barriers of  $80 \text{ kJ mol}^{-1}$  in both cases. Such a prediction qualitatively agrees with the experimental observations: the formation of vinylidene was identified at  $\sim 130 \text{ K}$ , then ethylene was formed in the region of  $200 \text{ K}$ , and ethylidyne appeared after heating above  $300 \text{ K}$ .<sup>68</sup>

Actually, these findings do not rule out vinyl as intermediate in the conversion of ethylene to ethylidyne. As discussed above, at low coverage, ethylene was formed at about  $200 \text{ K}$ ,<sup>68</sup> with  $61 \text{ kJ mol}^{-1}$  barrier. However, vinyl can be regenerated at higher temperature in the conversion of ethylene to ethylidyne because of the higher barrier,  $92 \text{ kJ mol}^{-1}$ , for

ethylene dehydrogenation to vinyl (Reaction *a*) compared with the reaction from vinyl to ethylene. Moreover, the former barrier is higher than the barriers of the proceeding steps, vinyl to ethylidyne via vinylidene (80 kJ mol<sup>-1</sup>) or ethylidene (78 kJ mol<sup>-1</sup>). Therefore, Reaction *a* is rate-limiting in the conversion from ethylene to ethylidyne via M1 or M2, and vinyl could not accumulate on the surface, which consists with an intermediate observed during this process by previous experiment.<sup>68</sup>

### 3.3.2 Reaction under hydrogenation conditions.

In most practical situations, e.g. in hydrogenation of ethylene, the formation of ethylidyne from ethylene occurs as a side reaction. In such cases, the reaction takes place in an atmosphere with a sufficient amount of hydrogen. Thus, mechanism M3, which involves an initial hydrogenation of ethylene to ethyl, could compete with other reaction mechanism, like M1 or M2. The energy profile of M3 is shown in Fig. 3.5c.

The first step of this mechanism is the hydrogenation of ethylene. Unlike the dehydrogenation of ethylene, previous *in situ* SFG experiment<sup>75</sup> suggested  $\pi$ -bound ethylene as likely primary intermediate of ethylene hydrogenation. In the present calculations, hydrogenation from both  $\pi$ -bound or di- $\sigma$  ethylene was investigated. Indeed, the optimized reaction path shows a notably lower activation energy for the hydrogenation of  $\pi$ -ethylene than of di- $\sigma$  ethylene. At high coverage (1/3), the activation energy for the former case is only 37 kJ mol<sup>-1</sup>, i.e., 38 kJ mol<sup>-1</sup> lower than the corresponding barrier of di- $\sigma$ -ethylene (Table 3.4). The barrier increases slightly to 61 kJ mol<sup>-1</sup> at low coverage (1/9), but it is still lower than that of the corresponding reaction of di- $\sigma$  ethylene (75 kJ mol<sup>-1</sup>). Both values of hydrogenation barriers of  $\pi$ -ethylene are rather low, showing that the hydrogenation of  $\pi$ -ethylene should be much easier than that of di- $\sigma$ -ethylene at either high or low coverage.

The hydrogenation barrier of  $\pi$ -ethylene is not only lower than the corresponding barrier of di- $\sigma$  ethylene, but also lower than the dehydrogenation barrier of ethylene to vinyl, which is the first step of mechanisms M1 or M2. At high coverage (1/3), the barrier for the dehydrogenation reaction, 92 kJ mol<sup>-1</sup>, is 55 kJ mol<sup>-1</sup> higher than the hydrogenation of  $\pi$ -ethylene. Actually, it is also slightly higher than the hydrogenation barrier of di- $\sigma$  ethylene, by 4 kJ mol<sup>-1</sup>. Both results indicate M3 to be energetically more favorable than M1 or M2. At low coverage (1/9), the obtained activation energy for the hydrogenation of ethylene, 61 and 88 kJ mol<sup>-1</sup> for  $\pi$  and di- $\sigma$  mode respectively, are comparable with the barriers of the first

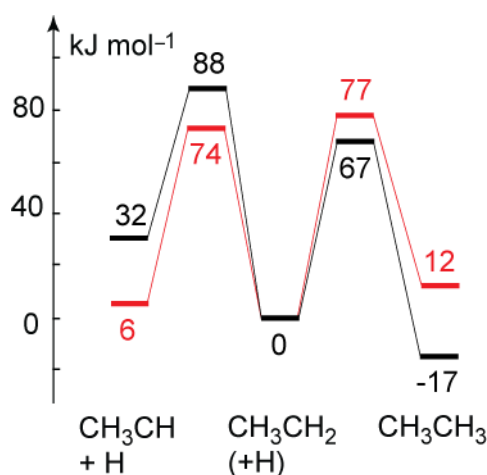


**Figure 3.7.** Reaction energy profiles (kJ mol<sup>-1</sup>) of ethyl conversion to ethylidene or ethane over Pt(111) at 1/3 coverage (black) and 1/9 coverage (red).

dehydrogenation step in M1 and M2, 75 kJ mol<sup>-1</sup>, which suggests that M3 may at least be equally probable.

Several further aspects need to be considered besides the simple comparison of the activation energies. First, the first hydrogenation step requires a significant concentration of hydrogen on the surface. For example, Frei et al.<sup>90, 91</sup> observed ethyl during ethylene hydrogenation over a Pt/Al<sub>2</sub>O<sub>3</sub> catalyst via peaks at 2893 cm<sup>-1</sup> and 1200 cm<sup>-1</sup> by time-resolved Fourier-transform infrared spectroscopy; however, these peaks were absent when the reactant mixture did not contain hydrogen gas. Second, the existence of  $\pi$ -ethylene on Pt(111) requires the presence of (external) ethylene in the gas phase<sup>16</sup> or certain coadsorbates.<sup>9-11</sup> Finally, if enough surface H atoms exist after ethylene is hydrogenated to ethyl, the latter could be further hydrogenated to ethane which would irreversibly desorb from the surface. At low (1/3) coverage, the barrier for this process is only 67 kJ mol<sup>-1</sup>, i.e., 21 kJ mol<sup>-1</sup> lower than the activation energy of ethyl dehydrogenation to ethylidene (Fig. 3.7). At high (1/9) coverage, the activation energies for hydrogenation and dehydrogenation of ethyl are comparable, 77 and 74 kJ mol<sup>-1</sup>, respectively. Therefore, in the presence of excess hydrogen, hydrogenation to ethane via parts of mechanism M3 should strongly compete with the dehydrogenation to ethylidene and ethylidyne.

### 3.4. Remark on a spectroscopically identified transient intermediate.

The transformation of ethylene to a stable surface species over transition metal surfaces was observed a long time ago, but identification of these puzzling species succeeded only in the

1970s. It was confirmed to be ethylidyne with the help of high resolution electron energy loss spectroscopy (HREELS) and LEED.<sup>17</sup> However, the reaction mechanism of this conversion was unclear due to the short lifetime of the intermediates. Even some of the intermediates could be detected, but the signals contained only several weak peaks which were mixed up with the ones belonging to the dominant stable species on the surface. Therefore, these intermediates were even harder to identify than the stable species. The mechanism of the conversion of ethylene to ethylidyne on Pt(111) was controversially debated until 1995. With SFG<sup>62</sup> and RAIRS<sup>63</sup> spectroscopy, a peak at 2957–2960  $\text{cm}^{-1}$  was observed and assigned to the asymmetric stretch of the methyl group of ethylidene. Another peak at 1387  $\text{cm}^{-1}$  was identified in the latter study. It developed in parallel with the 2960  $\text{cm}^{-1}$  feature and was assigned to the  $\text{CH}_3$  symmetric bend of ethylidene. These two rather weak IR signals from transient species were beyond the sensitivity limits of previous spectroscopic experiments.

However, based on the calculated results in this thesis, the barrier for the conversion from ethylidene to ethylidyne is less than 30  $\text{kJ mol}^{-1}$ , which is much lower than a typical hydrogenation / dehydrogenation barrier in this conversion. Such a low barrier would imply a fast conversion from ethylidene to ethylidyne, thus ethylidene is expected to be hardly accumulated during the reaction. Recent kinetic Monte Carlo (kMC) simulations<sup>92</sup> confirmed this hypothesis, which showed that instead of ethylidene, vinylidene could be accumulated over the surface during ethylene conversion.

One possible reason for this contradiction is the method for the assignment of vibrational modes. In many cases, one assumes a similarity between the spectrum of surface species with another spectrum of a related (molecular) compound of known structure, e. g. an organometallic analogue.<sup>93, 94</sup> This approach may lead to a wrong identification<sup>95</sup> due to the similarity of the vibrational modes of species with slightly different functional groups. On the other hand, theoretical calculations could directly determine the frequency of each vibrational mode, thus give direct evidence for the assignment of each peak in the spectrum. In this section, the vibrational normal mode analysis is done for both surface species and organometallic analogues.

Due to the strong anharmonicity of C–H stretching modes, the calculated harmonic frequencies are generally too high compared to the experimental values. The determined anharmonicity constants of such modes by experiment lie in the region 60–70  $\text{cm}^{-1}$ .<sup>96,97</sup> Even larger anharmonic corrections are reported by the calculations based on density functional

**Table 3.5** Calculated vibrational frequencies<sup>a</sup> of ethylidyne on Pt(111) as well as in Co<sub>3</sub>(CO)<sub>8</sub>(μ<sub>3</sub>-η<sup>1</sup>-CCH<sub>3</sub>) for two coverages  $\theta$  and assignment<sup>b</sup> of the normal modes

		f <sub>slab</sub>	f <sub>MO</sub>			Assignment
$\theta = 1/9^c$	$\theta = 1/3^c$	Exp	Calc (solid) <sup>c</sup>	Calc (gas) <sup>d</sup>	Exp <sup>e</sup>	
3032	3018	2950 <sup>m</sup> , 2939 <sup>i</sup>	3020	3004	2930	CH <sub>3</sub> ν <sub>a</sub>
3030	3012		3017			CH <sub>3</sub> ν <sub>a</sub>
2964	2938	2884 <sup>k</sup> , 2885 <sup>j</sup> , 2886 <sup>h</sup> , 2887 <sup>i,l</sup> , 2890 <sup>m</sup> , 2900 <sup>f</sup>	2953	2923	2888	CH <sub>3</sub> ν <sub>s</sub>
1403	1407		1419	1402	1420	CH <sub>3</sub> δ <sub>a</sub>
1402	1407	1420 <sup>m</sup> , 1444 <sup>i</sup>	1414			CH <sub>3</sub> δ <sub>a</sub>
1330	1326	1338 <sup>l</sup> , 1339 <sup>k</sup> , 1340 <sup>i,j</sup> , 1350 <sup>m</sup> , 1360 <sup>f</sup>	1354	1353	1356	CH <sub>3</sub> δ <sub>s</sub>
1095	1107	1115 <sup>j</sup> , 1118 <sup>k</sup> , 1124 <sup>i</sup> , 1126 <sup>l</sup> , 1130 <sup>f,m</sup>	1165	1220	1163	CC ν
957	962	900 <sup>f</sup> , 975 <sup>i</sup> , 980 <sup>m</sup>	997	991	1004	CH <sub>3</sub> ρ <sub>s</sub>
957	961		993		1004	CH <sub>3</sub> ρ <sub>s</sub>

<sup>a</sup> Only normal modes with calculated frequencies above ~900 cm<sup>-1</sup> are shown. <sup>b</sup> Notations used: ν, stretching; δ, bending; τ, twisting; ω, wagging; ρ, rocking; a, asymmetric; s, symmetric; ip, in-plane. <sup>c</sup> this work <sup>d</sup> Ref. 102. <sup>e</sup> Ref. 103. <sup>f</sup> Ref. 95. <sup>h</sup> Ref. 62. <sup>i</sup> Ref. 63. <sup>j</sup> Ref. 99. <sup>k</sup> Ref. 100. <sup>l</sup> Ref. 101. <sup>m</sup> Ref. 9.

theory, 100–160 cm<sup>-1</sup>, for C–H stretching frequencies of organic species.<sup>98</sup> This prevents a straightforward comparison of calculated and experimental frequencies in the present case. Thus, the discussion is mainly focused on modes other than C–H stretching. The calculated frequencies and the corresponding experimental values are listed in Tables 3.5–3.7.

### 3.4.1 C<sub>2</sub>H<sub>x</sub> (x = 3–4) on the Pt(111) surface

**Ethylidyne.** The most intense mode of ethylidyne on Pt(111) observed by RAIRS is the CH<sub>3</sub> symmetric bending (umbrella) mode,<sup>9,63,95,99-101</sup> which falls in the range 1338–1360 cm<sup>-1</sup>. The calculated results, at 1326 cm<sup>-1</sup> (1/3 ML) and 1330 (1/9 ML) cm<sup>-1</sup>, are slightly lower than the experimental results. Frequencies similarly to low are also obtained for the other modes. Calculated values for C–C stretching mode are 1107 (1/3 ML), 1095 (1/9 ML) cm<sup>-1</sup>, while the experiment values<sup>9,63,95,99-101</sup> are in the range of 1115–1130 cm<sup>-1</sup>. The double degenerated CH<sub>3</sub>

**Table 3.6** Calculated vibrational frequencies<sup>a</sup> of ethylene in Os<sub>2</sub>(CO)<sub>6</sub>(μ<sub>2</sub>-η<sup>2</sup>-CH<sub>2</sub>CH<sub>2</sub>) and on Pt(111) for two coverages  $\theta$  and assignment<sup>b</sup> of the normal modes

		f <sub>slab</sub>		f <sub>MO</sub>		Assignment
$\theta = 1/9$	$\theta = 1/3$	Exp		Cal	Exp <sup>d</sup>	
3080	3099			3067	2936	CH <sub>2</sub> v <sub>a</sub>
3057	3076	3000 <sup>k</sup>		3049	2917	CH <sub>2</sub> v <sub>a</sub>
2996	3016	2903 <sup>h</sup> , 2904 <sup>f</sup> , 2908 <sup>g</sup> , 2920 <sup>k</sup> , 2940 <sup>e</sup>		3011	2910	CH <sub>2</sub> v <sub>s</sub>
2986	3009			3004	2843	CH <sub>2</sub> v <sub>s</sub>
1421	1418	1414 <sup>h</sup> , 1416 <sup>g</sup> , 1420 <sup>e</sup> , 1430 <sup>j</sup>		1456	1445	CH <sub>2</sub> δ
1394	1400			1442	1434	CH <sub>2</sub> δ
1184	1229	1230 <sup>e</sup>		1230	1225	CH <sub>2</sub> ρ
980	1013	980 <sup>k</sup> , 990 <sup>e</sup> , 993 <sup>h</sup> , 995 <sup>g</sup>		1135	1144	CH <sub>2</sub> ω
1045 <sup>c</sup>	1089			1079 <sup>c</sup>	1083	CH <sub>2</sub> ω / CC v
934	929			1015	1012	CH <sub>2</sub> ρ
1048	1024	1042 <sup>g</sup> , 1047 <sup>h</sup> , 1050 <sup>k</sup>		1010 <sup>c</sup>	981	CC v / CH <sub>2</sub> ω
789	776	790 <sup>e, k</sup>		841	837	CH <sub>2</sub> τ
641	614	660 <sup>k</sup>		758	754	CH <sub>2</sub> τ

<sup>a</sup> Only normal modes with calculated frequencies above ~600 cm<sup>-1</sup> are shown. <sup>b</sup> Notations used: v, stretching; δ, bending; τ, twisting; ω, wagging; ρ, rocking; a, asymmetric; s, symmetric; ip, in-plane. <sup>c</sup> The admixture of the second mode is very weak. <sup>d</sup> Ref. 104. <sup>e</sup> Ref. 95. <sup>f</sup> Ref. 62. <sup>g</sup> Ref. 63. <sup>h</sup> Ref. 99. <sup>i</sup> Ref. 100. <sup>j</sup> Ref. 101. <sup>k</sup> Ref. 9.

asymmetric bending is calculated at 1407 (1/3 ML) and 1402–1403 (1/9 ML) cm<sup>-1</sup>. The previous experiments<sup>9,63</sup> reported these bands at 1420–1444 cm<sup>-1</sup>. The calculated CH<sub>3</sub> symmetric rocking modes are at 961–962 (1/3 ML), 957 (1/9 ML) cm<sup>-1</sup>, which are about 20 cm<sup>-1</sup> lower than the experimental values, 975–980 cm<sup>-1</sup>.<sup>9,63</sup>

**Ethylene.** Again, the discussion is focused on the modes which are not C–H stretching. CH<sub>2</sub> scissoring is the mode with the highest frequency, calculated at 1418 (1/3 ML), 1421 (1/9 ML) cm<sup>-1</sup>. It falls perfectly in the range reported by experiment, 1414–1430 cm<sup>-1</sup>. The CH<sub>2</sub> rocking mode varies a lot at different coverages. At high coverage (1/3), the calculated

**Table 3.7** Calculated vibrational frequencies<sup>a</sup> of vinyl in Os<sub>3</sub>(CO)<sub>10</sub>(μ-H)(μ-η<sup>2</sup>-CHCH<sub>2</sub>) and on Pt(111) for two coverages  $\theta$  and assignment<sup>b</sup> of the normal modes

$f_{\text{slab}}$		Assignment	$f_{\text{MO}}$			
$\theta = 1/9$	$\theta = 1/3$		Calc.	Exp. <sup>c</sup>	Exp. <sup>d</sup>	Assignment
3023	3016	CH <sub>2</sub> v <sub>a</sub>	3160	3052	3062	CH <sub>2</sub> v <sub>a</sub> / CH v
2995	3007	CH v	3135	2998	2997	CH v / CH <sub>2</sub> v <sub>a</sub>
2959	2949	CH <sub>2</sub> v <sub>s</sub>	3069	2920	2920	CH <sub>2</sub> v <sub>s</sub>
1381	1386	CH <sub>2</sub> δ	1481	1476	1475	CH <sub>2</sub> δ
1099	1108	CH δ <sub>ip</sub> /CC v	1311	1310	1311	CC v
1060	1064	CC v/CH <sub>2</sub> ω/CH δ <sub>ip</sub>	1258	1266	1266	CH <sub>2</sub> ρ / CH δ <sub>ip</sub>
994	1013	CH <sub>2</sub> ρ	1009	1005	1009	CH <sub>2</sub> ω / CH δ <sub>op</sub>
949	959	CH <sub>2</sub> ω / CH δ <sub>ip</sub>	997	990	990	CH <sub>2</sub> ω / CH δ <sub>ip</sub>
730	732	CH <sub>2</sub> ρ / CH δ <sub>op</sub>	993	987		CH <sub>2</sub> τ / CH δ <sub>op</sub>
665	666	CH <sub>2</sub> τ / CH δ <sub>op</sub>	802	782	786	CH <sub>2</sub> τ / CH δ <sub>op</sub>

<sup>a</sup> Only normal modes with calculated frequencies above  $\sim 600 \text{ cm}^{-1}$  are shown. <sup>b</sup> Notations used: v, stretching; δ, bending; τ, twisting; ω, wagging; ρ, rocking; a, asymmetric; s, symmetric; ip, in-plane.

<sup>c</sup> Ref. 105. <sup>d</sup> Ref. 106.

frequency is  $1229 \text{ cm}^{-1}$ , which essentially reproduces the experiment value  $1230 \text{ cm}^{-1}$ . However, at low coverage (1/9), it is calculated to shift to a lower frequency,  $1184 \text{ cm}^{-1}$ . A similar behavior is observed for the CH<sub>2</sub> wagging mode,  $1089 \text{ cm}^{-1}$  at 1/3 coverage and  $1048 \text{ cm}^{-1}$  at 1/9 coverage. The corresponding experimental results, between  $1042 \text{ cm}^{-1}$  and  $1050 \text{ cm}^{-1}$ , are again very close to the calculated value at low coverage. A mixed mode, CH<sub>2</sub> wagging and C–C stretching, is calculated at  $1013 \text{ cm}^{-1}$  (1/3 ML),  $980 \text{ cm}^{-1}$  (1/9 ML), very close to the experimental values,  $980\text{--}995 \text{ cm}^{-1}$ . Some other calculated bands, not observed by experiments, are as follows: CH<sub>2</sub> scissoring at  $1400 \text{ cm}^{-1}$  (1/3 ML),  $1394 \text{ cm}^{-1}$  (1/9 ML); a mixture of CH<sub>2</sub> wagging and C–C stretching at  $1089 \text{ cm}^{-1}$  (1/3 ML),  $1045 \text{ cm}^{-1}$  (1/9 ML); CH<sub>2</sub> rocking at  $929 \text{ cm}^{-1}$  (1/3 ML),  $934 \text{ cm}^{-1}$  (1/9 ML); CH<sub>2</sub> twisting modes at  $776 \text{ cm}^{-1}$  and  $614 \text{ cm}^{-1}$  (1/3 ML) as well as at  $789 \text{ cm}^{-1}$  and  $641 \text{ cm}^{-1}$  (1/9 ML)  $\text{cm}^{-1}$ .

**Vinyl.** There are no directly measured spectra for vinyl over Pt(111) surface because vinyl is not a stable species on the surface. Previous research on vinyl halide adsorption over

Pt(111) by Zaera and Bernstein<sup>68</sup> reported the spectrum for vinyl, with the assumption that the C–X bond is broken after adsorption at low temperature. In such case, the C=C double bond would still exist, as reflected by the strong adsorption peak at about 1600 cm<sup>-1</sup>. Note that the co-adsorption of halide does not affect the spectrum of the hydrocarbon, e.g. the peaks at 1340 cm<sup>-1</sup> and 1128 cm<sup>-1</sup> for ethylidyne co-adsorbed with iodide<sup>68</sup> which are close to the values without iodide in Table 3.5. Thus, the adsorption mode of vinyl on Pt(111), generated from vinyl halide, differs from the results of our calculation which predicted adsorption in  $\mu_3$ - $\eta^2$  fashion with only a C–C single bond of 147 pm. Indeed, besides the  $\mu_3$ - $\eta^2$  adsorbed complex, vinyl can be adsorbed at a top site in  $\eta^1$  fashion, preserving C=C, which is confirmed by the current DFT calculations. The vibrational normal mode analysis shows the C=C stretching mode of  $\eta$ -vinyl located at 1537–1547 cm<sup>-1</sup>, close to the experimentally observed frequencies about 1600 cm<sup>-1</sup>. However,  $\eta$ -vinyl is not included in the conversion of ethylene to ethylidyne because it is calculated 58 kJ mol<sup>-1</sup> and 75 kJ mol<sup>-1</sup> less stable than  $\eta^2$ - $\mu_3$ -vinyl at 1/3 and 1/9 coverage, respectively

The different adsorption mode between the calculated  $\mu_3$ - $\eta^2$  fashion and the experimental  $\eta$  fashion prevents a comparison of the vibrational modes. Hence, only the calculated results are listed: CH<sub>2</sub> scissoring at 1386 cm<sup>-1</sup> (1/3 ML), 1381 cm<sup>-1</sup> (1/9 ML); a mixture of CH in-plane bending and C–C stretching at 1108 cm<sup>-1</sup> (1/3 ML), 1099 cm<sup>-1</sup> (1/9 ML); a mixture of C–C stretching, CH<sub>2</sub> wagging, and CH in-plane bending at 1064 cm<sup>-1</sup> (1/3 ML), 1060 cm<sup>-1</sup> (1/9 ML); CH<sub>2</sub> rocking 1013 cm<sup>-1</sup> (1/3 ML), 994 cm<sup>-1</sup> (1/9 ML).

**Summary of the comparison for C<sub>2</sub>H<sub>x</sub> over Pt(111).** In most cases, the calculated vibrational frequencies of the stable species (ethylidyne and ethylene) lie within the intervals spanned by the values from various experiments,<sup>9,63,95,99-101</sup> with most of the deviation below 40 cm<sup>-1</sup>. Such deviation could be attributed to the complexity of the surface environment, e. g. different coverage or co-adsorbed species, leading to frequency shifts of specific vibrational modes, as well as the limited accuracy of GGA methods for vibrational frequencies. The calculations clearly show that vibrational frequencies may shift by 50 cm<sup>-1</sup> depending on different coverage. Smaller range is reported by the experiment, about 25 cm<sup>-1</sup>. It is fair to say that our DFT calculations describe the vibrational frequencies of C<sub>2</sub> species over the Pt(111) surface quite well.

### 3.4.2 C<sub>2</sub>H<sub>x</sub> (x = 3–4) in organometallic clusters

Three organometallic clusters, Co<sub>3</sub>(CO)<sub>9</sub>(CCH<sub>3</sub>),<sup>36,103</sup> Os<sub>2</sub>(CO)<sub>6</sub>(CH<sub>2</sub>CH<sub>2</sub>)<sup>37,104</sup> and Os<sub>3</sub>(CO)<sub>10</sub>(μ-H)(CHCH<sub>2</sub>),<sup>38,105,106</sup> were selected for comparison. For the first two clusters, the hydrocarbon part has a similar local adsorption mode as on the Pt(111) surface. However, this is not the case for the third organometallic cluster with the vinyl group. It was selected for two reasons: *i*) To the best of my knowledge, there is no complex for vinyl with a more similar adsorption mode as on Pt(111) and *ii*) this complex was also selected in a previous experimental study<sup>68</sup> to help identifying surface species. All three organometallic clusters contain carbonyl ligands besides the hydrocarbon part which is of key interest. Fortunately, the vibration modes related to carbonyl groups are mostly around 2000 cm<sup>-1</sup> (stretching) or below 500 cm<sup>-1</sup> (bending). Test calculations for an isolated organometallic cluster showed that these modes do not mix with the vibrations related to the C<sub>2</sub>H<sub>x</sub> moiety (x = 3–4) part; C–H stretching modes usually exhibit frequencies around 3000 cm<sup>-1</sup> and bending modes in the range 600–1500 cm<sup>-1</sup>. Thus, those modes related to CO are not calculated in our vibrational normal mode analysis. On the other hand, the M–C stretching modes are considered as metal-dependent.<sup>102</sup> Since all metal moieties investigated differ from the Pt surface of interest, the low-frequency region which is related to the M–C stretching modes was also not calculated. Therefore, only the hydrocarbon part is included in the normal mode analysis of the vibrations.

**Co<sub>3</sub>(CO)<sub>9</sub>(CCH<sub>3</sub>).** Similar to ethynyl adsorbed over Pt(111), the CCH<sub>3</sub> group is attached to the Co triangle in μ<sub>3</sub> fashion (Fig. 3.8a). The optimized geometry is quite similar to the previous XRD result.<sup>36</sup> The calculated C–Co bond lengths, 190–191 pm, falls nicely in the range of the experimental results,<sup>36</sup> 186–193 pm. Early DFT results at the LDA level on isolated complexes<sup>102</sup> obtained a slightly shorter distance at 189 pm. The optimized C–C bond length is 148 pm, 1 pm longer than the bond length in gas phase calculation.<sup>102</sup> However, both of them are notably shorter, by 5 pm, than the XRD result.<sup>36</sup>

Leaving the high-frequency C–H stretching modes aside, one notes perfect matches between the calculated data and the experimental results,<sup>103</sup> with a maximum difference of 11 cm<sup>-1</sup> (Table 3.5). For example, the modes at 1419, 1354, 996 and 993 cm<sup>-1</sup> are assigned to CH<sub>3</sub> asymmetric bending, CH<sub>3</sub> symmetric bending (umbrella) and doubly degenerate CH<sub>3</sub> symmetric rocking, respectively. The corresponding modes reported by experiment<sup>103</sup> are

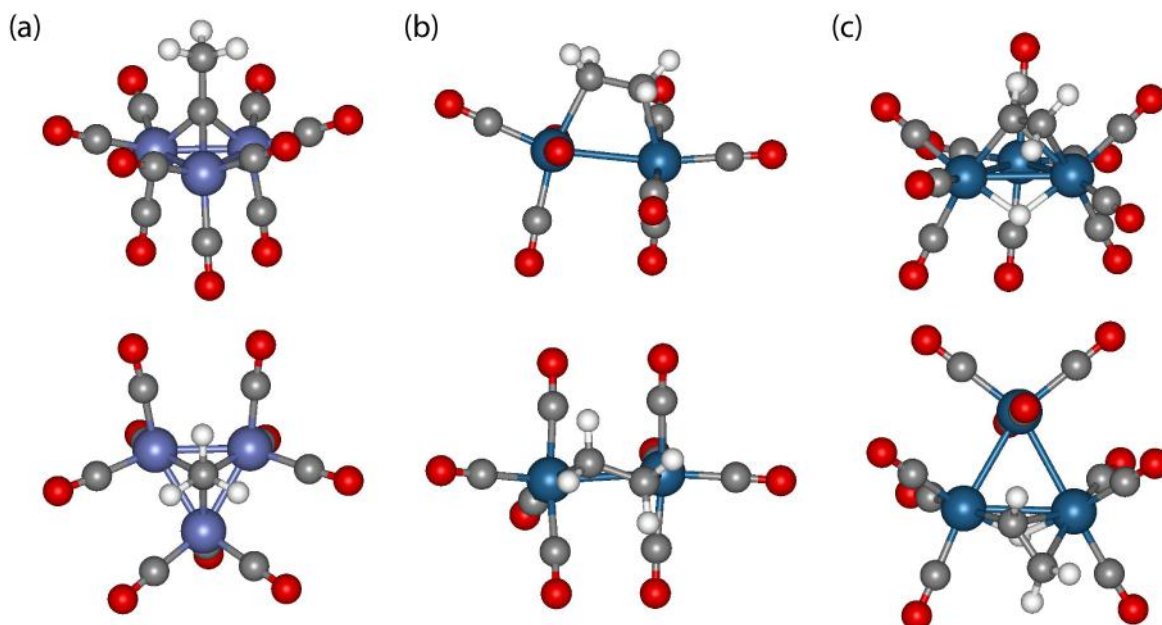


**Figure 3.8.** The structure of the optimized organometallic clusters: (a)  $\text{Co}_3(\text{CO})_9(\text{CCH}_3)$ ; (b)  $\text{Os}_2(\text{CO})_6(\text{CH}_2\text{CH}_2)$ ; (c)  $\text{Os}_3(\text{CO})_{10}(\mu\text{-H})(\text{CHCH}_2)$ . Colors: gray, carbon; white, hydrogen; red, oxygen; purple, cobalt; blue, osmium.

located at 1420, 1356 and 1004 (doubly degenerate)  $\text{cm}^{-1}$ , respectively. The gas phase DFT calculations<sup>102</sup> yielded slightly lower frequencies, at 1402  $\text{cm}^{-1}$ , 1353  $\text{cm}^{-1}$  and 991 (doubly degenerate)  $\text{cm}^{-1}$ , respectively. Surprisingly, the difference for the C–C stretching mode between the calculated (1165  $\text{cm}^{-1}$ ) and the experimental (1163  $\text{cm}^{-1}$ )<sup>103</sup> is accidentally as small as only 2  $\text{cm}^{-1}$ , even though the values of the bond lengths differ by 5 pm. However, the gas phase calculation, which predicted similar bond length as current work, reported a frequency at 1220  $\text{cm}^{-1}$ , which is more than 50  $\text{cm}^{-1}$  higher than solid phase results.

Generally speaking, the frequency calculation in the solid phase in the current thesis matches better with the experimental result than the calculation in the gas phase.<sup>102</sup> This is not surprising because the spectra also measured in the solid phase.<sup>103</sup> Environment effects, which reflect the interactions between neighboring complexes, are totally missing in the gas phase calculation. For example, due to the lack of the neighboring complex, the C–C stretching mode in the gas phase could vibrate more freely than the same mode in the solid phase, which leads to the 50  $\text{cm}^{-1}$  higher calculated frequency for the gas phase results<sup>102</sup> than the one calculated in the solid phase. Compared with frequencies calculated for the solid phase, the gas phase results in most cases have large deviations from the experimental values obtained for the crystal than our results also calculated on a crystalline model.

$Os_2(CO)_6(CH_2CH_2)$ . The  $CH_2CH_2$  group is adsorbed over two Os atoms in  $\mu-\eta^2$  fashion which is the same as di- $\sigma$  ethylene adsorbed over Pt(111) (Fig. 3.8b). The optimized geometry is again quite similar to XRD result,<sup>37</sup> with a maximum deviation of 5 pm. The calculated C–Os bond lengths are 224–225 pm and the Os–Os bond length is 293 pm. Both values are slightly longer than the experimental values<sup>37</sup> by 2–5 pm. However, the predicted C–C distance, 151 pm, is 2 pm shorter than the XRD value.<sup>37</sup> A similar shorter C–C bond length was also obtained in the case of  $Co_3(CO)_9(CCH_3)$  (see above).

The discussion of the frequencies is again restricted to the modes of the hydrocarbon, leaving aside the C–H stretching modes. The C–C stretching mode is calculated at  $1010\text{ cm}^{-1}$ . This value is  $29\text{ cm}^{-1}$  higher than the experimental value,<sup>104</sup>  $981\text{ cm}^{-1}$ ; this is also the largest difference of all the compared modes between calculation and experiment. The predicted higher frequency reflects a stronger C–C bond interaction, consistent with the shorter C–C bond length in the DFT result. The frequencies of the other modes agree much better between calculation and experiment, within at most  $11\text{ cm}^{-1}$ . The calculated peaks at  $1456\text{ cm}^{-1}$  and  $1442\text{ cm}^{-1}$  are  $CH_2$  scissoring modes and they are reported at  $1445\text{ cm}^{-1}$  and  $1434\text{ cm}^{-1}$  by experiment.<sup>104</sup>  $CH_2$  rocking modes are calculated at  $1230\text{ cm}^{-1}$  and  $1015\text{ cm}^{-1}$ , only  $3\text{--}5\text{ cm}^{-1}$  higher than experiment.<sup>104</sup> The findings for the  $CH_2$  rocking modes are similar: calculated at  $841\text{ cm}^{-1}$  and  $758\text{ cm}^{-1}$  and measured at  $837\text{ cm}^{-1}$  and  $754\text{ cm}^{-1}$ .<sup>104</sup> In contrast, the calculated frequencies of the  $CH_2$  wagging modes,  $1135\text{ cm}^{-1}$  and  $1079\text{ cm}^{-1}$ , are slightly lower than the experimental values, by  $4\text{--}9\text{ cm}^{-1}$ .<sup>104</sup>

$Os_3(CO)_{10}(\mu-H)(CHCH_2)$ . Unlike the above two complex, vinyl is adsorbed at a bridge site with three C–Os bonds on the  $Os_3$  triangle via  $\mu-\eta^2$  fashion (Fig. 3.8), which differs from the adsorption complex of  $CHCH_2$  over Pt(111), which adsorbs in  $\mu_3-\eta^2$  fashion (see Fig. 3.2). The calculated C–Os bonds lengths are 212, 227 and 236 pm, nearly the same as the XRD result, 211, 227 and 236 pm.<sup>38</sup> The C–C bond length is calculated at 139 pm and the Os–Os bond lengths are determined at 287 pm. All of them are again quite close (within 5 pm) to the experiment results.<sup>38</sup>

In most cases, the differences between calculated and experimental frequencies<sup>105,106</sup> for the non-CH stretching modes of  $Os_3(CO)_{10}(\mu-H)(CHCH_2)$  are less than  $10\text{ cm}^{-1}$ . One exception is a mode where  $CH_2$  twisting and CH out-of-plane bending are mixed; its frequency is calculated at  $802\text{ cm}^{-1}$ , i.e.,  $16\text{--}20\text{ cm}^{-1}$  higher than the experiment results.<sup>105,106</sup>

Other modes are as follows: mixtures of two modes of CH<sub>2</sub> scissoring and C–C stretching at 1481 cm<sup>-1</sup> and 1311 cm<sup>-1</sup>; a mixture of CH<sub>2</sub> rocking and CH in-plane bending at 1258 cm<sup>-1</sup>; mixtures of CH<sub>2</sub> wagging and CH out-of-plane bending at 1009 cm<sup>-1</sup> and 997 cm<sup>-1</sup>; a mixture of CH<sub>2</sub> twisting and CH out-of-plane bending at 993 cm<sup>-1</sup>.

**Summary of the comparison for organometallic clusters.** Three organometallic clusters were selected for comparison. The structures predicted by DFT calculations match very well with experimental bond lengths (within 5 pm) measured by XRD. For the vibrational normal mode analysis, the current calculations focused on the hydrocarbon part of the spectrum, and compared calculated values and experimental results for the non-CH stretching modes. The differences of the non-CH stretching modes between calculated and experimental results are mostly less than 11 cm<sup>-1</sup>, with few exceptions with deviations up to 30 cm<sup>-1</sup>. Note that the GGA functional used is not able to describe dispersion interactions between the organometallic clusters in the crystal in a quantitative way.<sup>107</sup> Nevertheless, it is fair to say the periodic DFT calculations could well reproduce the experimental results for the organometallic compounds.

### 3.4.3 Comparison between C<sub>2</sub>H<sub>x</sub> moieties (x = 3–4) on the surface and in a complex

**Perfect match: ethylidyne.** As early as the end of 1970s, ethylidyne was successfully identified on Pt(111) by comparison with organometallic clusters. Kesmodel et al.<sup>79</sup> reported their LEED and HREELS studies of the thermal evolution of ethylene pre-adsorbed on Pt(111). The result clearly showed the similarity on the structures and the vibrational frequencies between surface ethylidyne and the corresponding moiety of Co<sub>3</sub>(CO)<sub>9</sub>(CCH<sub>3</sub>). Both of them have the same adsorption mode on the metal substrate: at a three-fold hollow site in μ<sub>3</sub> fashion. Similar adsorption modes lead to similar values for the vibrational frequencies. In most cases, the vibrational frequency for the analogous mode on different substrates differs by less than 30 cm<sup>-1</sup>, except for the C–C stretching mode. This mode is calculated at 1165 cm<sup>-1</sup> in Co<sub>3</sub>(CO)<sub>9</sub>(CCH<sub>3</sub>), which is about 60 cm<sup>-1</sup> higher than the same mode over Pt(111), 1095–1107 cm<sup>-1</sup>. Such observation is consistent with the corresponding experimental results: 1163 cm<sup>-1</sup> in Co<sub>3</sub>(CO)<sub>9</sub>(CCH<sub>3</sub>)<sup>103</sup> and 1115–1130 cm<sup>-1</sup> on Pt(111).<sup>9,63,95,99-101</sup> In the C–C stretching mode, the C atom which is directly connected to the metal substrate has a large displacement. Concomitantly, the C–M bond is stretched due to the

movement of this C atom. Experiments reported<sup>102</sup> that the frequency of the C–M stretching modes differ by up to  $50\text{ cm}^{-1}$  when ethynidyne adsorbed on different substrates, indicating different C–M bond strength on different substrates. Thus, on different substrate, the C–C stretching mode suffers larger differences of the stretching or bending for the C–M bonds compared to the modes that involve only vibrations of the hydrocarbon part.

**Reasonable match: ethylene.** In  $\text{Os}_2(\text{CO})_6(\text{CH}_2\text{CH}_2)$ , ethylene interacts with two Os atoms in  $\mu_2$  fashion, which is the same as di- $\sigma$  adsorbed ethylene over Pt(111). The geometries of ethylene on these two substrates are slightly different. The C–C bond in ethylene is parallel to one surface metal–metal bond over Pt(111) while this is not the case in the organometallic cluster, with the dihedral angle between Os–Os and C–C being  $23^\circ$ . This disparity between the two geometries does not strongly affect the bond lengths, but leads to changes in bond angles, e.g., H–C–M or C–C–M differ by up to  $5^\circ$ . Thus, the four CH stretching modes, which mainly alter the bond length, exhibit similar frequencies that differ less than  $32\text{ cm}^{-1}$  on the two substrates. However, other bending modes, vibrations along bond angles, differ a lot between adsorption complexes and cluster compounds. For example, the  $\text{CH}_2$  twisting modes are calculated at  $841\text{ cm}^{-1}$  and  $758\text{ cm}^{-1}$  and measured at  $837\text{ cm}^{-1}$  and  $754\text{ cm}^{-1}$  in  $\text{Os}_2(\text{CO})_6(\text{CH}_2\text{CH}_2)$ <sup>104</sup>, which is about  $60\text{--}140\text{ cm}^{-1}$  higher than the same modes over Pt(111). One possible explanation for the blue shift of these two modes in the organometallic cluster is based on the slightly different geometries compared with the one on Pt(111). The twisting modes of  $\text{CH}_2\text{CH}_2$  alter the HCCH dihedral angle. On Pt(111) surface, the HCCH dihedral angle is about  $0^\circ$ . However, it is  $32^\circ$  in the  $\text{Os}_2(\text{CO})_6(\text{CH}_2\text{CH}_2)$ . One may expect the potential energy surface along the HCCH dihedral angle to be flatter for the former case, because when one changes this angle, the two H atoms move away from each other. But in the latter case, they will be closer to each other when the dihedral angle changes in the direction from  $32^\circ$  to  $0^\circ$ . Similar large shifts are observed for the  $\text{CH}_2$  wagging modes. Generally speaking, the frequency shifts for similar modes of ethylene on different substrates can be as large as  $140\text{ cm}^{-1}$  i.e.  $\text{CH}_2$  twisting. Recall the case of ethynidyne, where similar geometries of ethynidyne in the organometallic cluster and on the surface imply comparable frequencies, with a maximum deviation of  $70\text{ cm}^{-1}$ .

**Mismatch: vinyl.** Vinyl adsorbs over a three-fold site on Pt(111) via  $\mu_3\text{-}\eta^2$  fashion, which is totally different from its bonding mode in the cluster compound  $\text{Os}_3(\text{CO})_{10}(\mu\text{-H})(\text{CHCH}_2)$ . The different adsorption modes lead to large difference in the geometries of

vinyl on these two kinds of substrates. For example, the C–C bond length in  $\text{Os}_3(\text{CO})_{10}(\mu\text{-H})(\text{CHCH}_2)$  is only 139 pm, 8 pm shorter than the same bond over Pt(111). The shorter C–C bond length, with stronger C–C interaction, in the organometallic cluster results in a frequency of C–C stretching mode as high as  $1311\text{ cm}^{-1}$ . The analogous mode for vinyl over Pt(111) is not only  $200\text{ cm}^{-1}$  lower than it in the organometallic cluster, but it also mixes with CH bending and  $\text{CH}_2$  wagging modes. The bond angle H–C–H in the  $\text{CH}_2$  group differs by  $4^\circ$  on two substrates, which leads to a shift of the  $\text{CH}_2$  scissoring mode by  $100\text{ cm}^{-1}$  on the two kinds of substrates. Therefore, different adsorption modes change details of the geometry of vinyl over the two kinds of substrates, which in turn cause a large shift for the vibrational frequencies. Thus, it prevents a direct comparison on both substrates.

### 3.4.4 Final remark on a spectroscopically identified transient intermediate

Previous spectroscopic studies<sup>62,63</sup> suggested that the intermediate during the conversion of ethylene to ethylidyne is ethylidene, as confirmed by two vibrational frequencies at  $2957\text{--}2960\text{ cm}^{-1}$  for the  $\text{CH}_3$  asymmetric stretching and  $1387\text{ cm}^{-1}$  for the symmetric bending of  $\text{CH}_3$ . In the meantime, several other experiments seemed to rule out other intermediates, like vinyl or vinylidene. However, the DFT calculations in this thesis suggest that ethylidene can easily convert to ethylidyne, with a low barrier around  $19\text{--}29\text{ kJ mol}^{-1}$ . This barrier is much lower than typical hydrogenation / dehydrogenation barriers, normally around  $50\text{--}100\text{ kJ mol}^{-1}$ . In other words, detection of this intermediate is highly unlikely because of its expected short life-time.<sup>108,109</sup> This is confirmed by recent kMC simulations,<sup>92</sup> which showed that vinylidene, but not ethylidene could be accumulated over Pt(111). In this section, the discussion will be focused on the vibrational frequencies of the possible intermediates.

**Spectra of vinyl halide:** Vinyl was ruled out on the basis of their recorded low-temperature vibrational spectrum of vinyl iodide.<sup>62</sup> Three peaks, at  $2995\text{ cm}^{-1}$ ,  $3033\text{ cm}^{-1}$ , and  $3068\text{ cm}^{-1}$  at 132 K, were observed and all of them are too high to account for the feature at  $2960\text{ cm}^{-1}$  in the conversion of ethylene to ethylidyne. However, one should also not ignore the possibility for the changing of adsorption site for vinyl iodide at low temperatures. Similar experiments done by Zaera et al.<sup>68</sup> and Liu et al.<sup>110</sup> working on the system  $\text{CH}_2\text{CHBr}$  covered a wider spectral range of frequencies. Besides C–H stretching mode at  $3059\text{--}3070\text{ cm}^{-1}$ , the C–C stretching mode is observed at  $1565\text{--}1584\text{ cm}^{-1}$ , clearly showing the character of a C=C double bond. In such cases, vinyl adsorbed at a top site in  $\eta^1$  fashion, preserving C=C, and the

**Table 3.8** Calculated vibrational frequencies<sup>a</sup> of relevant C<sub>2</sub>H<sub>x</sub> intermediates (x = 2–4) on Pt(111) for two coverages  $\theta$  and assignment<sup>b</sup> of the normal modes

$\mu$ -Ethyliidene			$\eta$ -Vinyl			$\eta^2\mu_3$ -Vinylidene		
$\theta = 1/3$	$\theta = 1/9$	Assignment	$\theta = 1/3$	$\theta = 1/9$	Assignment	$\theta = 1/3$	$\theta = 1/9$	Assignment
2985	2989	CH <sub>3</sub> v <sub>a</sub>	3114	3113	CH <sub>2</sub> v <sub>a</sub>	3124	3133	CH <sub>2</sub> v <sub>a</sub>
3038 <sup>c</sup>	2966	CH <sub>3</sub> v <sub>a</sub> /CH v	3049	3058 <sup>c</sup>	CH v/CH <sub>2</sub> v <sub>s</sub>	3033	3043	CH <sub>2</sub> v <sub>s</sub>
2990 <sup>c</sup>	2945	CH v/CH <sub>3</sub> v <sub>a</sub>	3028	3029 <sup>c</sup>	CH <sub>2</sub> v <sub>s</sub> /CH v			
2927	2880	CH <sub>3</sub> v <sub>s</sub>						
			1547 <sup>c</sup>	1537	CC v/CH <sub>2</sub> $\delta$			
1406	1402	CH <sub>3</sub> $\delta_a$	1354 <sup>c</sup>	1352	CH <sub>2</sub> $\delta$ /CC v	1415	1413	CH <sub>2</sub> $\delta$
1404	1391	CH <sub>3</sub> $\delta_a$	1206	1192	CH <sub>2</sub> $\rho$ /CH $\delta_{ip}$	1263	1256	CC v
1328	1336	CH <sub>3</sub> $\delta_s$	948	941	CH <sub>2</sub> $\rho$ /CH $\delta_{ip}$	980	973	CH <sub>2</sub> $\rho$
1244	1226	CH $\delta_{ip}$ /CH <sub>3</sub> $\rho_s$						
1049	1040	CC v						

<sup>a</sup> Only normal modes with calculated frequencies above  $\sim 950$  cm<sup>-1</sup> are shown. <sup>b</sup> Notations used: v, stretching;  $\delta$ , bending;  $\tau$ , twisting;  $\omega$ , wagging;  $\rho$ , rocking; a, asymmetric; s, symmetric; ip, in-plane.

<sup>c</sup> The admixture of the second mode is very weak.

calculated C=C stretching mode of  $\eta$ -vinyl located at 1537–1547 cm<sup>-1</sup> (Table 3.8), very close to the experimentally observed frequencies 1565–1584 cm<sup>-1</sup>. On the other hand, the calculated highest non-CH stretching frequency for  $\mu_3$ - $\eta^2$ -vinyl is only around 1380 cm<sup>-1</sup>, and the C–C stretching mode  $\nu$ (CC), coupled both with CH<sub>2</sub> wagging  $\omega$ (CH<sub>2</sub>) and CH in-plane bending modes  $\delta_{ip}$ (CH) or coupled only with  $\delta_{ip}$ (CH), are located at even lower frequencies, at 1060 cm<sup>-1</sup> and 1099 cm<sup>-1</sup>, respectively.  $\eta$ -vinyl is calculated 58 kJ mol<sup>-1</sup> and 75 kJ mol<sup>-1</sup> less stable than  $\mu_3$ - $\eta^2$ -vinyl at 1/3 and 1/9 coverage, respectively. This species may convert to the more stable  $\mu_3$ - $\eta^2$ -vinyl after heating, and might generate the signal at 2960 cm<sup>-1</sup> at high temperature.

**Spectra of thermal evolution of acetylene:** Previous experiments provided more solid evidence to rule out vinylidene as the intermediate. Cremer et al.<sup>111</sup> reported a SFG study of thermal evolution of acetylene on Pt(111). Four peaks at 2981, 2924, 2878, 2837 cm<sup>-1</sup> at 125 K were observed which perfectly matched the reported corresponding organometallic analog<sup>106</sup> of vinylidene with peaks at 3047, 2986, 2926, 2898, and 2855 cm<sup>-1</sup>. The signal at

2960  $\text{cm}^{-1}$ , associated with ethylidene, appeared only at higher temperatures. A later RAIRS study of the same process by Deng et al.<sup>101</sup> did not observe all these features at low temperature (85K). But at higher temperatures, both experiments observed similar multiple peaks: 2982, 2993, and 3001  $\text{cm}^{-1}$ , by SFG at 210K<sup>111</sup> and 2976 and 2990  $\text{cm}^{-1}$ , by RAIRS at 191K.<sup>101</sup> The one at 2976–2982 is still assigned to  $\mu_3\text{-}\eta^2$ -vinylidene. The newly appeared feature at 2990–2993 is believed to be the  $\mu_3\text{-}\eta^2$  adsorbed vinyl. A later study,<sup>101</sup> which covered a wider range, also reported another intense peak at 1280  $\text{cm}^{-1}$  and assigned it to the C–C stretching of  $\mu_3\text{-}\eta^2$ -vinyl. Multiple evidence supports this assignment including isotope experiments,<sup>101</sup> HREELS of vinyl iodide,<sup>110</sup> HREELS of the photo-decomposition of 1,1,2-trichloroethane,<sup>112</sup> and spectrum of organometallic analog  $\text{Os}_3(\text{CO})_{10}(\mu\text{-H})(\text{CHCH}_2)$ .<sup>106</sup> Further heating of the system is similar to the thermal evolution of ethylene over Pt(111), which generate a similar intermediate with peaks at 2964  $\text{cm}^{-1}$  and 1391  $\text{cm}^{-1}$ .<sup>101</sup>

However, the current calculations clearly show that neither  $\mu_3\text{-}\eta^2$ -vinyl nor  $\eta$ -vinyl has a vibration mode around 1280  $\text{cm}^{-1}$  over Pt(111). According to the comparison in Section 3.4.1, the maximum deviation is about 50  $\text{cm}^{-1}$  between experimental and calculated surface frequency results (Table 3.5 and 3.6). In most cases, the deviation is even less than 30  $\text{cm}^{-1}$ , which clearly rules out vinyl to be responsible for the peak at 1280  $\text{cm}^{-1}$ . It might be vinylidene or other C2 species, which is not covered by current calculation, e.g. CHCH or CCH, responsible for the 1280  $\text{cm}^{-1}$  signal.

Actually, the surface C2 species contain similar structures and functional groups which lead to the vibrational modes are very close to each other. It is really hard to identify these intermediates only by spectroscopy without any further (spectroscopic) information. Nevertheless, both experimental studies<sup>101,111</sup> seem to reach agreement that during the thermal evolution of acetylene, two intermediates are identified: at low temperature ( $\sim 200$  K) by the series of peaks at 2800–3000  $\text{cm}^{-1}$  and 1280  $\text{cm}^{-1}$ ; and at high temperature ( $\sim 300$  K) by the peaks at  $\sim 1387$   $\text{cm}^{-1}$  and  $\sim 2960$   $\text{cm}^{-1}$ , which is the same intermediate as the one found in the conversion of ethylene to ethylidyne. Due to the lack of the necessary activation barrier for the conversion of acetylene, one may suggest that the intermediate at  $\sim 200$  K should not be vinyl based on the calculated results in this thesis.

***Spectra of thermal evolution of ethylene:*** Previous experiments observed two vibrational modes during the conversion of ethylene to ethylidyne, and assign these

**Table 3.9** Calculated vibrational frequencies<sup>a</sup> of relevant C<sub>2</sub>H<sub>x</sub> intermediates (x = 2–4) on Pt(111) for two coverages  $\theta$  and assignment<sup>b</sup> of the normal modes

$\mu$ -Ethylidene			$\eta^2\mu_3$ -Vinyl			$\eta^2\mu_3$ -Vinylidene		
$\theta = 1/3$	$\theta = 1/9$	Assignment	$\theta = 1/3$	$\theta = 1/9$	Assignment	$\theta = 1/3$	$\theta = 1/9$	Assignment
before scaling								
2985	2989	CH <sub>3</sub> v <sub>a</sub>	3114	3113	CH <sub>2</sub> v <sub>a</sub>	3124	3133	CH <sub>2</sub> v <sub>a</sub>
3038 <sup>c</sup>	2966	CH <sub>3</sub> v <sub>a</sub> /CH v	3049	3058 <sup>c</sup>	CH v/CH <sub>2</sub> v <sub>s</sub>	3033	3043	CH <sub>2</sub> v <sub>s</sub>
2990 <sup>c</sup>	2945	CH v/CH <sub>3</sub> v <sub>a</sub>	3028	3029 <sup>c</sup>	CH <sub>2</sub> v <sub>s</sub> /CH v			
2927	2880	CH <sub>3</sub> v <sub>s</sub>						
after scaling <sup>d</sup>								
2913	2917	CH <sub>3</sub> v <sub>a</sub>	3039	3038	CH <sub>2</sub> v <sub>a</sub>	3049	3058	CH <sub>2</sub> v <sub>a</sub>
2965 <sup>c</sup>	2895	CH <sub>3</sub> v <sub>a</sub> /CH v	2976	2985 <sup>c</sup>	CH v/CH <sub>2</sub> v <sub>s</sub>	2960	2970	CH <sub>2</sub> v <sub>s</sub>
2918 <sup>c</sup>	2874	CH v/CH <sub>3</sub> v <sub>a</sub>	2955	2956 <sup>c</sup>	CH <sub>2</sub> v <sub>s</sub> /CH v			
2857	2811	CH <sub>3</sub> v <sub>s</sub>						

<sup>a</sup> Only normal modes with calculated frequencies above  $\sim 950$  cm<sup>-1</sup> are shown. <sup>b</sup> Notations used:  $\nu$ , stretching;  $\delta$ , bending;  $\tau$ , twisting;  $\omega$ , wagging;  $\rho$ , rocking; a, asymmetric; s, symmetric; ip, in-plane.

<sup>c</sup> The admixture of the second mode is very weak. <sup>d</sup> The uncertainty of all these mode are  $\sim \pm 35$  cm<sup>-1</sup>

frequencies to ethylidene, 2957–2960 cm<sup>-1</sup> to be CH<sub>3</sub> asymmetric stretching and 1387 cm<sup>-1</sup> to be symmetric bending of CH<sub>3</sub>. Indeed, the organometallic complex, Os<sub>2</sub>(CO)<sub>8</sub>(CHCH<sub>3</sub>),<sup>113</sup> shows similar adsorption modes at 2950 cm<sup>-1</sup> and 1369 cm<sup>-1</sup>. Besides the matching with the organometallic analog, there is also evidence from the surface decomposition of 1,1-diiodethane on the Pt(111).<sup>85</sup> The corresponding features are reported at 2972 cm<sup>-1</sup> and 1372 cm<sup>-1</sup>. Thus it seems that ethylidene has been proved to be the intermediate during ethylene conversion to ethylidyne by previous experiments.

However, the comparison between this intermediate and other C<sub>2</sub> species in organometallic clusters should be not ignored. For example, Os<sub>3</sub>(CO)<sub>9</sub>( $\mu$ -H)<sub>2</sub>(CCH<sub>2</sub>), containing vinylidene, also has two suitable vibrational modes, a C–H stretching frequency at 2986 cm<sup>-1</sup> and the C–C stretching mode at 1331 cm<sup>-1</sup>, which are close to the spectrum of the

observed intermediate on Pt(111). Recall the discussion in Section 3.4.2, where it was discussed that a difference of  $50\text{ cm}^{-1}$  for the C–C stretching mode between the organometallic complex and the adsorption complex is still acceptable. Thus, if the comparison is only done between the spectra of surface species and the organometallic complexes, it is hard to judge whether ethylidene or vinylidene should be the intermediate.

The current calculations offer new evidence for the identification. The vibrational normal mode analysis clearly shows that not only ethylidene, but also vinyl and vinylidene exhibit a vibrational mode, the  $\text{CH}_2$  scissoring modes  $\delta(\text{CH}_2)$  at  $1380\text{ cm}^{-1}$  and  $1413\text{ cm}^{-1}$ , which are close to the experimental value  $1387\text{ cm}^{-1}$ . The other experimentally observed mode is C–H stretching at  $\sim 2960\text{ cm}^{-1}$ . The calculated harmonic frequencies are too high to be directly compared with experiment in view of the strong anharmonicity effect of this kind of modes. A simple way to improve such a comparison is via a scaling factor, obtained by comparing suitable calculated and experimental values. The results of this thesis give rise to a factor of  $0.976\pm 0.012$  by the values in Table 3.5 and 3.6; this is very close to the value, 0.973, used in a previous study of propylene and propylidyne over Pt(111).<sup>114</sup> The scaled values for the C–H stretching modes are summarized in Table 3.9. After scaling, the symmetric  $\text{CH}_2$  stretching mode of vinyl and vinylidene, at  $2956\text{ cm}^{-1}$  and  $2970\text{ cm}^{-1}$ , respectively, is very close to the value at  $2960\text{ cm}^{-1}$  reported by experiment. However, the symmetric stretching of  $\text{CH}_3$  in ethylidene is too low to be assigned to the experimentally observed one, especially in the low coverage (1/9) case which is more close to the true coverage for an intermediate during ethylene conversion. Recall that the calculated activation energy for the conversion from ethylidene to ethylidyne is as low as  $19\text{--}29\text{ kJ mol}^{-1}$ , indicating a fast conversion of ethylidene. Thus it should not accumulate on the surface. Instead, either vinyl or vinylidene may be observed as they need to overcome activation barriers of  $\sim 80\text{ kJ mol}^{-1}$  in the conversion to ethylidyne. Indeed, results of kMC simulations<sup>115</sup> indicate that vinylidene could be accumulated on the surface during the conversion of ethylene to ethylidyne.

### 3.5. Summary

In this chapter, the mechanism of ethylene conversion to ethylidyne over Pt(111) was studied with periodic slab model density function calculations. Three possible reaction pathways were examined at three different coverages, 1/3, 1/4 and 1/9: *i*) via vinyl and ethylidene (M1), *ii*) via vinyl and vinylidene (M2), and *iii*) via ethyl and ethylidene (M3). The calculated barriers

for the hydrogenation / dehydrogenations reactions involved on Pt(111) are in the range 19–92 kJ mol<sup>-1</sup>. However, higher barriers, above 150 kJ mol<sup>-1</sup>, were obtained for the 1,2–H shift reactions. The latter result directly disproved the previous proposed two-step mechanism<sup>71</sup> with 1,2–H shift reactions involved.

According to the calculated barriers for the reaction steps in this conversion, the mechanisms M1 and M2 are likely at work over Pt(111) in the absence of coadsorbed hydrogen. Both of them share the same first step, ethylene dehydrogenation to vinyl. Then vinyl could be either hydrogenated to ethylidene and dehydrogenated to ethylidyne (M1) or dehydrogenated to vinylidene and rehydrogenated to ethylidyne. According to the calculated barrier heights, the shared dehydrogenation step is rate limiting at high coverage, with a barrier of 92 kJ mol<sup>-1</sup>. At low coverage, the order of the barrier heights differs, with a rate-limiting barrier at ~80 kJ mol<sup>-1</sup> for the hydrogenation step of vinyl to ethylidene in M1 and for the dehydrogenation step of vinyl to vinylidene in M2. In this case, the first step of this conversion no longer rate-limiting, indicating the possibility of accumulating an intermediate on the surface. Indeed, in previous experiments two IR signals were noted and assigned to ethylidene as intermediate.<sup>62,63</sup> However, the current calculations suggest that this intermediate could be vinylidene based on three evidences: i) the barrier for the conversion of ethylidene to ethylidyne is calculated too low (19–29 kJ mol<sup>-1</sup>), indicating a short life time of ethylidene on the surface; ii) the vibrational normal mode analysis suggests vinylidene also to have a vibration mode with a frequency close to the experimentally observed value; iii) kinetic Monte Carlo simulation observed an accumulation of vinylidene during the conversion of ethylene to ethylidyne.

When additional hydrogen is available in the system, M3 starts to be dominant due the relatively low hydrogenation barrier from ethylene to ethyl, especially in the case with  $\pi$ -ethylene on Pt(111). However, the second step of M3, dehydrogenation of ethyl to ethylidene, strongly competes with the formation of ethane. At low coverage (1/9), the barriers for these two steps are comparable. However, at high coverage (1/3), the activation energy of the hydrogenation of ethyl is 21 kJ mol<sup>-1</sup> lower than the dehydrogenation of ethyl. Furthermore, once ethane is produced, it should easily desorb, leaving the surface irreversibly.

## Chapter 4

# Methylcyclopentane ring-opening reactions

### 4.1. Introduction

#### 4.1.1 Experimental research

Generally speaking, a catalyst required for selective (hydrogenolytic) ring-opening (SRO) of naphthenes is bifunctional:<sup>116</sup> i) hydrogenation or dehydrogenation reactions are efficiently catalyzed by highly dispersed noble metal particles, e.g. Pt, Pd, Ir, Ru, or Rh; ii) cracking or isomerization is catalyzed by an acidic support. Previous experiments<sup>116-120</sup> showed that the ring-opening (RO) reactions on these metals were much easier for five-member hydrocarbon rings than for six-member rings. Thus, an acidic support, which promotes the contraction of a six-member ring to a five-member ring, facilitates and accelerates the overall hydrogenolysis process.<sup>121, 122</sup> The generated five-member ring products can move to an active site on the metal component and then undergo a RO reaction.

In order to achieve a significantly improved CN number, the ideal products of the SRO reactions are those that preserve the original molecular weight with a minimum degree of branching. The selectivity of the SRO products depends on the nature of the metal catalyst. For example, the RO of methylcyclopentane (MCP), which is widely investigated as a model system,<sup>18-22</sup> yields three products: 2-methylpentane (2MP), 3-methylpentane (3MP), and *n*-hexane (*n*Hx). The branched products, 2MP and 3MP, are always favored when the reaction is catalyzed by supported Ir or Rh particles. However, the selectivity on other supported metal catalysts, like Pt, strongly depends on the dispersion of the metal. Large Pt particles<sup>123</sup> (e.g. of ~10 nm<sup>124</sup>) or flat Pt surfaces (111) and (100)<sup>125, 126</sup> tend to produce preferentially 2MP and 3MP, whereas small Pt particles<sup>124,127</sup> statistically break C–C bonds in the five-member ring. Other studies on bimetallic catalysts, e.g. AuPt,<sup>128</sup> GePt,<sup>129</sup> RhPt,<sup>19,130</sup> and RhGe,<sup>131</sup> also did not show a promising selectivity toward *n*Hx.

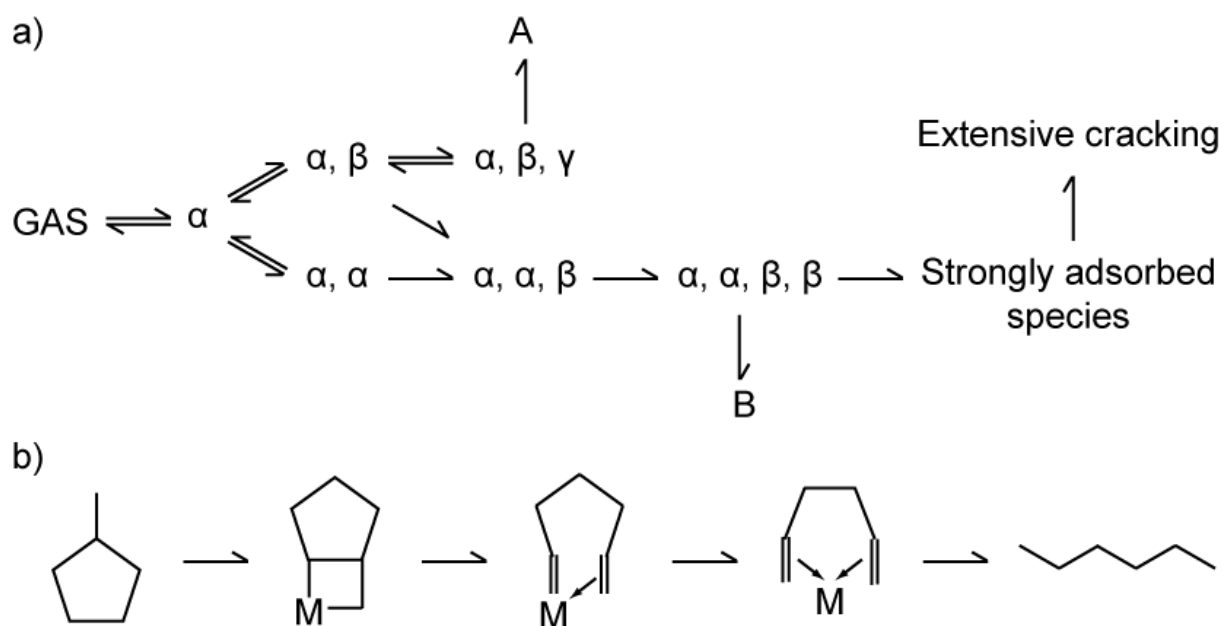


**Figure 4.1** Dissociative mechanism proposed by Gault et al. (a-A) non-selective;<sup>123</sup> (a-B) selective;<sup>123</sup> (b) one of the possible partially selective mechanisms.<sup>117</sup>

Due to the complexity of the involved chemistry, the mechanism of SRO has not clearly been proved experimentally and thus far remained at a hypothetical level. Several mechanisms were proposed in the literature on the basis of the experimental observations on Pt based catalysts. Generally, these mechanisms could be divided into two classes:<sup>132</sup> “dissociative”, where a dehydrogenation of the surface intermediate takes place before the ring opening and “associative” where the ring opening immediately follows the adsorption. Also, “edgewise” or “flat-lying” intermediates were discussed for both these groups. Two mechanisms have been most often invoked in various MCP RO studies: via a dissociative path and edgewise adsorption (the so-called “di-carbene” mechanism originally proposed by Gault, Maire, and associates<sup>117,123, 133</sup>) and an associative mechanism via a flat-lying intermediate (the “multiplet” mechanism introduced by Bragin and Liberman<sup>134</sup>),

In the dissociative mechanism, a hydrocarbon needs to be dehydrogenated to form an “edgewise” geometry before the C–C bond breaking. As early as 1965, Gault et al.<sup>123</sup> attempted to rationalize available experimental data for MCP RO on Pt by suggesting several reaction routes (Fig. 4.1a). There, types A and B denote completely non-selective and completely selective mechanisms, respectively. In a non-selective type A mechanism, all cyclic bonds are broken with the same probability resulting in the statistical 2MP : 3MP :  $n$ Hx

distribution of 2 : 1 : 2. Such a non-selective ring cleavage can happen after a loss of one to three H atoms ( $\alpha$ ,  $\alpha\alpha$ ,  $\alpha\beta$ ,  $\alpha\beta\gamma$ ); however, di-adsorbed intermediates were tentatively favored in the original papers by Gault and his school.<sup>117,123,133</sup> In a selective type B mechanism, only di-secondary CH<sub>2</sub>–CH<sub>2</sub> bonds are cleaved (i.e. at unsubstituted positions) after a loss of four H atoms and a formation of the  $\alpha\alpha\beta\beta$ -tetra-adsorbed intermediate. Due to the methyl substituent, a secondary-tertiary CH<sub>2</sub>–CHMe bond cannot be cleaved via this mechanism. In this case, a dehydrogenated MCP only forms an  $\alpha\alpha\beta$ -tri-adsorbed intermediate and its hydrogenolysis is expected to be unlikely. In some cases, the ring opening does not follow the “selective” or “non-selective” mechanism, instead producing an unusually high amount of 3MP or *n*Hx relative to its statistical ratio, e.g. *n*Hx is formed via a mechanism proposed by Gault<sup>117</sup> (Fig. 4.1b). The dissociative mechanism, involving dehydrogenative chemisorption prior to C–C bond breaking, was indirectly supported by studies of propane hydrocracking, where the adsorbed intermediate was shown to lose 3.5–5 hydrogen atoms on nickel and of 2–4 hydrogen atoms on platinum per molecule of propane.<sup>135</sup>

In the associative mechanism, a hydrocarbon ring is physically adsorbed over the metal catalyst in flat-lying fashion. The ring opens through the attack of an extra H atom co-adsorbed on the surface. This mechanism was preferred by the Russian and the Hungarian schools.<sup>132,134,136</sup> Among the facts speaking in favor of an associative mechanism is for instance an observation on a Pt catalyst<sup>136</sup> that the ring-opening of *cis*-1,2-dimethylpentane (*cis*-1,2-DMCP) is faster than that of *trans*-1,2-DMCP. Due to favorable stereochemistry, *cis*-1,2-DMCP can be adsorbed more strongly in the flat-lying fashion than the *trans* isomer; hence, the net conversion rate should be faster for the former. However, this argument does not seem to overrule a possibility of a dissociative mechanism because a dehydrogenation barrier to form an  $\alpha\alpha\beta\beta$ -tetra-adsorbed intermediate could also increase due to steric hindrance in the case of *trans*-1,2-DMCP.

Several other mechanisms were proposed in the studies of MCP RO on other metals of the Pt group. For example, on Pd based catalysts, the ratio of three RO products, 2MP : 3MP : *n*Hx, was close to 2 : 1 : 1.<sup>137</sup> To rationalize this observation, Le Normand et al.<sup>137</sup> suggested that the reaction on Pd proceeds through the formation of  $\pi$ -olefin- $\sigma$ -alkyl 1,2-5 intermediate. With the additional assumption that MCP is only adsorbed via a secondary carbon atom of the ring, the expected statistical distribution of this mechanism is 2MP : 3MP : *n*Hx = 2 : 1 : 1, which is close to the experimental observation.

### 4.1.2 Former theoretical studies

Several theoretical studies attempted to explore the chemistry of MCP or its derivatives on metal surfaces, but most of them only addressed the adsorption properties of various five-member rings, e.g. MCP,<sup>138</sup> cyclopentane<sup>139-141</sup> and cyclopentene.<sup>140,142</sup> Another early study by Brizuela et al.<sup>143</sup> addressed the dehydrogenation reactions of cyclopentene at a semiempirical level, but did not touch the ring-opening.

### 4.1.3 Reaction network investigated in the current study

As stated above, earlier theoretical studies on the MCP ring-opening system were limited to the adsorption properties of five-member rings. However, some other theoretical studies on related hydrocarbon systems offered indirect evidence which supported the dissociative mechanism. For example, DFT calculations<sup>144,145</sup> showed that the barriers for C–C bond cleavage of C<sub>2</sub> or C<sub>3</sub> species on M(111) (M = Pd, Pt) decreased with increasing degree of dehydrogenation of the hydrocarbon. These observations support the four-fold dehydrogenated  $\alpha\alpha\beta\beta$ -tetra-adsorbed intermediate to be the precursor of the C–C bond breaking step. Another theoretical study<sup>146</sup> in the context of olefin metathesis catalyzed by transition metal complexes provided a prototype of the partially selective dissociative mechanism via a  $\alpha\gamma$ -adsorbed metallocyclobutane intermediate (Fig. 4.1b)

When checking on the possibility of an associative mechanism, I expected that the barrier of the C–C bond breaking step in an associative mechanism should be rather high because the precursor of the C–C bond breaking step is a saturated hydrocarbon interacting only very weakly with the metal catalyst. Indeed, test calculations with scanning of the potential energy surface according to such an associative mechanism did not directly locate the transition state of the C–C bond breaking step, but the approximate barrier of this reaction was estimated to be 150 kJ mol<sup>-1</sup> or higher. Hence, in this thesis, the calculations were mainly based on the assumption of a dissociative mechanism.

Fig. 4.2 shows the reaction network investigated in this study. The proposed mechanism contains three global steps: (i) MCP is dehydrogenated to form an  $\alpha\alpha\beta\beta$ -tetra-adsorbed,  $\alpha\alpha\beta$ -tri-adsorbed or  $\alpha\gamma$ -di-adsorbed intermediate, the precursors of the C–C bond breaking step; (ii) one of the endocyclic C–C bond is cleaved; (iii) the adsorbate is completely hydrogenated and subsequently desorbed from the surface.

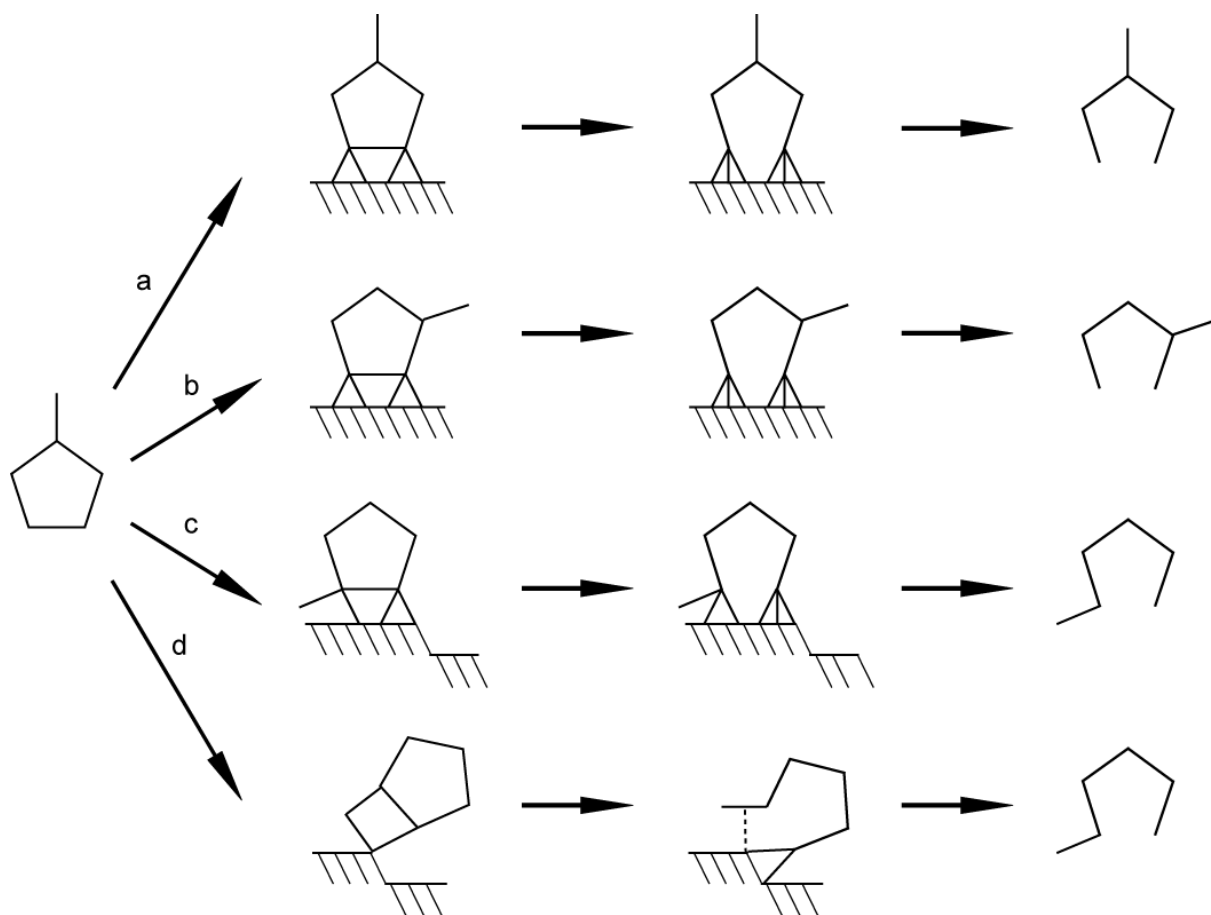


**Figure 4.2** The mechanism calculated in this thesis: formation of (a) 3MP and (b) 2MP via an  $\alpha\alpha\beta\beta$ -tetra-adsorbed intermediate; formation of  $n\text{Hx}$  via (c)  $\alpha\alpha\beta$ -tri-adsorbed or (d)  $\alpha\gamma$ -di-adsorbed intermediate

## 4.2. Ring-opening reactions catalyzed by Pt

In this part, the calculation was focused on Pt based catalysts. As stated in the introduction, the selectivity of the RO products strongly depends on the Pt particle size.<sup>124</sup> In order to model the particle size effect on the product distribution, two types of metal surfaces, flat Pt(111) and stepped Pt(211) and Pt(322), were selected to model terrace-rich large particles and defect-rich small particles, respectively. I will first comment on the calculated activation energies of the elementary steps on these two types of surfaces and then I will discuss the particle size effect on the basis the results of my calculations.

### 4.2.1 Reactions on large Pt particles

The RO reactions of MCP on Pt(111), or large Pt particles, selectively produce

branched 2MP and 3MP. According to the dissociative mechanism assumed in this study involving deep dehydrogenation, MCP needs to convert to an  $\alpha\alpha\beta\beta$ -tetra-adsorbed cyclic intermediate to form branched 2MP or 3MP. On the other hand, on the reaction pathway to the linear product  $n\text{Hx}$ , MCP can lose at most three H atoms forming an  $\alpha\alpha\beta$ -tri-adsorbed intermediate due to the presence of the methyl substituent, and it is supposed to require a high activation energy for the subsequent C–C cleavage step. As shown in Fig. 4.2, the conversion of MCP to 2MP, 3MP, and  $n\text{Hx}$  involves a series of dehydrogenation steps, C–C bond breaking step and hydrogenation steps, which will be discussed in detail in the following. For convenience, the C atoms within the ring will be named as follows: the first C atom which binds to the metal surface is denoted as C1, and the second as C2; the other three carbon centers are numbered from C3 to C5 along the direction from C1 to C2.

***Dehydrogenation reactions over Pt(111).*** Several dehydrogenation steps are required to form  $\alpha\alpha\beta\beta$ -tetra-adsorbed or  $\alpha\alpha\beta$ -tri-adsorbed intermediates in the conversion from MCP to 2MP/3MP, or  $n\text{Hx}$ , respectively. Fig. 4.3 shows the structures of the four dehydrogenation steps on the reaction pathway to 3MP. The intermediates and TS structures involved in the corresponding dehydrogenation steps on the way to 2MP and  $n\text{Hx}$  are not shown since they are quite similar to the above structures, only the position of the methyl group is changed. In general, all the dehydrogenation steps pass through a transition state with a typical C–H–Pt three-member-ring structure as discussed in Chapter 3. After each dehydrogenation step, the released H atom is assumed to move freely far away from the adsorbate. Thus, there is at most one co-adsorbed H atom in each final state modeled. The diffusion steps of an H atom are not explicitly considered in this thesis due to their low activation energy.<sup>147</sup> For all the dehydrogenation reactions, the geometry of an adsorbate in the final state is nearly the same as in the initial state of the next step, the only principle difference being that in the final states the dissociated H atom is still co-adsorbed with the hydrocarbon. Therefore, the description of the structural details for the initial state of a dehydrogenation step will be skipped except for the first dehydrogenation step. Because the structural aspects of the pathways leading to 2MP, 3MP and  $n\text{Hx}$  are really very similar, the same individual step leading to different products will be in the following described collectively. For this reason, in the following I often use the plural form of a word when referring to *transition states* and *intermediates*; although only one single reaction step is discussed at a time.

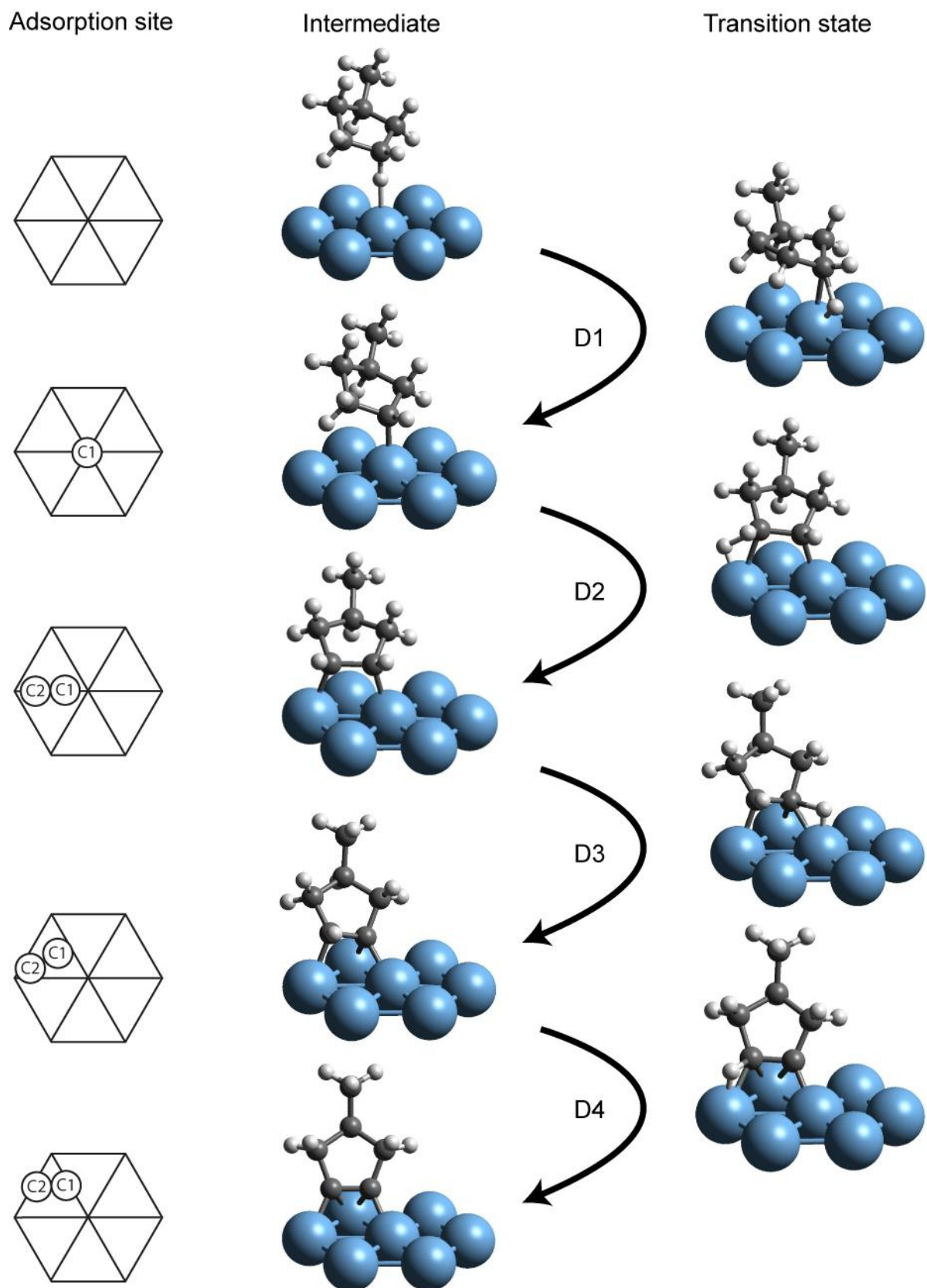


**Figure 4.3** Optimized structures and a schematic illustration of the adsorption modes pertinent to the dehydrogenation steps in the reaction path to 3MP on Pt(111). C1 and C2 denote the two C atoms directly bound to Pt(111).

*First dehydrogenation reaction (D1).* There are three possibilities for the first dehydrogenation reaction, differing in the position of the methyl group, which could be attached at either C1, C2 (C5) or C3 (C4). The initial states of these three reactions are nearly identical, with MCP weakly adsorbed at a top site over Pt(111) via an H atom attached to C1 atom (Fig. 4.3). The linear fragment Pt–H–C1 is perpendicular to the surface, with H–Pt = 210–211 pm. Due to the H–Pt interaction, the C–H bond is slightly elongated to 114 pm, hence 4 pm longer than the other C–H bonds. The three physically adsorbed intermediates are weakly bound to the surface, with adsorption energies of 16–18 kJ mol<sup>-1</sup>. However, it is well known that the GGA functional used in this work is unable to describe such weak interactions in a quantitative way.<sup>107</sup>

In the transition states, the adsorbates move closer to the surface, with the C1 atom attached to Pt(111) at a top site (Fig. 4.3). The H atom, which originally occupied this top site, is pushed to a neighboring bridge site. Similar to the initial states, the transition states of the three alternative pathways differ mainly in the position of the methyl substituent. Also, when CH<sub>3</sub> is attached at the C1 position, steric hindrance leads to an elongation of the dissociating C–H bond, which is 13 pm longer than in the transition structures with the CH<sub>3</sub> group at the C2 or C3 positions. The total energies of the transition states are also slightly affected by this steric hindrance. The structure with CH<sub>3</sub> attached to C1 is ~11 kJ mol<sup>-1</sup> less stable than the most stable one, with CH<sub>3</sub> at the C3 position (Fig. 4.4).

In the final states, the hydrocarbons are chemically adsorbed at a top site with a single C–Pt bond (Fig. 4.3). Again, in the case where the methyl group is attached at the C1 position, the steric hindrance elongates the C1–Pt bond to 219 pm, which is 6–7 pm longer compared to the values when CH<sub>3</sub> is at C2 or C3 positions. Simultaneously, the Pt atom that binds the hydrocarbon, is notably pulled out of the surface, by about 50 pm in the case where the methyl group is at the C1 position. This adsorbate-induced distortion is about twice as large as for the other two final states.

The activation energies of D1 for the discussed pathways with the methyl group at different positions lie in a narrow range, between 85–97 kJ mol<sup>-1</sup> (Fig. 4.4, Table 4.1). However, the reaction energies vary a lot. The reaction is endothermic by 36 kJ mol<sup>-1</sup> when the methyl group is attached to C1, while the two alternative reactions are essentially thermoneutral (Fig. 4.4). This difference as well as the slightly higher barrier in the case with

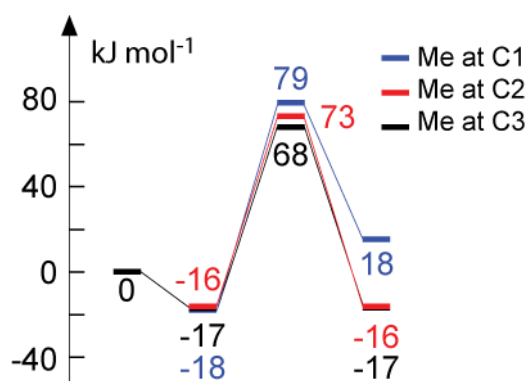


**Figure 4.4** The energy profile of the first dehydrogenation steps on Pt(111). The reference system is MCP in the gas phase and the clean Pt(111) surface.

the methyl group at C1 position are due to the steric hindrance which was mentioned above.

*Second dehydrogenation reaction (D2).* There are several possibilities for a series of dehydrogenation reactions to form an  $\alpha\alpha\beta\beta$ -tetra-adsorbed or  $\alpha\alpha\beta$ -tri-adsorbed intermediate from MCP. The reaction pathways considered in this thesis are those with the lowest barrier for the first dehydrogenation step, i.e. those involving the structures with the methyl substituent at the C3 position (or at C4) on the way to 2MP (3MP) or at the C2 position on the way to  $n$ Hx, with the first dehydrogenation barriers below  $89 \text{ kJ mol}^{-1}$ . In addition, for the second dehydrogenation step, there are at least two options,  $\alpha$ - or  $\beta$ -elimination, competing with each other to form two different kinds of the final products,  $\alpha\alpha$ -di-adsorbed or  $\alpha\beta$ -di-adsorbed intermediates. It was observed experimentally<sup>66</sup> that  $\beta$ -elimination reactions of a hydrocarbon fragment on Pt(111) were preferred over  $\alpha$ -elimination reactions. This observation was confirmed by later theoretical studies on Pt(111)<sup>148</sup> and Pd(111)<sup>65</sup> surfaces, with barriers for  $\beta$ -elimination reactions by  $10\text{--}25 \text{ kJ mol}^{-1}$  lower than for  $\alpha$ -elimination (at  $1/9$  coverage). Thus, only  $\beta$ -H elimination reactions were considered for step D2 to form  $\alpha\beta$ -di-adsorbed intermediates.

In the initial states, hydrocarbons are adsorbed at a top site as already described in the discussion of the first dehydrogenation step. In the transition states (Fig. 4.3), the dissociating H atom moves to a top site with  $\text{H-Pt} \approx 160 \text{ pm}$  and the C-H bond elongated to  $155\text{--}165 \text{ pm}$ . The C2 center, with the dissociating H atom, is already attached to the surface. Similar to the first dehydrogenation step, the steric hindrance again affects the structures both geometrically and energetically when  $\text{CH}_3$  binds to C2. The C2-Pt distance is  $14 \text{ pm}$  longer, and the

**Table 4.1:** Optimized geometries<sup>a</sup> (pm) and energy characteristics (kJ mol<sup>-1</sup>) of the transition states pertinent to the MCP ring-opening reactions over Pt(111) for various locations of the methyl (Me) substituent.

Reaction step <sup>b</sup>	2MP as product (Me at C3)				3MP as product (Me at C4)				<i>n</i> Hx as product (Me at C2)			
	C-H <sup>c</sup>	H-Pt <sup>c</sup>	$\Delta E^d$	$E_a^e$	C-H <sup>c</sup>	H-Pt <sup>c</sup>	$\Delta E^d$	$E_a^e$	C-H <sup>c</sup>	H-Pt <sup>c</sup>	$\Delta E^d$	$E_a^e$
D1	148	167, 214	0	85	148	167, 214	0	85	148	167, 213	0	89
D2	157	160	-31	55	155	160	-30	57	165	159	-17	65
D3	155	162	21	84	155	162	24	88	156	162	26	86
D4 <sup>f</sup>	144	163	-18	60	144	163	-20	58				
Migration <sup>f</sup>			60	61			60	61				
CC			-21	15			-21	14			-19	116
C-shift1 <sup>f</sup>			-71	14			-73	15				
C-shift2 <sup>f</sup>			-12	50			-10	52				
H1 <sup>f</sup>	144	164	66	80	142	165	55	76				
H2	158	161	-4	56	155	161	-12	59	158	161	12	65
H3	156	170, 204	-43	66	150	168, 217	-24	72	161	175, 185	-57	52
H4 <sup>g</sup>	136	166	78	83					135	167	78	81
H5 <sup>g</sup>									157	162	-18	64
H6 <sup>g</sup>									152	166, 221	-12	63

<sup>a</sup> A–B, distance between atoms A and B in the transition state. <sup>b</sup> D1–D4 denote the first to fourth dehydrogenation steps; CC stands for the C–C bond breaking step; H1–H6 refer to the first to sixth hydrogenation steps. <sup>c</sup> Bonds that are breaking/forming during a reaction. <sup>d</sup> Reaction energy. <sup>e</sup> Activation energy. <sup>f</sup> The reaction path to *n*Hx does not contain this step. <sup>g</sup> The fourth to sixth hydrogenation steps for 2MP and 3MP are expected to have energy profiles very close to the respective hydrogenation steps for *n*Hx.

absolute energy is 8–15 kJ mol<sup>-1</sup> higher than the case with the CH<sub>3</sub> substituent at C3 or C4 positions. In the final states (Fig. 4.3), the C–H bond totally breaks, while the H atom moves to the neighboring hollow site on the surface. The adsorption mode of the hydrocarbon in the final states is the same as in the transition states, with two  $\sigma$  bonds at a bridge site. This reaction step is exothermic, by 17–31 kJ mol<sup>-1</sup>, for all the three considered reactions. The activation energies of this step are only 55–65 kJ mol<sup>-1</sup>, i.e., 24–30 kJ mol<sup>-1</sup> lower than the barriers calculated for the first dehydrogenation step (Table 4.1).

*Third dehydrogenation reaction (D3).* Similar to the discussion of the second dehydrogenation step, the choice of the third dehydrogenation step is also not unique. The

third H atom can be split either from C1 or C2 atom. Since the position of the methyl group does not significantly affect the barriers (Fig. 4.5, Table 4.1), the H atom was chosen to be removed from the center C1 in all the three considered reaction paths.

In the transition states, the hydrocarbon moves to a hollow site (Fig. 4.3). The carbon atom, with the dissociating H atom, forms a second bond with a Pt center, while the H atom interacts with both Pt (162 pm) and C (155–156 pm) atoms, forming the typical H–Pt–C three-member-ring structure. In the final states, the hydrocarbon adsorbates attach to the surface in  $\mu_3\text{-}\eta^2$  fashion at the same hollow site as in the respective transition states, with the dissociated H atom co-adsorbed at a neighboring hollow site (Fig. 4.3).

Energetically, this reaction step is endothermic by 21–26 kJ mol<sup>-1</sup>. The corresponding activation energy was obtained in the range 84–88 kJ mol<sup>-1</sup> (Table 4.1). In view of this relatively high barrier, the transition state of the C–C bond cleavage from a  $\alpha\beta$ -dehydrogenated intermediate, which is the initial state of the third dehydrogenation step, was also located. The calculated result shows a barrier as high as 148 kJ mol<sup>-1</sup>, which is significantly higher than the barrier of the third dehydrogenation step, and is also higher than the barriers for C–C bond cleavage of tri- and tetra-dehydrogenated intermediates (see below).

*Fourth dehydrogenation reaction (D4).* In step D4, only the two pathways leading to 2MP or 3MP were addressed. On the pathway to *n*Hx, there are no further H atoms on C1 or C2 to be dehydrogenated due to the methyl substituent, which connects to C2. After the three dehydrogenation steps discussed above, the hydrocarbons adsorb at a three-fold hollow site in  $\mu_3\text{-}\eta^2$  fashion. In the transition states, the C2 center forms a second bond with the Pt surface, leading to a nearly parallel conformation between the C–C bond and one of the Pt–Pt bonds of the adsorbing hollow site (Fig. 4.3). The backbone of the ring is almost normal to the Pt(111) surface. The dissociating H atom migrates to a top site. In the various final states, the adsorption mode of the hydrocarbon is similar to that in the corresponding transition state, except the C–H bond is completely broken (Fig. 4.3). This reaction is exothermic by 18–20 kJ mol<sup>-1</sup> and the barrier of this reaction is not very high, 58–60 kJ mol<sup>-1</sup> (Table 4.1).

*C–C bond breaking reactions over Pt(111).* The  $\alpha\alpha\beta\beta$ -tetra-adsorbed or  $\alpha\alpha\beta$ -tri-adsorbed intermediates are generated after a sequence of dehydrogenation reactions as described above. The  $\alpha\alpha\beta\beta$ -tetra-adsorbed intermediates, 3-methylcyclopentyne and 4-methylcyclopentyne, will finally convert to 2MP and 3MP, respectively, while  $\alpha\alpha\beta$ -tri-

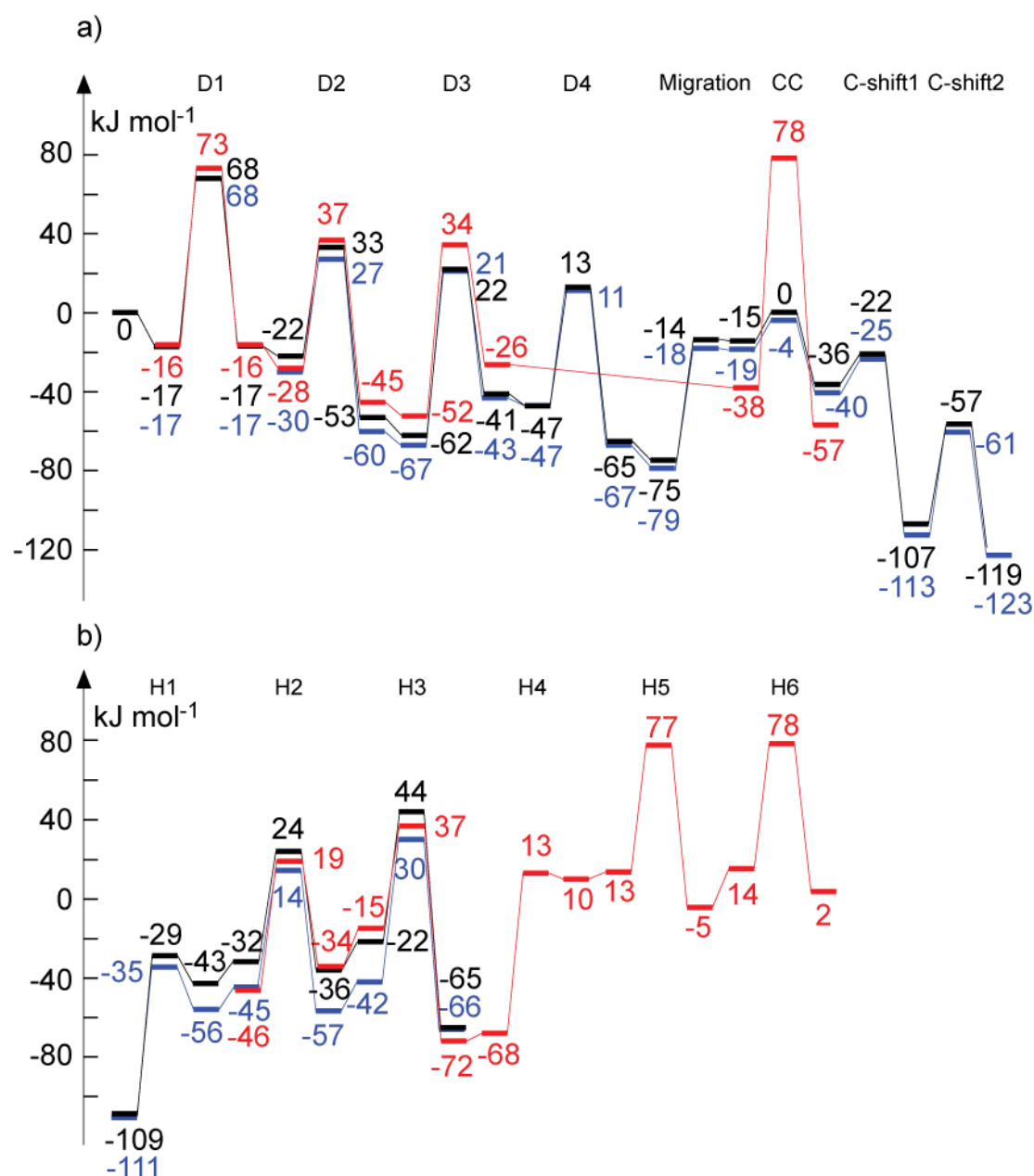


**Figure 4.5.** The energy profiles (kJ mol<sup>-1</sup>) of the MCP ring-opening reactions over Pt(111): reaction path to 2MP – blue; reaction path to 3MP – black; reaction path to *n*Hx – red. Energies are calculated relative to MCP(g) and the clean 3×3 Pt(111) slab. For a system containing *x* H atoms in the unit cell with energy  $E_{\text{unitcell}}$ , the relative energy is defined as  $E = E_{\text{unitcell}} + (12-x)(E_{\text{H/Pt(111)}} - E_{\text{Pt(111)}}) - E_{\text{MCP(g)}} - E_{\text{Pt(111)}}$ .  $E_{\text{H/Pt(111)}}$ ,  $E_{\text{MCP(g)}}$  and  $E_{\text{Pt(111)}}$  are the total energies of H adsorbed on Pt(111) at 1/9 coverage, of MCP (in the gas phase) and of the clean 3×3 Pt(111) slab, respectively. The energy shifts between two hydrogenation / dehydrogenation steps reflect the differences between structures with a co-adsorbed H atom in the unit cell and an H atom at an infinite separation (i.e. calculated separately on Pt(111) at 1/9 coverage).

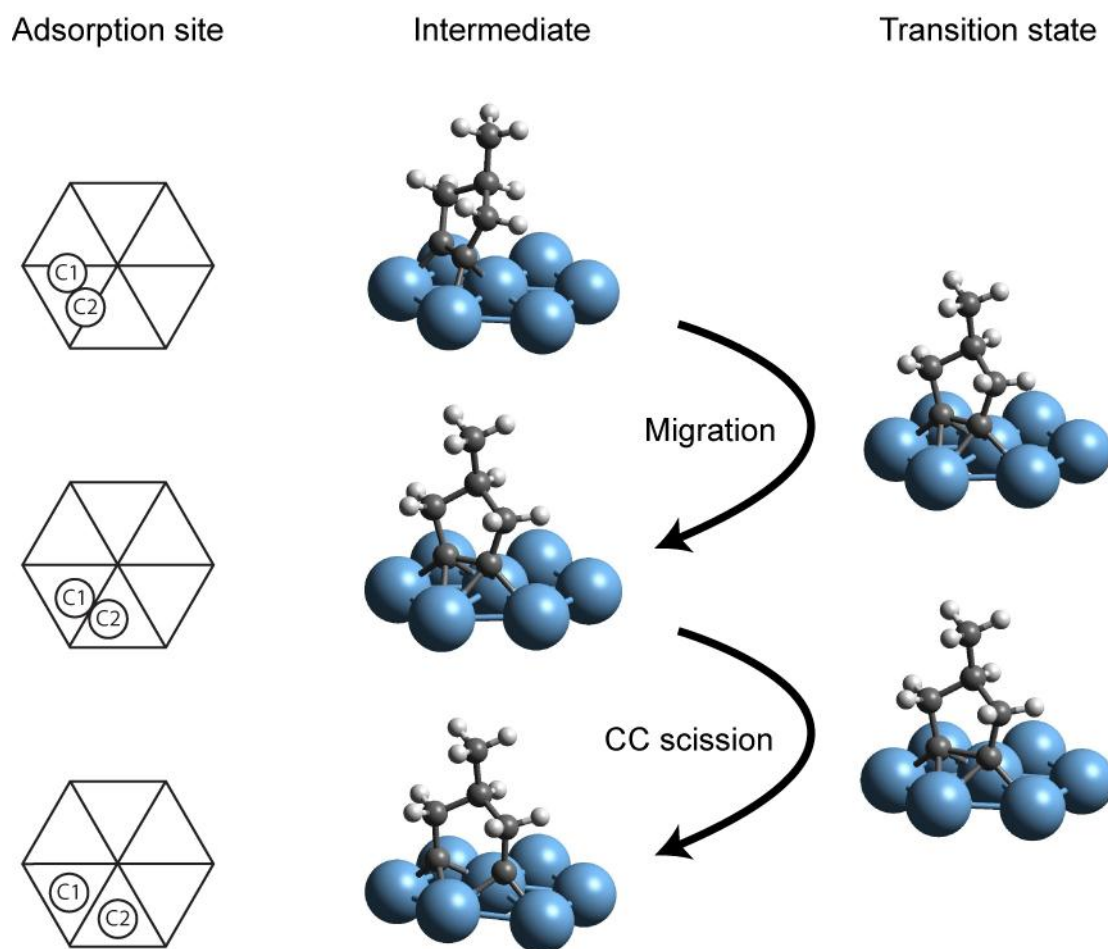


**Figure 4.6.** Optimized structures and sketches of the adsorption modes for the migration, C–C bond breaking on the way to 3MP over Pt(111). C1 and C2 denote the two C atoms directly bound to Pt(111).

adsorbed 2-methyl-1-cyclopenten-1-yl will convert to  $n\text{Hx}$ . The C–C bond breaking reactions for the  $\alpha\alpha\beta\beta$ -tetra-adsorbed and  $\alpha\alpha\beta$ -tri-adsorbed intermediates behave differently, and they will be discussed separately in this section.

*C–C bond breaking in the tetra-dehydrogenated intermediates.* As mentioned above in the discussion of the fourth dehydrogenation step, the ring structures of  $\alpha\alpha\beta\beta$ -tetra-adsorbed intermediates are nearly normal to the Pt(111) surface and the C–C bond is located above a threefold hollow site, each C atom forming two C–Pt bonds in a bridge fashion (Fig. 4.6). The attempt to find a first-order transition state for the direct C–C bond breaking from this intermediate failed. Instead, a second-order transition state, with a high barrier, at  $130 \text{ kJ mol}^{-1}$ , was located. The imaginary modes of this transition state correspond to a migration of

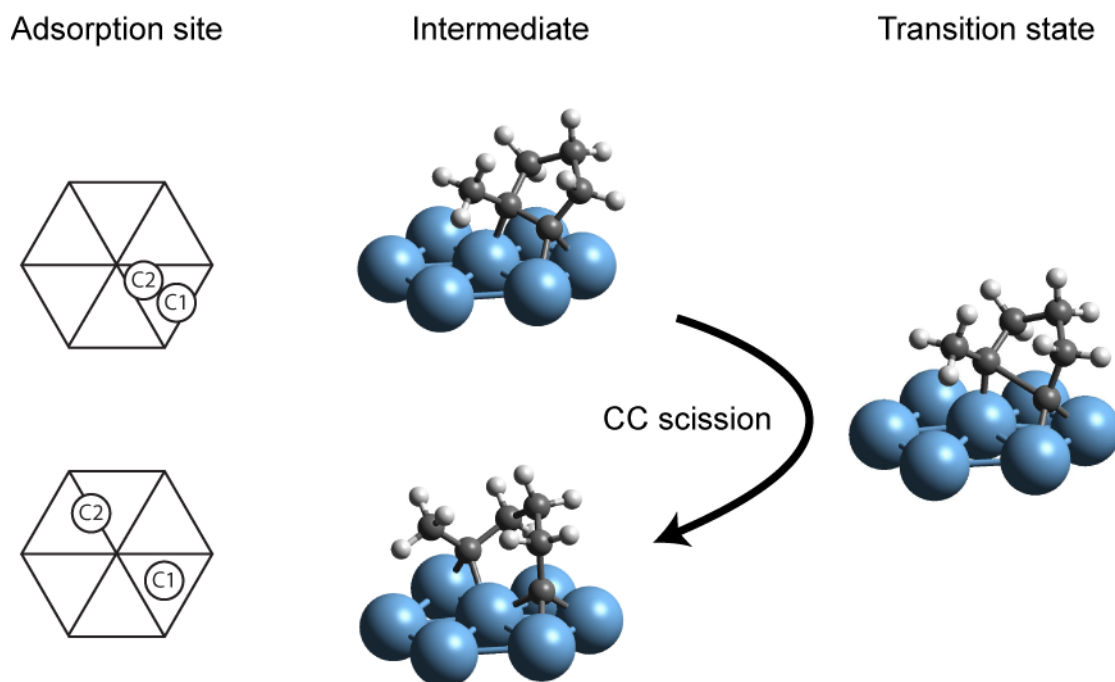


**Figure 4.7.** Optimized structures and sketches of the adsorption modes for and C–C bond breaking on the way to  $n\text{Hx}$  over Pt(111). C1 and C2 denote the two C atoms directly bound to Pt(111).

the whole molecule in the direction of an adjacent three-fold hollow site and C–C bond stretching. Therefore, another intermediate is needed in the lowest energy pathway of C–C bond breaking.

Indeed, an additional step, in the following referred to as “migration step”, is added to the reaction scheme. In this step, the whole structure of the adsorbate rotates by  $\sim 30^\circ$  about an axis perpendicular to the surface, through the Pt atom that connects to two C atoms (Fig. 4.6, Migration). After the rotation, the two C atoms occupy two adjacent threefold hollow sites, with the adsorbed C–C bond perpendicular to the Pt–Pt bond which is shared by these two hollow sites (Fig. 4.6). The C–C bond length is slightly increased to 148 pm, 6 pm longer than the one in the initial state. This step is strongly endothermic by about  $60 \text{ kJ mol}^{-1}$ , with a very low reverse reaction barrier,  $1 \text{ kJ mol}^{-1}$  (Table 4.1). Multiple adsorption modes of similar nature were also previously reported for acetylene adsorbed on transition metal surfaces.<sup>149</sup>

In a subsequent step, the C–C bond finally breaks. In the transition states of this step (on the path to 2MP or 3MP), the C–C bond length is stretched to 176–178 pm, 28–30 pm longer than it in the initial states. In the final states, the C–C completely breaks, as reflected by the

237 pm distance. This reaction step is exothermic by 21 kJ mol<sup>-1</sup>. The activation energies of this elementary step are surprisingly low, only 14–15 kJ mol<sup>-1</sup> (Table 4.1). However, the barriers for the reverse reaction of the previous migration step are only 1 kJ mol<sup>-1</sup>. Thus, the total barrier should be calculated relative to the most stable configuration of the tetra-adsorbed cyclic species, the initial state of the migration step. Therefore, the total barriers for the combined migration and C–C bond breaking amount to 74–75 kJ mol<sup>-1</sup>.

*C–C bond breaking in the tri-dehydrogenated intermediate.* At variance with the two-step cleavage of the tetra-dehydrogenated intermediate, there is no additional reaction step before the C–C bond breaking from the tri-dehydrogenated intermediate. In the initial state, the hydrocarbon adsorbs over a three-fold hollow site in  $\mu_3\text{-}\eta^2$  fashion, with a C–C distance of 150 pm (Fig. 4.7). In the transition state, the C atom with the methyl group attached to it moves towards a top site, while the other adsorbed C atom slightly shifts to the center of the hollow site (Fig. 4.7). The C–C bond elongates to 212 pm. In the final state, the former C atom moves further to a bridge site, while the other C remains attached at the same hollow site as in the initial state. The C–C bond breaks completely, as manifested by the C–C distance of 303 pm. This reaction is exothermic by 19 kJ mol<sup>-1</sup>, with a relatively high barrier, 116 kJ mol<sup>-1</sup>. This barrier is at least 27 kJ mol<sup>-1</sup> higher than the barriers of the preceding dehydrogenation reactions (Table 4.1).

**Hydrogenation reactions over Pt(111).** After the C–C bond breaking step, a series of hydrogenation steps is required to obtain the final products, 2MP, 3MP, or *n*Hx. Similar to the dehydrogenation reactions of MCP discussed above, there are several choices of the sequence for hydrogenating two unsaturated C centers. The hydrogenation can proceed according to the following two major routes: (i) first, total hydrogenation of one terminal carbon center, followed by the total hydrogenation of the second carbon center, or (ii) alternating hydrogenation steps at the two terminal carbon centers. In Chapter 3, the calculation on the ethylene transformations over Pt(111) showed that the barrier to hydrogenate a carbene species CHCH<sub>3</sub>, 68 kJ mol<sup>-1</sup>, is 21 kJ mol<sup>-1</sup> lower than the hydrogenation barrier of the carbyne species CCH<sub>3</sub>. Thus, one expects that the second hydrogenation step of a carbynic C, i.e. hydrogenation of a carbene species, should be easier than its first hydrogenation step. This fact speaks in favor of route (i) — complete hydrogenation of one carbon center followed by the hydrogenation of the other, due to the high activation energies for hydrogenating of the carbyne center (H1, H4). In the following, the hydrogenation steps will be discussed one by

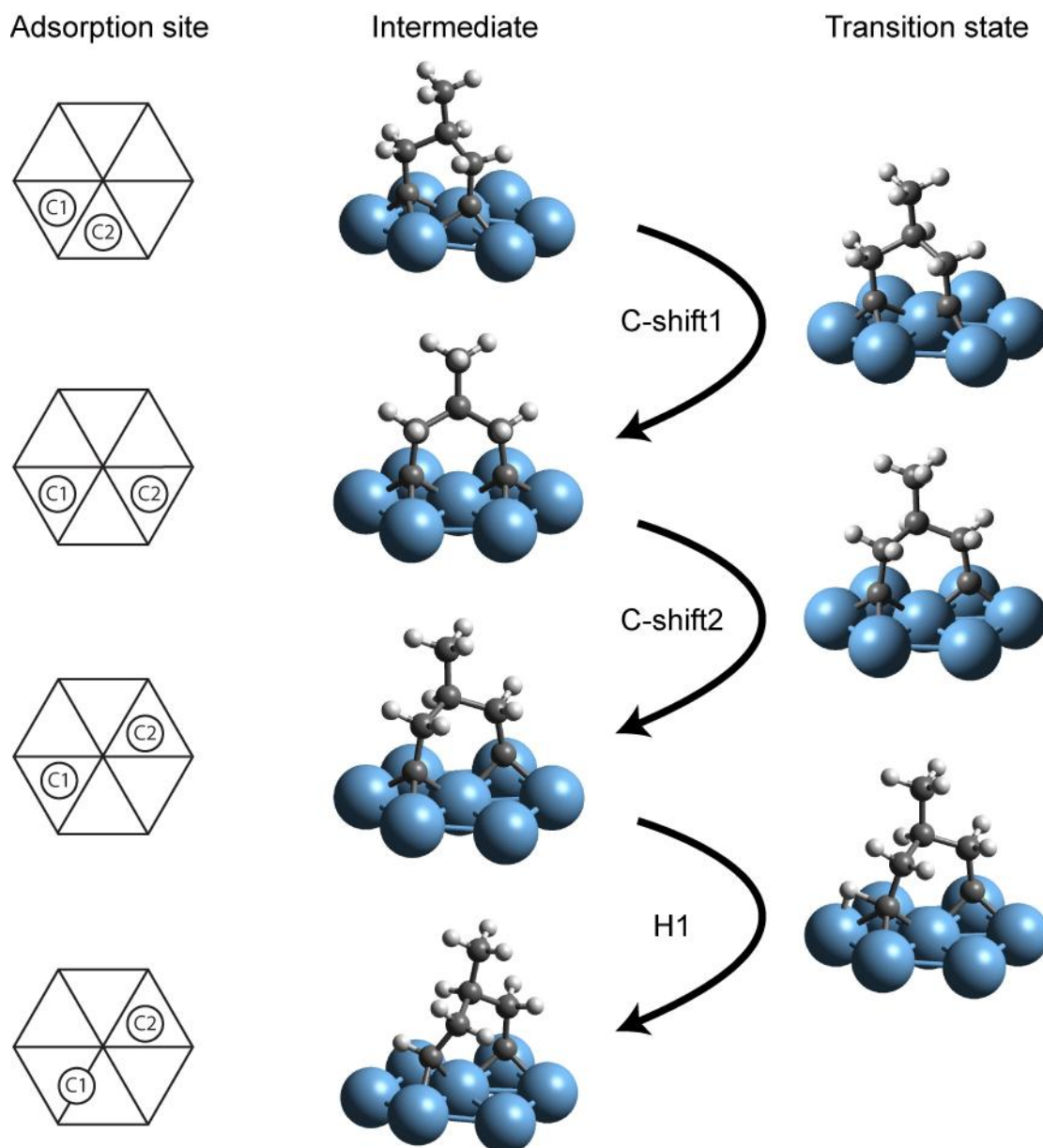


**Figure 4.8.** Optimized structures and a schematic illustration of the adsorption modes for the C-shift reactions and the first hydrogenation step on the way to 3MP over Pt(111). C1 and C2 denote the two C atoms directly bound to Pt(111).

one. Due to the methyl substituent, only five hydrogenation steps (H2–H6) are required to produce  $n\text{Hx}$  from the corresponding ring-cleavage final state.

*C shift reactions (C-shift1, C-shift2).* Only the pathways to 2MP and 3MP contain these reaction steps. After the C–C bond breaking step, the generated intermediates, 2-methylpentan-1,5-diylidyne and 3-methylpentan-1,5-diylidyne on the reaction paths to 2MP and 3MP, respectively, are adsorbed at two adjacent three-fold hollow sites. However, it is not

the most stable adsorption mode for these intermediates. One of the terminal C atoms can shift to the neighboring hollow site which is farther apart from the other terminal C atom (Fig. 4.8, C-shift1). C-shift1 results in an adsorption complex that is about  $70 \text{ kJ mol}^{-1}$  more stable. Both barriers, to 2MP and 3MP, for this process are very low,  $15 \text{ kJ mol}^{-1}$ , much lower than typical barriers for hydrogenation reactions ( $\sim 50\text{--}100 \text{ kJ mol}^{-1}$ ) (Table 4.1). Thus, the direct hydrogenation of the C–C bond breaking products on the way to 2MP and 3MP is not included in this thesis.

After the C-shift1 reaction, the two terminal C atoms are adsorbed at two hollow sites separated by another threefold hollow site (Fig. 4.8). The barriers for the hydrogenation reaction of the C-shift1 products are relatively high,  $95\text{--}97 \text{ kJ mol}^{-1}$ . Thus, another shift reaction is suggested, whereby one terminal C atom is further moved to a neighboring threefold hollow site to form a conformation with two carbynic C atoms sitting diametrically opposite to each other in a hexagon (Fig. 4.8). This reaction is slightly exothermic, by  $10\text{--}12 \text{ kJ mol}^{-1}$ , and the activation energies are also not very high,  $50\text{--}52 \text{ kJ mol}^{-1}$  (Table 4.1). After this additional rearrangement, the barrier of the subsequent hydrogenation step (H1) is decreased by  $\sim 20 \text{ kJ mol}^{-1}$ .

*First hydrogenation reaction (H1).* After the two C-shift reactions, the carbynic C atom is hydrogenated with a moderate barrier. There are two possibilities for adding the first hydrogen in the reaction pathway to 2MP due to the asymmetric structure. As the energetics of dehydrogenation / hydrogenation reactions are not sensitive to the position of the methyl group at C3–C5 (as shown above in our discussion on the dehydrogenation reactions, Table 4.1), the terminal C atom close to the methyl group is chosen to be hydrogenated first. In the transition states, the attacking H atom moves to a top site with the C–H distance at  $142\text{--}144 \text{ pm}$ ; concomitantly, the hydrogenated C atom is pushed backward with a longer C–Pt distance at  $223\text{--}224 \text{ pm}$  in the H–C–Pt three-member-ring (Fig. 4.8). In the final states, the H-receiving C atom is adsorbed at a bridge site (Fig. 4.8). The C–H bond length is shortened to  $111 \text{ pm}$ , which is a typical length for a C–H bond with the current GGA functional. The reactions are strongly endothermic, by  $55\text{--}66 \text{ kJ mol}^{-1}$ . The barriers for these reactions are  $76\text{--}80 \text{ kJ mol}^{-1}$  (Table 4.1).

As a side remark, I want to comment on why the first hydrogenation reaction of the C-shift2 products is more favorable than the hydrogenation reaction of the C-shift1 products. The former step has a lower barrier than the latter, by  $\sim 20 \text{ kJ mol}^{-1}$ . The barrier lowering is

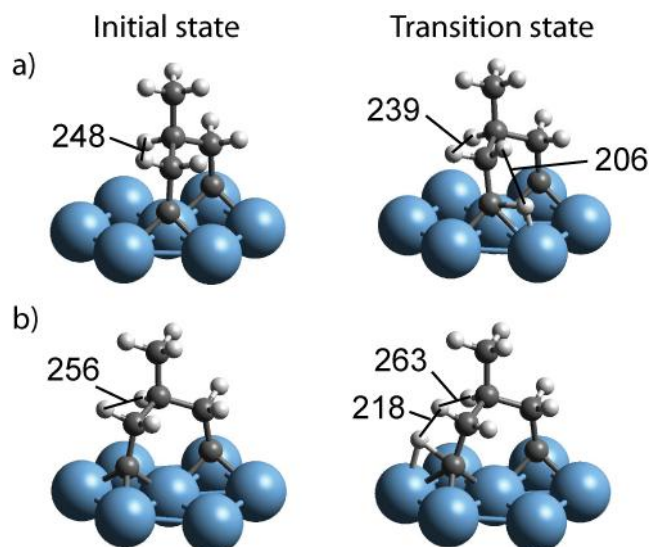


**Figure 4.9.** Optimized initial and transition state structures of the hydrogenation step a) from the product of the C-shift1 reaction; b) from the product of the C-shift2 reaction. Total hydrogenation of both intermediates will form 3MP.

due to a sterically less constrained transition state structure of the latter hydrogenation reaction. For example, the H–H distance between the attacking H atom and the nearest H atom of the hydrocarbon chain is 218 pm in the transition state of the hydrogenation reaction after the C-shift2 reaction. However, this distance is 12 pm shorter in the hydrogenation step direct from the C-shift1 product (Fig. 4.9), leading to stronger repulsion between these two centers in the latter case. Similarly, the nearest intra-molecular H–H distance is also different in two cases. Compared with the corresponding initial state, this distance becomes 9 pm shorter in the hydrogenation transition state of the C-shift1 product, while it is 7 pm longer in the hydrogenation transition state of the C-shift2 product than the corresponding initial state (Fig. 4.9). This indicates a more relaxed structure in the latter transition state. Both findings suggest that the hydrogenation transition state of the C-shift2 product is structurally more relaxed compared with the one of the C-shift1 product, thus rationalizing the lower barrier of the hydrogenation step after the C-shift2 reaction.

*Second hydrogenation reaction (H2).* This step is present in all three reaction pathways leading to 2MP, 3MP and *n*Hx. In the transition states, the attacking H atom moves to a top site and again a Pt–H–C three-member-ring is formed (Fig. 4.10). The C–Pt bond length is elongated, e.g. in the reaction pathway to *n*Hx, by 19 pm, compared to the 210 pm in the initial state. In the final states, this hydrogenated C center moves to a top site of the original

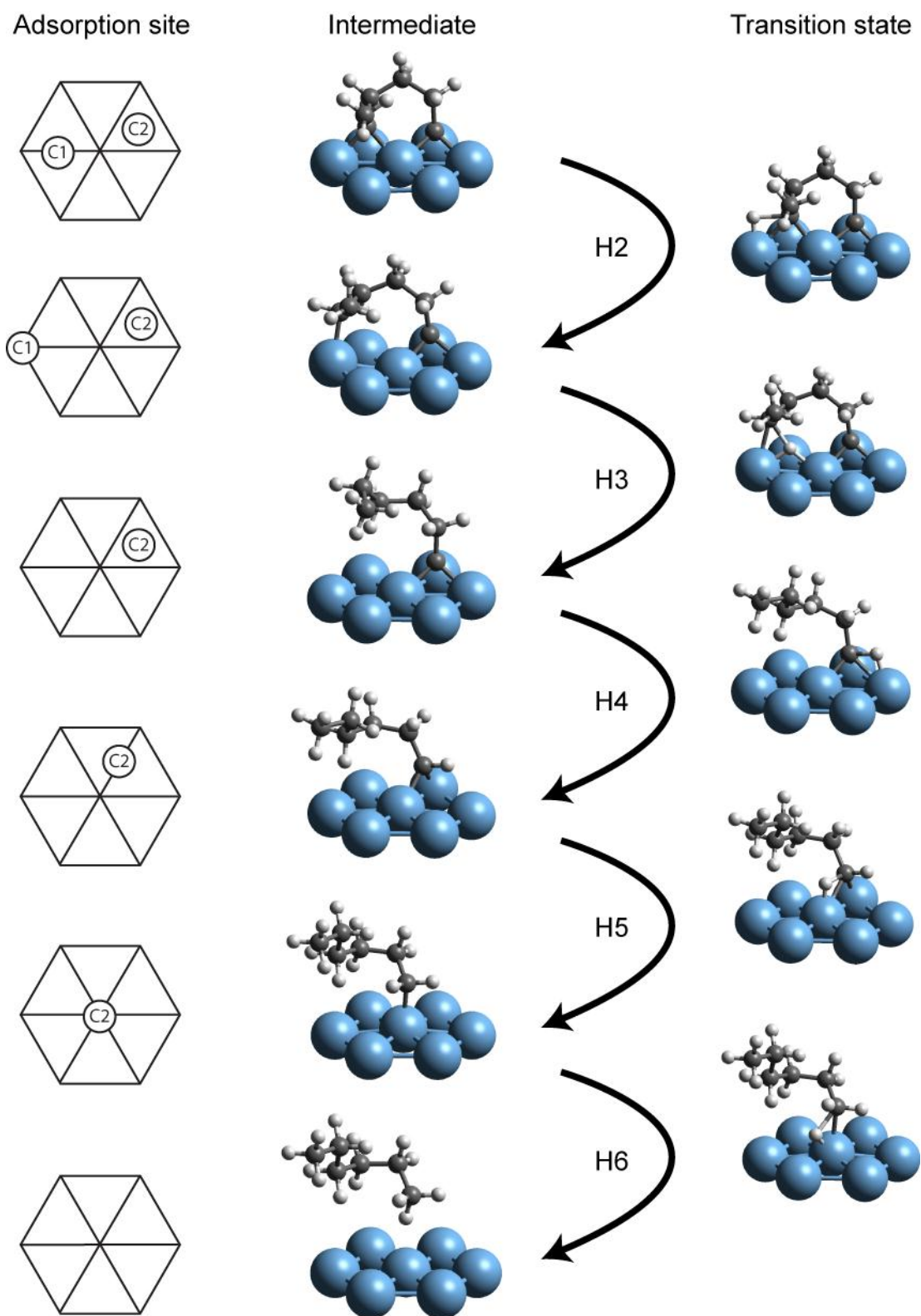


**Figure 4.10.** Optimized structures and sketches of the adsorption modes for the second to the sixth hydrogenation step on the way to 3MP over Pt(111). C1 and C2 denote the two C atoms directly bound to Pt(111).

bridge site (Fig. 4.10). The hydrogenation is  $12 \text{ kJ mol}^{-1}$  endothermic in the reaction path to  $n\text{Hx}$  and slightly exothermic by  $4\text{--}12 \text{ kJ mol}^{-1}$  in the other two cases. The activation energies of this reaction step are  $56\text{--}65 \text{ kJ mol}^{-1}$  (Table 4.1).

*Third hydrogenation reaction (H3).* In the transition states the attacking H atom moves to a neighboring bridge site of the adsorbate (Fig. 4.10). Two asymmetric H–Pt bonds are formed of  $168\text{--}175$  and  $185\text{--}217$  pm. Similar to the first hydrogenation step, the C–Pt bond length is also increased due to the presence of the attacking H atom. In the final states, the hydrogenated C atom is totally desorbed from the surface (Fig. 4.10). This reaction is strongly exothermic, by  $24\text{--}57 \text{ kJ mol}^{-1}$  and activation energies of this reaction are  $52\text{--}72 \text{ kJ mol}^{-1}$  (Table 4.1).

*Fourth hydrogenation reaction (H4).* After the first three hydrogenation steps, 3–methylpentylidyne, 4–methylpentylidyne or hexylidyne are adsorbed on the surface in similar fashion: one terminal C atom has been fully hydrogenated and detached from the surface whereas the other one (of a carbene type) still adsorbs at a threefold hollow site. Test calculations showed that the total energies of the initial, transition, and final state for the hydrogenation of 4–methylpentylidyne are only about  $3\text{--}5 \text{ kJ mol}^{-1}$  lower than the corresponding states in the hydrogenation step of hexylidyne. Therefore, these hydrogenation steps (H4–H6) are assumed to have very similar barriers as the analogous hydrogenation steps on the way to  $n\text{Hx}$ . In the following three steps (H4–H6), only the transition states in the reaction pathway to  $n\text{Hx}$  were located.

In the transition state of reaction H4, the H atom moves to a top site. The hydrogenated C atom is pushed a little away from the center of the threefold hollow site (Fig. 4.10). The C–Pt bond in the C–Pt–H three-member-ring increases to  $230$  pm, compared to  $204$  pm in the initial state. The H–C distance is only  $135$  pm, which is shorter than a typical H–C distance ( $>140$  pm) in the transition state. In the final state, the H–C distance further shortens to  $112$  pm and the C atom moves to a bridge site (Fig. 4.10). This reaction is strongly endothermic, by  $78 \text{ kJ mol}^{-1}$ . The activation energy of this reaction is  $81 \text{ kJ mol}^{-1}$  whereas the barrier for the reverse dehydrogenation reaction is only  $3 \text{ kJ mol}^{-1}$  (Table 4.1).

*Fifth and sixth hydrogenation reactions (H5 and H6).* The reactive parts of the transition state structures in these two hydrogenation steps are quite similar to those of the second and third hydrogenation steps, respectively. The main structural difference is that in

reactions H5 and H6 the other (non-reactive) terminal C atom is no longer attached to the surface. Therefore, the structures of these two reactions will not be described in detail. The reaction energies of these two reaction steps are exothermic by  $18 \text{ kJ mol}^{-1}$  and  $12 \text{ kJ mol}^{-1}$ , respectively. The activation energies for these two steps are  $64 \text{ kJ mol}^{-1}$  and  $63 \text{ kJ mol}^{-1}$  (Table 4.1).

## 4.2.2 Reactions on small Pt particles

Several experimental studies indicated that the selectivity to  $n\text{Hx}$  increased when the MCP ring-opening reaction is catalyzed by small Pt particles, which feature a higher proportion of low-coordination edge and defect sites compared to large particles.<sup>124</sup> In order to check the effect of the surface defects on the selectivity, the ring-opening reaction of MCP was calculated on a stepped surface, Pt(211), which consists of (111) terraces, three rows wide, separated by line defects, i.e. steps of atomic height. Indeed, one of the earlier experimental studies suggested that the C–C bond breaking is more facile on the stepped or kinked Pt surfaces.<sup>150</sup>

In order to focus the computational effort on a more relevant part of the problem, the hydrogenation and dehydrogenation reactions on the stepped surface were not addressed. Previous computational studies on the dehydrogenation of propane<sup>145</sup> and ethane<sup>73</sup> also showed that the barriers of reactions analogous to the dehydrogenation reactions in this thesis over stepped surfaces Pt(211) and Pt(110) lie in the range of  $20\text{--}70 \text{ kJ mol}^{-1}$ , i.e. below the typical activation energies of C–C scission. Thus, the computational study focused on the C–C bond breaking steps over the surface Pt(211).

The stepped surface offers adsorption sites different from those of the Pt(111) surface; these additional possibilities will be discussed in detail in the following. The initial states were selected such that the adsorbed hydrocarbon has at least one direct contact with a Pt atom at the step edge. The barriers of the reaction paths not considered herein with initial states close to the step edge but without a direct interaction with edge Pt atoms, are expected to lie between the calculated barriers on Pt(111) given in Section 4.2.1 and those on Pt(211) discussed in this section. According to this selection criterion, to the best of my knowledge, I have considered all possible scenarios for the C–C scission reaction at steps, but there is still a small possibility that I missed some of the viable pathways. After all the barriers had been located, only few reaction paths could fulfill the necessary requirements of possessing both a

**Table 4.2:** Optimized geometries<sup>a</sup> (pm) and energy characteristics (kJ mol<sup>-1</sup>) of transition states of the C-C bond breaking of MCP ring-opening over Pt(211) on the way to *n*Hx.

	C-C <sup>b</sup>	BE <sup>c</sup>	ΔE <sup>d</sup>	E <sub>a</sub> <sup>e</sup>
Type 1	203	272	12	94
Type 2	221	289	85	109
Type 3	230	221	10	88
Type 4	232	202	-34	91
Type 5	213	330	-17	167

<sup>a</sup> A-B, distance between atoms A and B in the transition state. <sup>b</sup> C-C distance in the transition state of the bond to be cleaved. <sup>c</sup> Binding energy of the initial state. Note that the binding energy of the tri-dehydrogenated MCP over Pt(111) is 282 kJ mol<sup>-1</sup>. <sup>d</sup> Reaction energy. <sup>e</sup> Activation energy.

relatively low barrier and a relatively large binding energy of its initial state. The low barrier indicates that the reaction rate of this step is fast enough, while the large binding energy points to a high population of this initial state. For each of the two types of C-C bond breaking reactions considered (on the way to *n*Hx and on the way to 2MP/3MP) separately discussed in the following, only one most favorable path has been selected on the basis of the kinetic and thermodynamic requirements just mentioned. This path further labeled as Type 1 path has been designated as the most plausible C-C bond breaking elementary step in the MCP RO reaction over Pt(211). Of course, Type 1 C-C bond breaking paths on the way to *n*Hx and to 2MP/3MP are not the same.

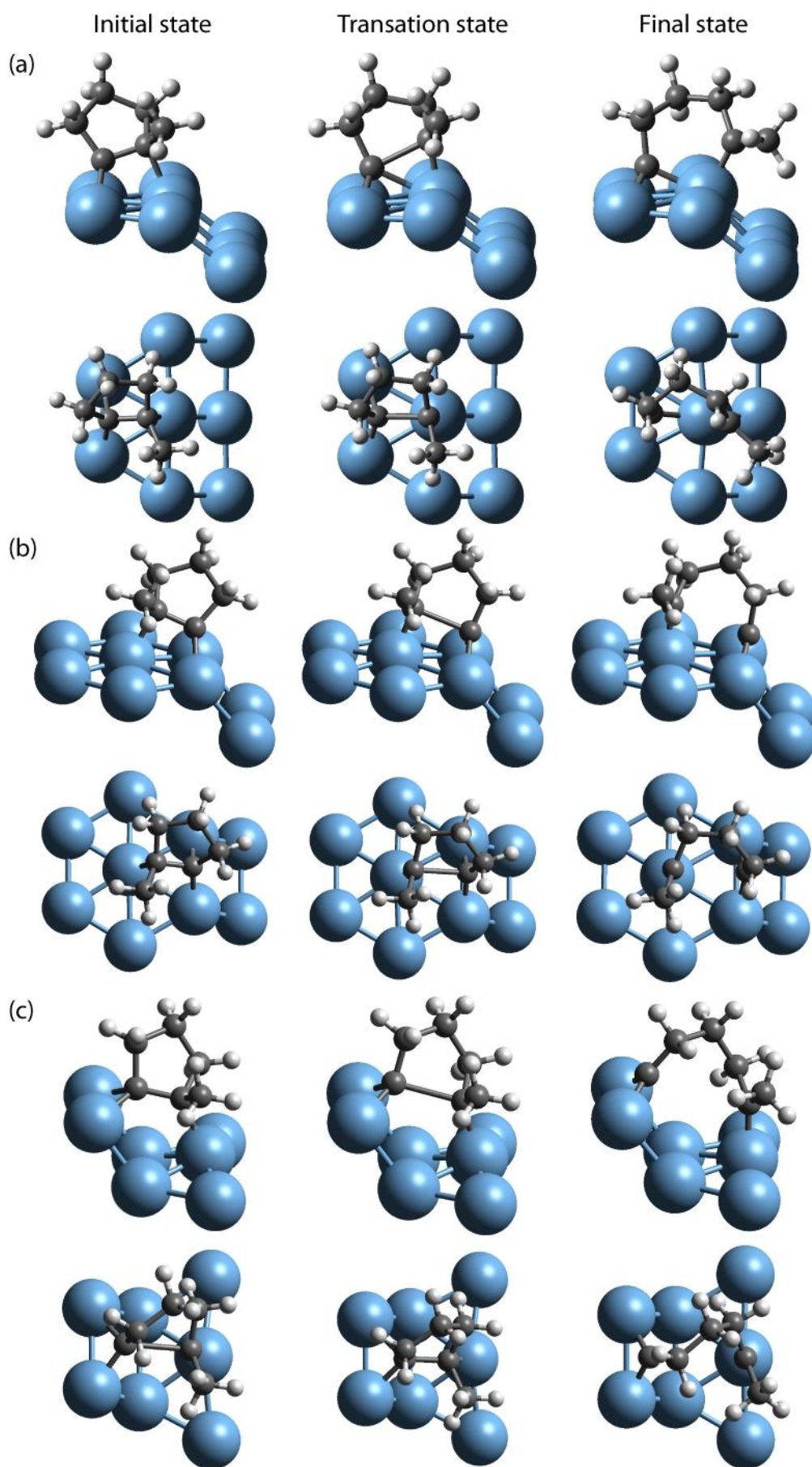
***C-C bond breaking on the reaction path to *n*Hx.*** Similar to the reaction over Pt(111), the initial state of this reaction is the tri-dehydrogenated 2-methyl-1-cyclopenten-1-yl. In total, five different initial states were considered on Pt(211), corresponding to five different reaction pathways to *n*Hx. They will be referred to as Type 1 to Type 5 in the following (Fig. 4.11).

*Type 1 - Most favorable reaction pathway.* Structurally, this path is very similar to the analogous reaction over Pt(111). In the initial state, the adsorbate is located at a hollow site of the (111) terrace near the step edge in μ<sub>3</sub>-η<sup>2</sup> fashion (Fig. 4.11a). The C center carrying the methyl substituent directly attaches to an edge Pt atom. In the transition state, this C center moves away from the terrace to the edge (Fig. 4.11a), and the C-C bond increases to 203 pm. In the final state, the C-C bond totally breaks. The terminal C atom, with the methyl group attached to it, is still bound on top of one edge Pt atom. This sp<sup>2</sup> hybridized carbon center

manifests an additional  $\pi$  interaction with the metal atoms at the step edge (Fig. 4.11a) resulting from free bonding capacities offered by undercoordinated Pt atoms at edges. This is reflected both by the 20 pm shorter C–Pt bond than the C–Pt bond with  $sp^3$  hybridized C in the initial state and by the planar geometry of the interacting C center, i.e. all three bonds formed by this C center lie nearly in the same plane. The reaction is slightly endothermic by  $12 \text{ kJ mol}^{-1}$ . The barrier of this reaction is not very high,  $94 \text{ kJ mol}^{-1}$  (Table 4.2).

*Type 2-5 - Alternative reaction pathways.* Type 2: The initial state of this reaction path is also similar to that of the analogous reaction step over Pt(111), with the hydrocarbon adsorbed at a hollow site near the step edge (Fig. 4.11b); however, at variance with Type 1, the methyl group is attached to the other chemisorbed carbon center, located farther from the edge. The transition state of this reaction step is very similar to the one over Pt(111), with the C–C bond elongating to 221 pm (Fig. 4.11b, Table 4.2). In the final state, the terminal C atom that is close to the step edge remains adsorbed at a bridge site, whereas the other C atom moves to a top site (Fig. 4.11b). Similar to the final state of Type 1 path, both terminal C atoms exhibit  $sp^2$  hybridization and bind in a  $\pi$  fashion with two edge atoms and one terrace atom, respectively, of the metal. The interaction of the terrace Pt atom and the  $sp^2$  hybridized C atom is not strong enough, leading to a strongly endothermic reaction, by  $85 \text{ kJ mol}^{-1}$ . The activation energy of this reaction is  $109 \text{ kJ mol}^{-1}$ , slightly lower than on the Pt(111) surface but higher than for Type 1 path over the Pt(211) surface (Table 4.1 and 4.2). Type 3 and Type 4: The initial states of these two reactions are very similar to each other, the tri-dehydrogenated intermediates are bound to the surface via one C atom attached to the step edge and the other C atom adsorbed on the (111) terrace across the step. The only difference between these two initial states is the position of the methyl group, either close to the edge or close to the terrace (Fig. 4.11c and 4.11d). In the transition states, the C–C bond stretches to 230–232 pm (Table 4.2). In the final states, the C–C bond is broken, with the C–C distance  $> 340 \text{ pm}$ . The reaction is endothermic by  $10 \text{ kJ mol}^{-1}$  for Type 3 and exothermic by  $34 \text{ kJ mol}^{-1}$  for Type 4. The calculated barriers are  $88\text{--}91 \text{ kJ mol}^{-1}$ , which are close to the barrier height of Type 1 (Table 4.2). However, the initial states of Type 3 and 4 are relatively less stable compared with the initial state of Type 1, as reflected by the 50 and  $70 \text{ kJ mol}^{-1}$  smaller adsorption energies (Fig. 4.12, Table 4.2). Therefore, Type 1 should be more favorable than Types 3 and 4.

Type 5: In the initial state, the tri-dehydrogenated intermediate is binding to two edge Pt atoms of the stepped surface (Fig. 4.11e). The C–C bond distance is only 143 pm, manifesting a double bond order. In the transition state, the C–C bond stretches to 213 pm (Table 4.2). In



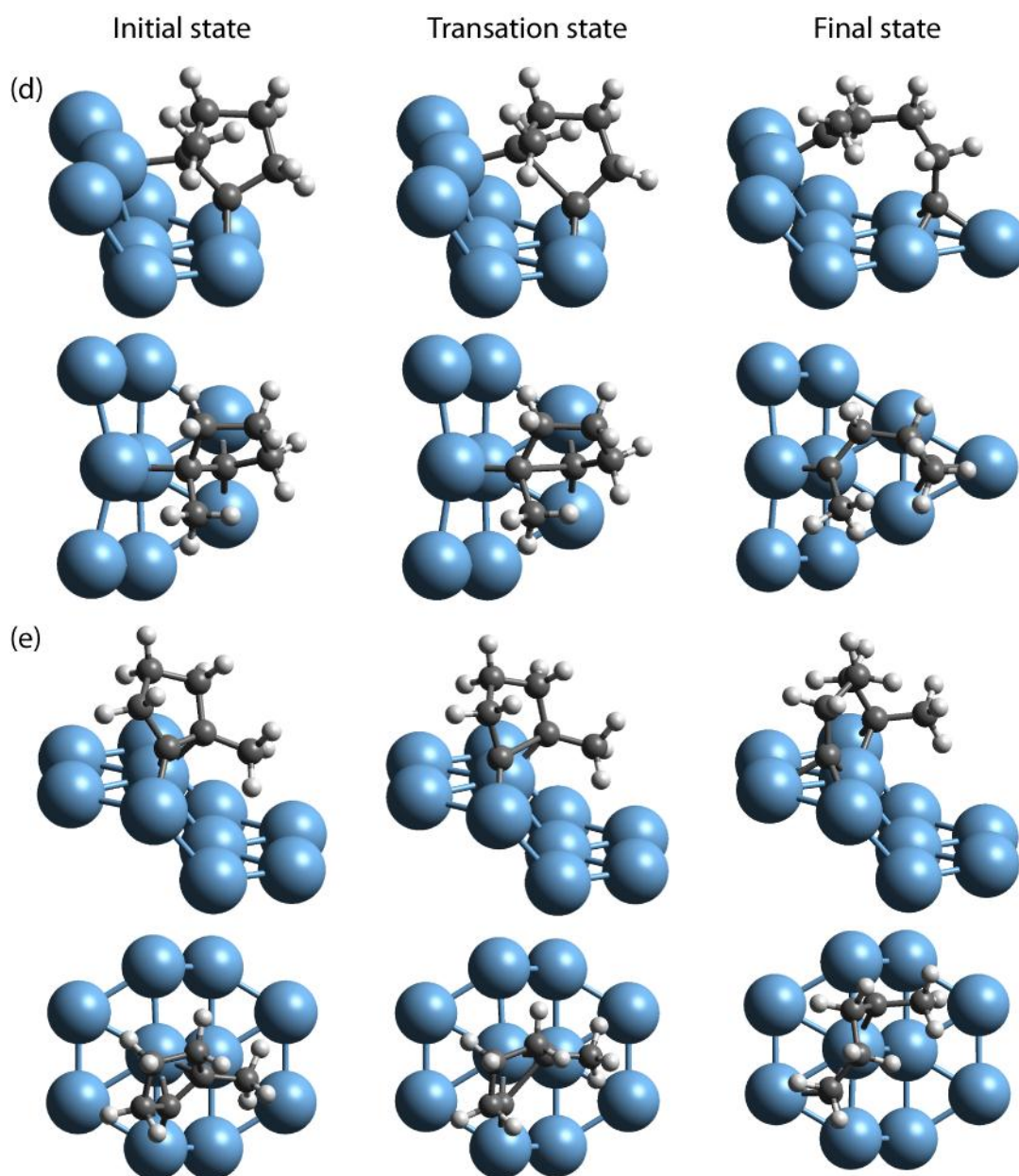


**Figure 4.11.** Optimized structures for the C–C bond breaking step at different reaction sites a) to e), corresponding to reaction pathways Type 1 to Type 5, respectively, on the way to *n*Hx over Pt(211).

the final state, the C–C bond breaks and the two terminal C atoms are binding to a hollow and a bridge site, respectively (Fig. 4.11e). This reaction is exothermic by  $17 \text{ kJ mol}^{-1}$  and has a very high barrier,  $167 \text{ kJ mol}^{-1}$  (Table 4.2).

*Summary of C-C bond breaking on the way to nHx on Pt(211).* Here I considered five different types of initial states for the C–C bond scission step on the way to *n*Hx. Three reaction paths, namely, Type 1, 3 and 4, were found to have low barriers of  $\sim 90 \text{ kJ mol}^{-1}$ , while the barriers of the other two paths, Type 2 and Type 5, are at least  $20 \text{ kJ mol}^{-1}$  higher

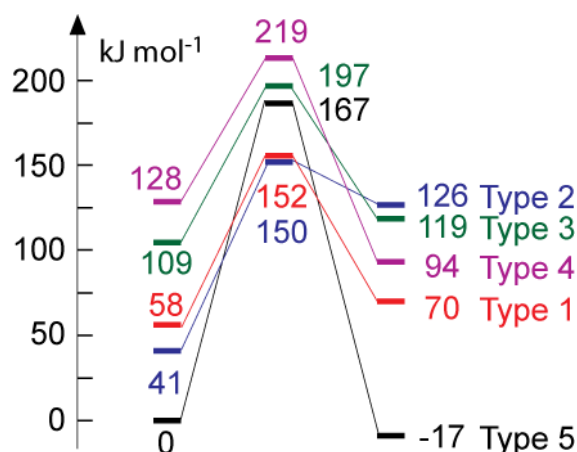


**Figure 4.12.** Energy profile of the C–C bond breaking step on the way to  $n\text{Hx}$  over Pt(211). The most stable initial state (Type 5) serves as energy reference.

than the barriers of the former three paths (Fig. 4.12, Table 4.2). Although the barriers of Type 3 and 4 paths are slightly lower than the barrier of Type 1 path by 3–6  $\text{kJ mol}^{-1}$ , the binding energies of their initial states are 50–70  $\text{kJ mol}^{-1}$  smaller than the corresponding binding energy on the latter pathway (Fig. 4.12, Table 4.2). Therefore, among all calculated reaction paths, Type 1 should be most favorable.

**C–C bond breaking on the reaction path to 2MP and 3MP.** Recall that the C–C scission over Pt(111) took place in the  $\alpha\alpha\beta\beta$ -tetra-dehydrogenated MCP derivatives 3-methylcyclopentyne and 4-methylcyclopentyne. On the stepped Pt(211) surface, however, in addition to the tetra-dehydrogenated  $\alpha\alpha\beta\beta$ -species, also tri-dehydrogenated  $\alpha\alpha\beta$ -intermediates 3-methyl-1-cyclopenten-1-yl and 4-methyl-1-cyclopenten-1-yl were considered to undergo a C–C cleavage on the way to 2MP and 3MP. Such a possibility was checked because, as shown above, a tri-dehydrogenated intermediate can also have a relatively low barrier (94  $\text{kJ mol}^{-1}$ ) for the C–C bond breaking step on Pt(211) to  $n\text{Hx}$ , which is notably lower than for the analogous reaction on the flat Pt(111) surface. The selection criteria for the choice of the initial states are explained at the beginning of Section 4.2.2 and will not be repeated here. I calculated in total three types of initial states, named as Type 1, 2 and 3 in the following, and for each type there are two reactions, on the way to 2MP and 3MP, respectively.

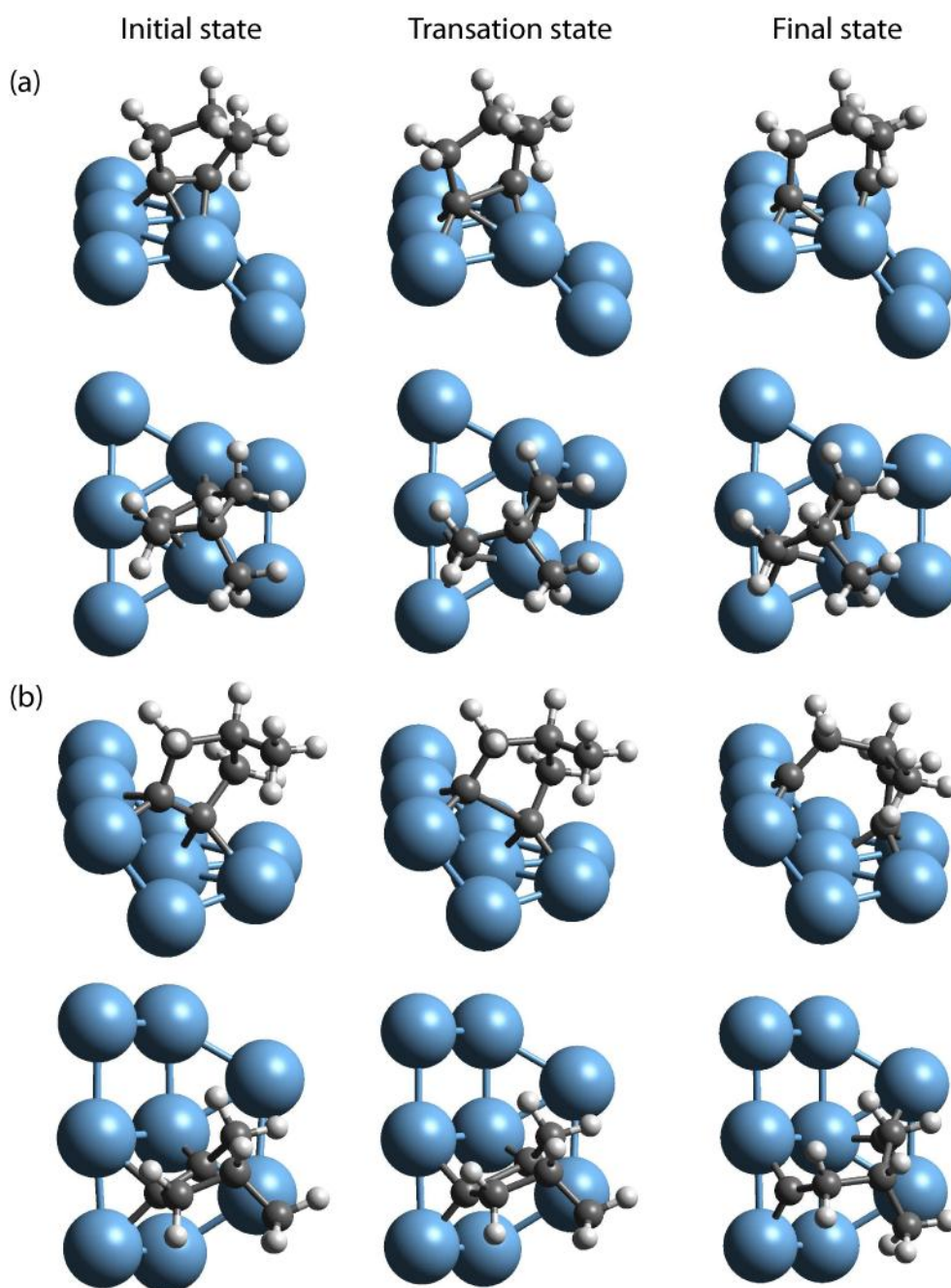


**Figure 4.13.** Optimized structures for C–C bond breaking steps from a tetra-dehydrogenated intermediate at different reaction sites a) Type 1 and b) Type 2 on the way to 3MP over Pt(211).

*Type 1 - Most favorable reaction pathways.* The initial states of the reactions toward 2MP and 3MP are tetra-dehydrogenated intermediates. The hydrocarbon adsorbs at a terrace edge hollow site in the same fashion as over Pt(111) (Fig. 4.13a). Unlike the reaction over Pt(111), the ring-opening can proceed via a direct C–C bond breaking without a preceding migration step. This difference can be attributed to the stronger bonding between the edge Pt

**Table 4.3:** Optimized geometries<sup>a</sup> (pm) and energy characteristics (kJ mol<sup>-1</sup>) of transition states of C-C bond breaking of MCP ring-opening over Pt(211) on the way to 3MP and 2MP.

		Initial state	C-C <sup>b</sup>	BE <sup>c</sup>	$\Delta E$ <sup>d</sup>	E <sub>a</sub> <sup>e</sup>
3MP	Type 1	tetra-adsorbed	191	499	40	102
	Type 2	tetra-adsorbed	222	440	-30	107
	Type 3	tri-adsorbed	211	295	24	111
2MP	Type 1	tetra-adsorbed	189	505	33	98
	Type 2	tetra-adsorbed	220	424	-61	97
	Type 3	tri-adsorbed	210	294	31	113

<sup>a</sup> A-B, distance between atoms A and B in the transition state. <sup>b</sup> C-C distance in the transition state of the bond to be cleaved. <sup>c</sup> Binding energy of the initial state. Note that the binding energy of the tri-dehydrogenated (tri-adsorbed) MCP over Pt(111) is 282 kJ mol<sup>-1</sup> and those of the tetra-dehydrogenated (tetra-adsorbed) MCPs on Pt(111) are 489–492 kJ mol<sup>-1</sup>. <sup>d</sup> Reaction energy. <sup>e</sup> Activation energy.

atom and the C atom, which prevents the migration of the adsorbed C atom on Pt(211). In the final state, this C atom is still adsorbed at the bridge site of the terrace edge in sp<sup>2</sup> hybridized fashion (Fig. 4.13a), similar to Type 1 path on the way to *n*Hx over Pt(211). This reaction step is strongly endothermic by 33–40 kJ mol<sup>-1</sup>. The calculated barrier heights on the way to 2MP and 3MP are 98 and 102 kJ mol<sup>-1</sup>, respectively, more than 20 kJ mol<sup>-1</sup> above the barrier of the corresponding step over Pt(111) (Tables 4.1 and 4.3).

*Types 2-3 - Alternative reaction pathways.* Type 2: The initial states of these reactions toward 2MP and 3MP are also tetra-dehydrogenated intermediates. The hydrocarbon adsorbs across the step with one C atom connecting to the edge Pt atoms and the other one binding to the lower terrace (Fig. 4.13b). In the transition states, the C-C bond stretches to 220–222 pm, 30 pm longer than in the transition states of Type 1 path (Table 4.3). In the final states, the two terminal C atoms adsorb at a hollow site on the terrace and a bridge site at the step edge (Fig. 4.13b). This reaction step is strongly exothermic by 30–61 kJ mol<sup>-1</sup>. The corresponding activation barriers are 97–107 kJ mol<sup>-1</sup>, close to barrier heights of Type 1 path (Table 4.3). However, the initial states of Type 2 reaction path are 60–80 kJ mol<sup>-1</sup> less stable than those of Type 1 path, indicating that Type 2 should not dominate at stepped surfaces.

Type 3: Recall that for Type 1 path to *n*Hx on Pt(211), a low barrier, 94 kJ mol<sup>-1</sup>, was calculated, which is 20 kJ mol<sup>-1</sup> lower than for the corresponding step on Pt(111). An

**Table 4.4:** Optimized geometries<sup>a</sup> (pm) and energy characteristics (kJ mol<sup>-1</sup>) of transition states of C-C bond breaking of MCP ring-opening on Pt(322) on the way to *n*Hx.

	Initial state	C-C <sup>b</sup>	BE <sup>c</sup>	ΔE <sup>d</sup>	E <sub>a</sub> <sup>e</sup>
Type 1	<i>αγ</i> -di-adsorbed	190	-329	-35	79
Type 2	<i>αγ</i> -di-adsorbed	234	-308	-5	122
Type 3	<i>αγ</i> -di-adsorbed	233	-311	-47	123
Type 4	<i>ααγ</i> -tri-adsorbed	238	-573	68	114
Type 5	<i>ααγ</i> -tri-adsorbed	223	-494	-147	85

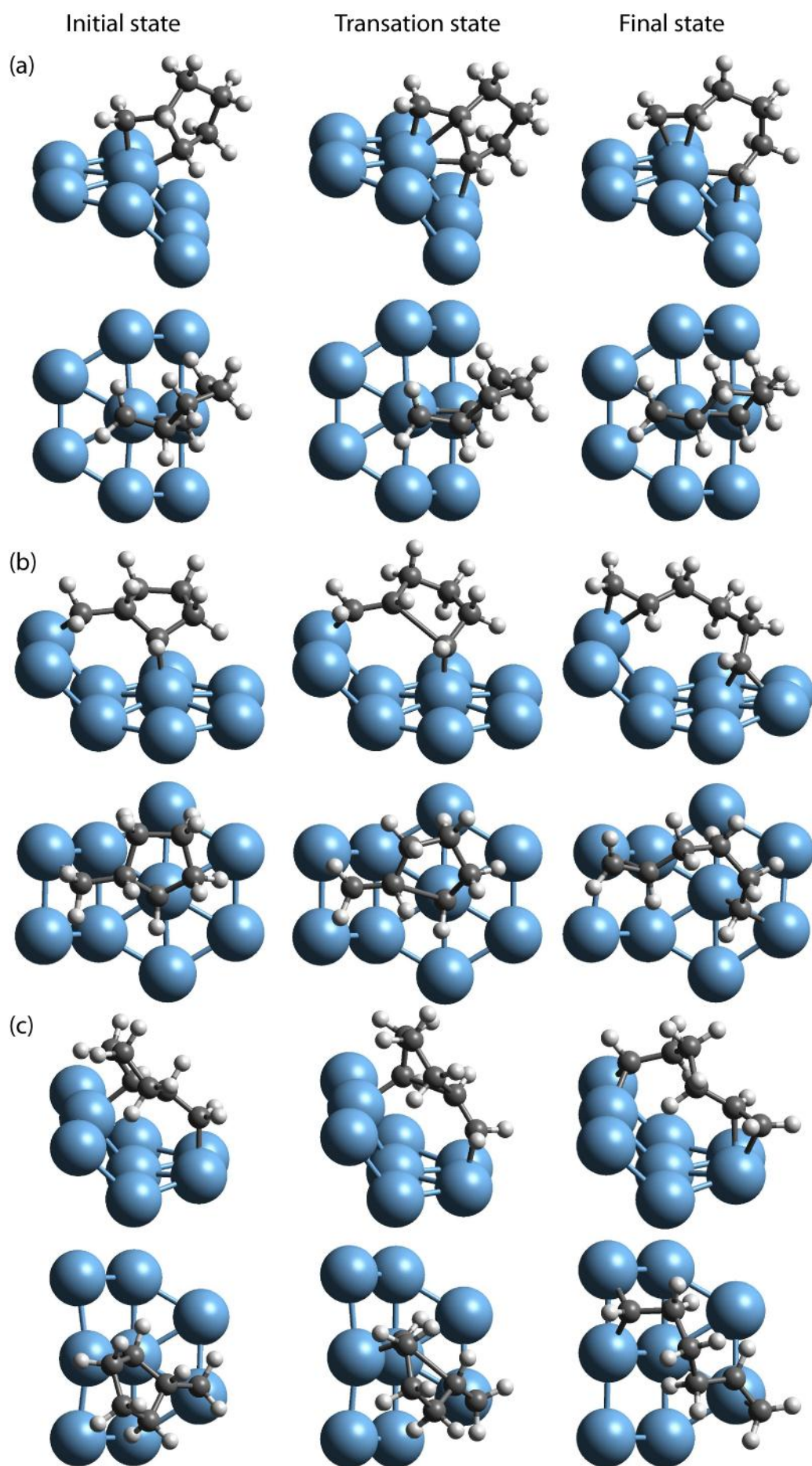
<sup>a</sup> A-B, distance between atoms A and B in the transition state. <sup>b</sup> C-C distance in the transition state of the bond to be cleaved. <sup>c</sup> Binding energy of the initial state. <sup>d</sup> Reaction energy. <sup>e</sup> Activation energy.

analogous ring-opening reaction, from *ααβ*-tri-dehydrogenated initial states, can also lead to 2MP or 3MP, when methyl group is attached to the corresponding C atoms (C3-C5) (similar to Fig. 4.11a, but with methyl group attached to C3, C4, or C5). The structural details of this reaction are very close to those of Type 1 C-C cleavage on the way to *n*Hx, and are not repeated here. Both reactions are endothermic by 24–31 kJ mol<sup>-1</sup>. Yet, the activation energies calculated for Type 3 path on the way to M2/M3 are 111–113 kJ mol<sup>-1</sup>. They are about 10 kJ mol<sup>-1</sup> higher than the barriers of Type 1 and 2 reaction paths, to 3MP and 2MP from *ααββ*-tetra-dehydrogenated intermediates (Table 4.3).

*Summary of C-C bond breaking on the way to 2MP and 3MP on Pt(211).* Here I considered three different types of initial states of the C-C bond scission step on the way to 2MP or 3MP. The C-C scission barriers of Type 1 and 2 paths, 97–107 kJ mol<sup>-1</sup>, are slightly lower than the barriers of Type 3 paths, 111–113 kJ mol<sup>-1</sup> (Table 4.3). Furthermore, the initial states of Type 1 C-C cleavage have 50–80 kJ mol<sup>-1</sup> larger binding energies than the corresponding initial states of Type 2 paths. Therefore, among all calculated reaction paths, Type 1 should be the most likely one.

### 4.2.3 Alternative reaction to form *n*Hx on small Pt particles

Finally, yet another mechanism for the ring opening of MCP shall be considered, via an *αγ*-di-adsorbed intermediate, Fig. 4.1(b). This pathway is based on suggestions by Gault and co-workers<sup>117</sup> and is sometimes referred to in the literature as “partially selective” or “metallocyclobutane” mechanism. The calculation was done using the Pt(322) surface as a



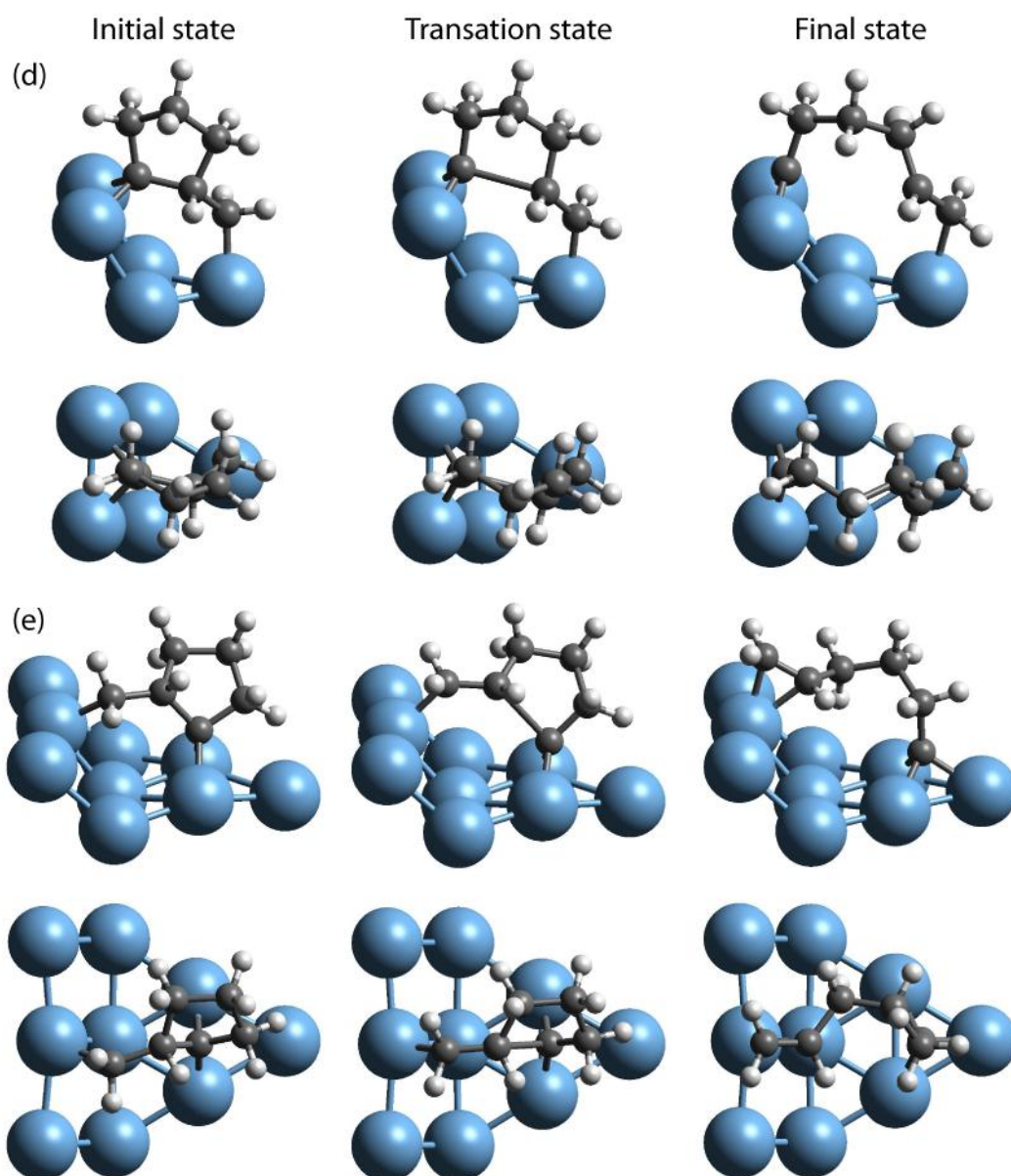


**Figure 4.14.** Optimized structures for the C–C bond breaking step from: *i*)  $\alpha\gamma$ -didehydrogenated intermediate (a)–(c), corresponding to Type 1–3, respectively; *ii*)  $\alpha\alpha\gamma$ -tri-dehydrogenated intermediate (d) and (e) on the way to  $nHx$ , corresponding to Type 4 and 5, respectively, over Pt(322).

model for small Pt particles. This surface has a step structure similar to Pt(211), but features wider terraces between two steps. The wider terraces help to avoid unrealistic intramolecular interactions between adsorbates in adjacent unit cells. Similar to the reaction scheme on Pt(211), only the C–C bond breaking step was considered in this thesis.

***C–C bond breaking in the reaction path to  $nHx$ .*** The initial state of this reaction is an  $\alpha\gamma$ -di-adsorbed or  $\alpha\alpha\gamma$ -tri-adsorbed metallocycle, where the methyl group participates in the

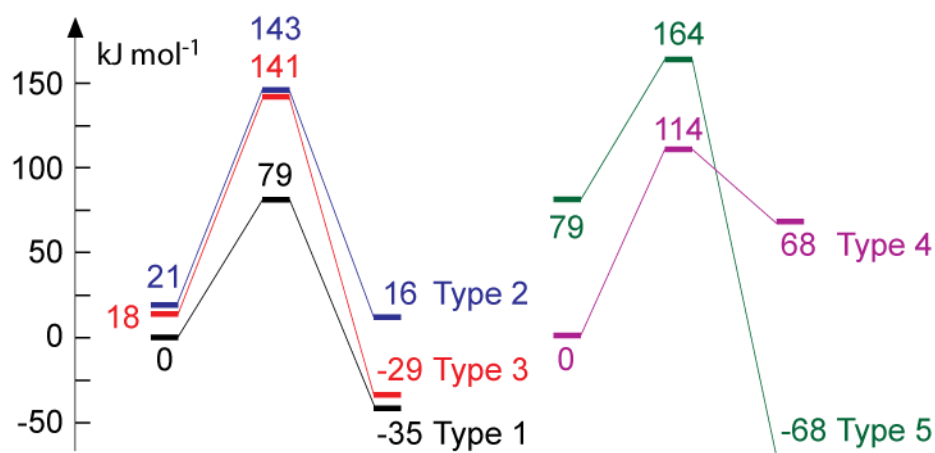


**Figure 4.15.** Energy profile of the C–C bond breaking step on the way to  $n\text{Hx}$  over Pt(322). The reference system is the most stable initial state of the didehydrogenated intermediate (Type 1) and tri-dehydrogenated intermediate (Type 4).

binding to the metal. The formation of both intermediates requires a dissociation of one H atom from the methyl group. Next, the C–CMe bond breaks selectively. Thus, only  $n\text{Hx}$  can be produced via this mechanism. Similar to the calculations on Pt(211), only the initial states in which the hydrocarbon adsorbate directly interacts with the edge Pt atoms are considered, as explained at the beginning of Section 4.2.2.

*Most favorite reaction pathway, Type 1.* The reaction starts from an  $\alpha\gamma$ -di-adsorbed intermediate. In the initial state, both chemisorbed C atoms, C1 and C6, bind to the same Pt atom at the step edge (Fig. 4.14a), with C–Pt bonds of 212–213 pm. The C1–C2 length is 154 pm; it stretches to 190 pm in the transition state (Table 4.4). The C2 atom forms a weak interaction with the step edge Pt atom, at 256 pm. This interaction becomes stronger in the final state, 222 pm, with both C2 and C6 bonding to one Pt atom (Fig. 4.14a). The C1 atom adsorbs at a bridge site on the step. The reaction is exothermic by  $35 \text{ kJ mol}^{-1}$  with a barrier as low as  $79 \text{ kJ mol}^{-1}$  (Table 4.4). This barrier is lower than the other calculated barriers (Table 4.4). Thus, it is the most favorable C–C breaking reaction path to form  $n\text{Hx}$  from  $\alpha\gamma$ -di-adsorbed or  $\alpha\alpha\gamma$ -tri-adsorbed intermediates over Pt(322).

*Type 2-5, Alternative pathways.* Type 2 and Type 3: These two reactions have very similar initial states. The di-dehydrogenated intermediates are bound to the surface via one C atom attaching to the edge of a step and another C atom adsorbing on the (111) terrace across the step (Fig. 4.14b and 4.14c). The only difference between these two initial states is the

position of the methylene group, which is either attached to the edge (Type 2) or to the terrace (Type 3). Both initial states are about  $20 \text{ kJ mol}^{-1}$  less stable than that of Type 1 (Figure 4.15). In the transition states, the C–C bond stretches to 233–234 pm (Table 4.4). At variance with the TS structure in Type 1, the C2 atom is still away from the metal surface, with the C2–Pt distance  $> 300 \text{ pm}$ , which indicates no stabilization of this unsaturated C center via an interaction with the Pt surface. In the final states, the C–C distance is increased to  $\geq 389 \text{ pm}$ , indicating a complete breaking of the C–C bond. Both reactions are exothermic by  $5 \text{ kJ mol}^{-1}$  and  $47 \text{ kJ mol}^{-1}$ , respectively. The activation energies are 122 and  $123 \text{ kJ mol}^{-1}$ , about  $40 \text{ kJ mol}^{-1}$  higher than the activation barrier of Type 1 path (Table 4.4).

Type 4 and Type 5: The initial states of these two reactions are tri-dehydrogenated  $\alpha\alpha\gamma$  intermediates. They have the same orientation of the adsorbates as in the initial states of Type 3 and 2 paths, respectively. The major difference to Type 3 and 2 paths, is that the last H atom on C1 is already dehydrogenated in Type 4 and 5 initial states, and C1 is attached at a bridge site either at an edge or on a terrace (Fig 4.14d and 4.14e). In the transition states, the C–C bond stretches to 223–238 pm (Table 4.4). These two reaction paths show different adsorption modes in the final state. In the final state of Type 4 path, C1 is bridge-bound at a step in  $sp^2$  hybridized fashion, C6 is singly adsorbed at a top site, while C2 is not interacting with the surface for sterical reasons, whereas in the final state of Type 5 path C1 adsorbs at a threefold site, as is typical for a strongly interacting carbynic center, and both C2 and C6 are  $\pi$ -adsorbed. Due to the lack of stabilization of C2 center by the Pt surface in the final state of Type 4 path, its binding energy is  $135 \text{ kJ mol}^{-1}$  smaller compared to the final state of Type 5 path (Fig. 4.15). Consequently, the reaction energy of Type 4 path is strongly endothermic by  $68 \text{ kJ mol}^{-1}$ , with a barrier at  $114 \text{ kJ mol}^{-1}$  (Table 4.4). In contrast, the barrier of Type 5 path is not very high,  $85 \text{ kJ mol}^{-1}$ , which is comparable to that of Type 1 path (Table 4.4). In addition, the final state of Type 5 path benefits from extra stability of the carbyne type terminal C1 atom, and the corresponding reaction is exothermic by  $147 \text{ kJ mol}^{-1}$ . However, the initial state of Type 5 path is  $79 \text{ kJ mol}^{-1}$  less stable than that of Type 4 path, indicating that the population of this initial state should be smaller than that of Type 4. Thus, Type 5 cleavage should not be important over Pt(322).

*Summary of C–C bond breaking on the way to  $nHx$  on Pt(322).* In this section I considered five different reaction paths either from  $\alpha\gamma$ -di-adsorbed or  $\alpha\alpha\gamma$ -tri-adsorbed intermediate. Two reaction paths have calculated barriers as low as  $\sim 80 \text{ kJ mol}^{-1}$ , namely,

Type 1 at  $79 \text{ kJ mol}^{-1}$  and Type 5 at  $85 \text{ kJ mol}^{-1}$ . However, the binding energy of the Type 5 initial state is  $80 \text{ kJ mol}^{-1}$  smaller than of Type 4 initial state, which indicates that the population of the former initial state should be low. On the other hand, among all the three  $\alpha\gamma$ -di-adsorbed initial states, the binding energy of Type 1 initial state is the largest. Note that the binding energy of  $\alpha\gamma$ -di-adsorbed and  $\alpha\alpha\gamma$ -tri-adsorbed initial states cannot directly be compared with each other. Therefore, Type 1 is likely the most favorable reaction path according to the results of current calculations.

#### 4.2.4 Selectivity of the ring-opening on single-crystal surfaces

The current section focuses on the reactions over two types of surfaces, flat Pt(111) and stepped Pt(211) and Pt(322). The calculations show that the activation energies of the hydrogenation / dehydrogenation reactions are always below  $90 \text{ kJ mol}^{-1}$ . Moreover, the position of the methyl group does not have a large influence on the activation energy of a particular hydrogenation / dehydrogenation step. However, the barriers of the C–C bond breaking steps vary from the lowest  $74 \text{ kJ mol}^{-1}$  to the highest  $\sim 125 \text{ kJ mol}^{-1}$ . In the following, I will try to rationalize the experimentally observed different selectivity of various Pt surfaces on the basis of the calculated barriers of the key elementary steps.

**Flat Pt(111) surface.** The calculated activation energy for the C–C bond breaking on the way to  $n\text{Hx}$  over the Pt(111) terraces is  $116 \text{ kJ mol}^{-1}$ . It is quite a bit higher than the barriers of the C–C bond breaking in the reaction path to 2MP and 3MP,  $74\text{--}75 \text{ kJ mol}^{-1}$  (Fig. 4.16a). In fact, the barrier for C–C cleavage on the way to  $n\text{Hx}$  over Pt(111) is expected to be rate determining because it is also higher than the activation energies of the hydrogenation and dehydrogenation reactions, which are less than  $89 \text{ kJ mol}^{-1}$ . Thus, the production of  $n\text{Hx}$  should be slow on Pt(111) due to the  $25 \text{ kJ mol}^{-1}$  higher barrier of the rate determining step, compared to the highest barriers on the way to 2MP and 3MP. Remarkably, this hypothesis was confirmed by single-crystal experiments. Garin et al. reported<sup>125</sup> the distribution of products 2MP, 3MP and  $n\text{Hx}$  on Pt(111) was  $0.6 : 0.3 : 0.1$  (Fig. 4.16b). Compared with the statistical ratio,  $2\text{MP} : 3\text{MP} : n\text{Hx} = 0.4 : 0.2 : 0.4$ , the formation of  $n\text{Hx}$  is clearly depressed. A study by Zaera et al.<sup>126</sup> also reported a similar distribution with slightly higher selectivity to  $n\text{Hx}$ ,  $2\text{MP} : 3\text{MP} : n\text{Hx} = 0.6 : 0.25 : 0.15$ .

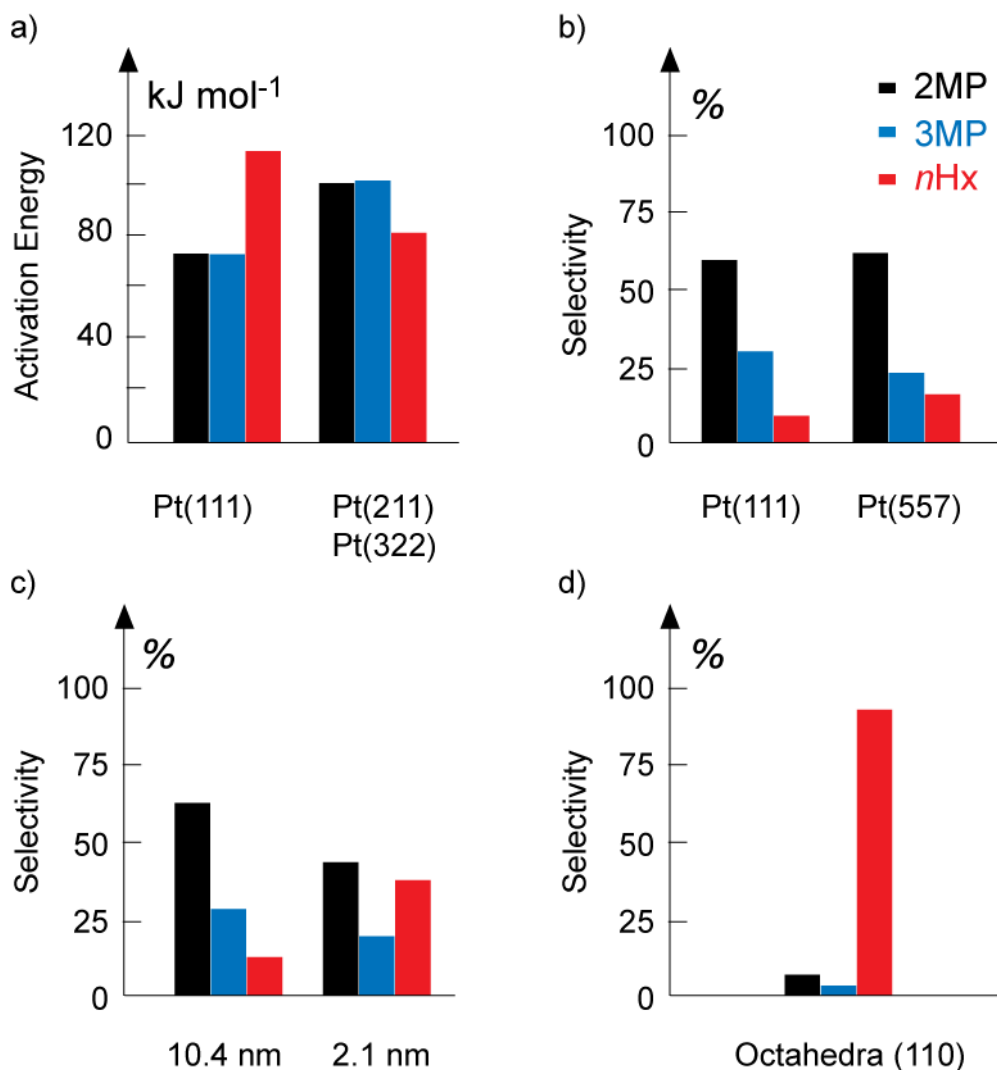


**Figure 4.16.** a) calculated barrier heights of the C–C bond breaking step on different Pt surfaces. b-d) experimental selectivity of the 2MP, 3MP and *n*Hx: b) catalyzed by single crystal (Ref 125); c) catalyzed by supported Pt particles with different size (Ref 124); d) catalyzed by the morphology controlled Pt particles (Ref 155).

**Stepped surfaces.** On stepped surfaces, the situation is reversed. The barriers of C–C bond breaking to form branched products over Pt(211), 102 kJ mol<sup>-1</sup> (2MP) and 98 kJ mol<sup>-1</sup> (3MP), are slightly higher than the barrier on the way to *n*Hx, 94 kJ mol<sup>-1</sup>. An even lower barrier, 79 kJ mol<sup>-1</sup>, was calculated over Pt(322) on the way to *n*Hx. If the highest barrier for the hydrogenation / dehydrogenation reactions over stepped Pt(211) and Pt(322) surfaces is assumed the same as over Pt(111) (~90 kJ mol<sup>-1</sup>), the barrier for the rate determining step is about 10 kJ mol<sup>-1</sup> higher on the way to branched 2MP or 3MP than that on the way to *n*Hx. Thus, the formation of the *n*Hx should be enhanced in this case. Indeed, the relative yield of

$n$ Hx increased from 0.1 on Pt(111) to 0.16 on Pt(557) in the experimental studies by Garin et al.<sup>125</sup> Note that the surfaces Pt(577), Pt(322) and Pt(211) have the same step structure with different terrace width which are 7, 5, and 3 rows wide, respectively. However, the selectivity towards 2MP and 3MP is still much higher than to  $n$ Hx. This is not surprising because 86% of the surface atoms of Pt(557) are on (111) terraces; thus, 2MP and 3MP are still preferentially produced over the terrace part of Pt(557). At variance with the above result, the enhanced production of  $n$ Hx was not observed by Zaera et al.<sup>126</sup> on the stepped surface Pt(557) surface. The difference to the observations of Garin et al.<sup>125</sup> may be rationalized by the lower  $H_2$  / MCP ratio used in the work of Zaera et al.<sup>126</sup> In the latter case, steps and other defects were blocked by carbonaceous deposits, as the authors confirmed by CO titration and Auger electron spectroscopy. Thus, carbon residues, which preferentially stick to undercoordinated surface sites,<sup>151,152</sup> were found to inhibit the formation of  $n$ Hx over the steps.

#### 4.2.5 Selectivity of ring-opening products on supported Pt particles

In industrially relevant catalytic systems, reactions are catalyzed by supported metal particles but not by surfaces of single crystals. An interesting observation coming from numerous experimental studies on MCP ring-opening was the correlation between the selectivity of ring-opening products and the supported Pt particle size.<sup>124</sup> One could expect that for large Pt particles, the surface area of the terrace facets, e.g. (111), is relatively large. Indeed, in a recent <sup>13</sup>CO-TPD study, Lundwall et al.<sup>153</sup> clearly showed that the sites on the terrace facets constitute more than 65% of all sites when Pt particles are larger than 4 nm. Thus, in the case of supported large Pt particles, a large net surface area of (111) terraces is responsible for the selective production of 2MP and 3MP in large amounts, while the production of  $n$ Hx is lower than the statistical ratio. When the size of Pt particles decreases, the fraction of step sites increases.<sup>154</sup> The preference of  $n$ Hx formation at stepped sites increases the selectivity towards  $n$ Hx on small Pt particles compared with the large ones.

The desired product of MCP ring-opening with high CN is  $n$ Hx. Decreasing of the particle size can help increase the selectivity towards  $n$ Hx. However, most of the previous experiments only achieved a selectivity as high as around 40%. According to the current calculations, a catalyst with a high fraction of step sites should dramatically increase the selectivity toward  $n$ Hx, due to a lower C–C bond breaking barrier to produce  $n$ Hx than the barriers to produce 2MP or 3MP at stepped sites. A recent study by Alayoglu et al.<sup>155</sup> succeeded in preparing Pt particles with controlled shape and size. The selectivity towards

*n*Hx in the ring-opening of MCP reached 90% when it was catalyzed by 6.3 nm octahedral Pt particles with (110) facet symmetry at about 220°C (Fig. 4.16d). Thus, a stepped structure indeed helps to increase the selectivity toward *n*Hx. However, one should keep in mind that the selectivity is also very sensitive to the reaction temperature on this kind of Pt particles, where the selectivity to *n*Hx drops steadily when the reaction temperature increases.<sup>155</sup>

### 4.3. Ring-opening reactions catalyzed by Rh, Ir and Pd

Aside from Pt, other noble metals, e.g. Rh and Ir, are capable to catalyze MCP ring-opening. Samoila et al.<sup>19</sup> studied five metal catalysts, Ir, Rh, Ru, Re and Pt, supported by alumina, and compared the selectivity and activity of these catalysts. At 573K, the activity of the tested catalysts followed the following trend from high to low: Ir > Rh > Ru > Re >> Pt. Although Pt showed the lowest activity, the selectivity to *n*Hx was highest among the metal catalysts considered.

In order to gain a deeper understanding of the MCP RO mechanisms on different metal catalysts, three additional transition metal catalysts M, M = Rh, Ir or Pd, were selected in this study. Similar to the calculations on Pt surfaces, the mechanism proposed in this part is based on the ideas of Gault et al.<sup>117, 123</sup> (Fig. 4.2). Our preferred mechanism requires deep dehydrogenation of the two chemisorbed C atoms in MCP, i.e. the dissociation of all H atoms connected to the two C atoms of the breaking C–C bond. Arguments supporting such a mechanism were given in Section 4.1.3. Thus, the branched 2MP and 3MP are formed through  $\alpha\alpha\beta\beta$ -tetra-dehydrogenated intermediates, while *n*Hx can only be formed via  $\alpha\alpha\beta$ -tri-dehydrogenated intermediate, due to the substituting methyl group.

In section 4.2, the calculated barriers for the same hydrogenation / dehydrogenation step on the way to the three RO products, 2MP, 3MP and *n*Hx, are very close to each other, within 10 kJ mol<sup>-1</sup>, indicating similar reaction rates for the corresponding hydrogenation / dehydrogenation steps. Moreover, compared to the barriers of the C–C bond breaking steps, the barriers of the hydrogenation / dehydrogenation reactions are in a lower energy range, under 90 kJ mol<sup>-1</sup> on Pt(111). Similarly low barriers were also reported on other metal surfaces by several previous theoretical studies<sup>64,65,73,144,145, 156</sup> for hydrogenation / dehydrogenation reactions analogous to those of the present thesis. For example, slightly higher barriers were reported for hydrogenation/dehydrogenation of hydrocarbons on Pd(111),<sup>64, 65, 144</sup> with most of them less than 100 kJ mol<sup>-1</sup>. Much lower

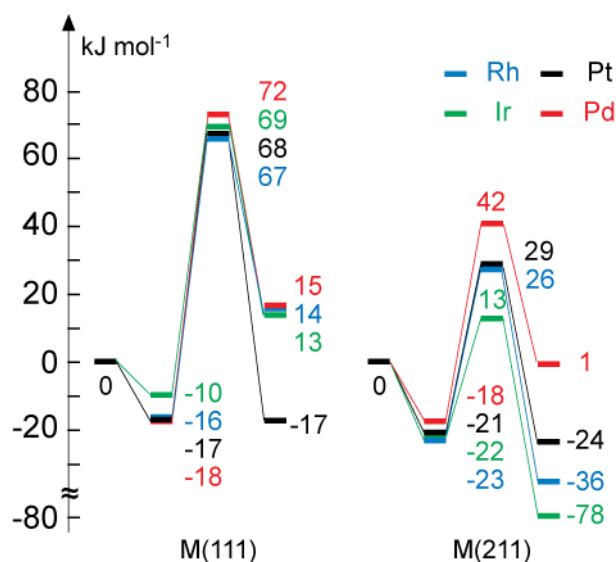


**Figure 4.17.** Energy profile of the first dehydrogenation step on the way to 3MP over M(111) and M(211). Energies are calculated relative to MCP in the gas phase and the clean 3×3 M(111) or 3×1 M(211) slab.

barriers,  $< 50 \text{ kJ mol}^{-1}$ , were reported<sup>156</sup> for analogous reactions over Rh(111). In this thesis, only the transition states of the first dehydrogenation step, which is the one with the highest dehydrogenation / hydrogenation barrier on Pt(111), were located on M(111) and M(211) surfaces. Underlying to this strategy is the assumption that the corresponding barriers are close to the highest barrier of hydrogenation / dehydrogenation reactions on each metal surfaces. The calculated C–C bond breaking barriers on Pt surfaces, which were demonstrated to be crucial for the relative selectivity of the three RO products in Section 4.2, vary from  $75 \text{ kJ mol}^{-1}$  to  $116 \text{ kJ mol}^{-1}$ . In the current section, the C–C bond breaking steps on M(111) and M(211) are investigated. In the following, M denotes the three metals under consideration, Pd, Rh and Ir. Moreover, the calculated barriers of individual steps on the pathway to 2MP are very close to the ones on the pathway to 3MP, and the reaction to 2MP is not calculated in this section.

### 4.3.1 First dehydrogenation reaction (D1)

**Dehydrogenation over M(111).** The geometries of the hydrocarbon intermediate during the reaction are quite similar on all four considered M(111) surfaces including Pt(111), the latter has been discussed in Section 4.2 [see Fig. 4.3 for the corresponding geometries on Pt(111)]. Thus, the structure details is repeated here. This dehydrogenation step on the way to

3MP is endothermic by 23–35 kJ mol<sup>-1</sup> on M(111) (Table 4.5), while it is nearly thermoneutral on Pt(111) (Table 4.1). Such a difference might be explained by a slightly different adsorption site of the co-adsorbed H in the final state on Pt(111). In the latter case, the H atom does not experience a direct bonding interaction with the Pt atom that binds to the hydrocarbon, which reduces the repulsion between the adsorbed H and the hydrocarbon and stabilizes the structure compared to the corresponding final states on the other three metals. Nevertheless, since the diffusion barrier of H atoms on the M(111) surfaces is low (~10 kJ mol<sup>-1</sup>),<sup>147,157,158</sup> a more stable final state can be formed after the diffusion of the H atom to one of the other empty sites away from the co-adsorbed hydrocarbon ring. The calculated barriers are in a narrow range on all M(111) surfaces including Pt(111), 79–92 kJ mol<sup>-1</sup> (Table 4.1 and Table 4.5). All barrier heights differ at most by 4 kJ mol<sup>-1</sup> between in the reaction path to 3MP and to *n*Hx (Table 4.5).

**Dehydrogenation over M(211).** The results of calculations summarized above show that the position of the methyl group does not strongly affect the reaction energies and barriers on M(111). Hence, on the stepped M(211) surfaces, the current study focused on only one of the two reactions, with the methyl group at C3. In the initial states, MCP is physically adsorbed at the step edge, with H–M bond length at 179–201 pm. This distance is shorter than on M(111), due to a stronger interaction of the unsaturated edge metal atoms with the dissociating H atom. The transition states are also similar to those on M(111). The reactive C atom moves towards the metal atom on the step edge, forming a new C–M bond at 222–233 pm. The dissociating H atom is pushed in the direction of a neighbor metal atom at the edge. The final state on Pd(211) is similar to that on Pt(211), with the hydrocarbon adsorbed at an edge top site with a single C–Pd bond at 209 pm. However, on the other two stepped surfaces, Rh(211) and Ir(211), the dehydrogenated MCP is adsorbed at the edge in a bridge fashion, forming two asymmetric C–M contacts at 210–213 pm and 239–240 pm, respectively. The remaining C1–H bond also bends towards the surface, forming a weak interaction of H with an edge metal atom, at 177–183 pm. At the same time, these C–H bond elongate to 117–123 pm. Note that the bridge-type adsorption was also reported for another monoradical hydrocarbon species (CH<sub>3</sub>) on Rh(211).<sup>159</sup> Energetically, the reaction is endothermic by 26 kJ mol<sup>-1</sup> on Pd(211) and exothermic by 13–56 kJ mol<sup>-1</sup> on Rh(111) and Ir(211). The calculated activation energies on M(211) surfaces are in the range of 35–60 kJ mol<sup>-1</sup>, which is 30–35 kJ mol<sup>-1</sup> lower than the values on M(111) (Table 4.5).

**Table 4.5:** Optimized geometries<sup>a</sup> (pm) and energy characteristics (kJ mol<sup>-1</sup>) for transition states of the first dehydrogenation step of the MCP ring-opening on the way to *n*Hx over M(111) and M(211) (M = Rh, Ir and Pd).

Final Product Surface	3MP		<i>n</i> Hx	
	111	211	111	
Pt	C-H <sup>b</sup>	148	154	148
	H-M <sup>b</sup>	167, 214	168, 207	167, 213
	DE <sup>c</sup>	0	-3	0
	E <sub>a</sub> <sup>d</sup>	85	50	89
Rh	C-H <sup>b</sup>	152	161	151
	H-M <sup>b</sup>	166, 200	166, 194	166, 201
	DE <sup>c</sup>	30	-13	26
	E <sub>a</sub> <sup>d</sup>	83	49	81
Ir	C-H <sup>b</sup>	148	153	149
	H-M <sup>b</sup>	167, 214	169, 211	167, 214
	DE <sup>c</sup>	23	-56	24
	E <sub>a</sub> <sup>d</sup>	79	35	81
Pd	C-H <sup>b</sup>	155	166	155
	H-M <sup>b</sup>	168, 192	169, 182	168, 192
	DE <sup>c</sup>	33	26	35
	E <sub>a</sub> <sup>d</sup>	90	68	92

<sup>a</sup> A–B, distance between atoms A and B in the transition state. <sup>b</sup> Bonds that are breaking/forming during a reaction. <sup>c</sup> Reaction energy. <sup>d</sup> Activation energy.

### 4.3.2 C–C bond breaking reactions

After four or three dehydrogenation reactions, two types of intermediates are formed over metal surfaces: (1)  $\alpha\alpha\beta\beta$ -tetra-adsorbed 3-methylcyclopentyne and 4-methylcyclopentyne and (2)  $\alpha\alpha\beta$ -tri-adsorbed 2-methyl-1-cyclopenten-1-yl. The former intermediates are going to convert to branched 2MP and 3MP, respectively, while the latter will ultimately convert to *n*Hx. In this section, I will separately discuss the C–C bond breaking reactions of the  $\alpha\alpha\beta\beta$ -tetra-adsorbed (tetra-dehydrogenated, on the pathway to 3MP) intermediate and of the  $\alpha\alpha\beta$ -tri-adsorbed (tri-dehydrogenated, on the pathway to *n*Hx) intermediate on different surfaces.

**Table 4.6:** Optimized geometries<sup>a</sup> (pm) and energy characteristics (kJ mol<sup>-1</sup>) for transition states of the migration and C–C scission steps of MCP ring-opening on the paths to 3MP or *n*Hx over M(111) and M(211) (M = Rh, Ir and Pd).

Final Product	Reaction step <sup>b</sup>	Surface	Pd			Rh			Ir		
			C–C <sup>c</sup>	$\Delta E^d$	$E_a^e$	C–C <sup>c</sup>	$\Delta E^d$	$E_a^e$	C–C <sup>c</sup>	$\Delta E^d$	$E_a^e$
3MP	Migration	111	142	11	14	143	2	11	147	23	41
	Migration	211	142	3	5	144	19	22	150	66	66
	CC (IS: $\mu$ -bridge)	111	196	50	59	183	5	16	175	-20	17
	CC (IS: $\mu$ -bridge)	211	201	76	84	187	14	27	181	-7	11
	CC (IS: $\parallel$ -bridge)	211							183	15	89
<i>n</i> Hx	CC	111	219	4	134	195	-49	70	190	-52	62
	CC	211	216	58	119	196	-7	59	190	-39	38

<sup>a</sup> A–B, distance between atoms A and B in the transition state. <sup>b</sup> CC stands for the C–C bond breaking step <sup>c</sup> C–C distance in the transition state of the bond to be cleaved in the C–C bond breaking step. <sup>d</sup> Reaction energy. <sup>e</sup> Activation energy.

**C–C bond breaking on the reaction pathway to 3MP over M(111).** As discussed above for the C–C bond breaking step on Pt(111), an additional migration step was introduced after the dehydrogenation reactions prior to the actual C–C cleavage because the direct C–C bond breaking in the tetra-dehydrogenated intermediate adsorbed in a parallel-bridge mode (the most stable adsorption mode; see below) passes through a second-order transition state. In this part of the thesis, the migration step is also considered on other M(111) surfaces.

After the four initial dehydrogenation reactions, the ring structures are adsorbed over a threefold hollow site with one metal atom forming bonds to both C atoms and the other two metal atoms forming one C–M bond each. This adsorption arrangement shall be denoted as  $\parallel$ -bridge mode. In the initial state, the ring backbone is almost normal to the surface. The C–C distance is only 140–142 pm, indicating a higher bond order than a single C–C bond. In the transition states (Fig. 4.18), the structures start to rotate about the surface normal passing through one of the metal atoms of the binding threefold site (a central M atom in the structural fragments of Fig. 4.18) and move in the direction of an adjacent threefold site. On Rh(111) and Pd(111), the transition-state structure with the two C atoms still sharing the same hollow site is closer to the initial state, whereas the transition structure on Ir(111) and Pt(111) with the two C atoms occupying neighbor hollow sites is more product-like. The C–C bond length in contact with the surface slightly increases to 142–147 pm in the transition state. During the

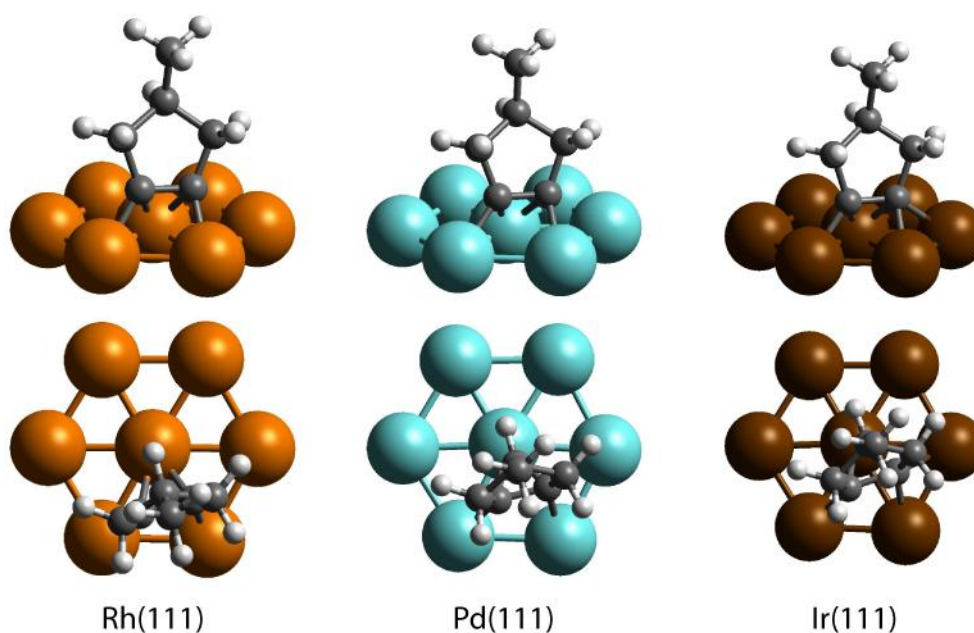


**Figure 4.18.** Optimized transition state structures for the migration step of the tetra-dehydrogenated intermediate on the way to 3MP over M(111).

migration step, the whole structure of the adsorbate rotates by  $\sim 30^\circ$  about the surface normal and shifts in the direction of the neighbor threefold site so that at the new location two C atoms occupy two adjacent threefold hollow sites. The resulting adsorption geometry is referred to as  $\mu$ -bridge mode. There, the C–C bond further elongates to 143–153 pm. This rearrangement is nearly thermoneutral over Rh(111) and slightly endothermic on Pd(111), by  $11 \text{ kJ mol}^{-1}$ , and Ir(111), by  $23 \text{ kJ mol}^{-1}$ . Lower activation energies are calculated for the metals of the fifth period (Pd and Rh,  $11\text{--}14 \text{ kJ mol}^{-1}$ ), while the activation energies are notably higher for the sixth-period metals (Pt and Ir,  $41\text{--}61 \text{ kJ mol}^{-1}$ ). Moreover, an extremely low reverse barrier,  $3 \text{ kJ mol}^{-1}$ , is found on Pd(111), indicating that the  $\mu$ -bridge mode is meta-stable, similarly to the situation on Pt(111).

After the migration step, the two C atoms in contact with the metal adsorb at two adjacent threefold hollow sites. In the transition states of the C–C scission, the two C atoms move away from each other. The C–C distance increases to 175–196 pm. In the final states, the C–C distance further increases to 224–235 pm. The barriers of this bond-breaking step are very low on Rh(111) and Ir(111), less than  $20 \text{ kJ mol}^{-1}$ . The reaction over Pd(111) has a higher barrier,  $59 \text{ kJ mol}^{-1}$ . Moreover, on Pd(111), the reverse barrier of the preceding migration step is as low as  $3 \text{ kJ mol}^{-1}$ . Thus, the total barrier should be calculated relative to

the most stable configuration of the tetra-adsorbed cyclic species, which is the  $\parallel$ -bridge mode. Hence, the overall barrier becomes  $70 \text{ kJ mol}^{-1}$  on Pd(111).

***C–C bond breaking on the reaction pathway to 3MP over M(211).*** A stepped surface offers more possibilities for accommodating a hydrocarbon at terrace or edge sites than the flat M(111) surface. For example, in the case of a reaction on Pt(211), three initial states for C–C bond breaking were discussed in Section 4.2. The reaction with the lowest activation barrier on Pt(211), which proceeds at a terrace hollow site close to the step edge, was chosen as the representative reaction for the current comparative study of ring-opening on M(211). Here, my working assumption is that the same path should be energetically most favorable on the rest of the studied M(211) surfaces.

The reaction path on Ir(211) is similar to that on Pt(211) discussed in Section 4.2 and illustrated in Fig. 4.11a. In the initial state of this reaction, the tetra-dehydrogenated intermediate is adsorbed in  $\parallel$ -bridge fashion at a hollow site close to the step edge. In the transition state, the C–C bond stretches to 183 pm, while one of the C atoms moves in the direction of the step edge. On Ir(211), like on Pt(211), direct C–C bond breaking, without a preceding migration step, takes place, likely due to the strong binding between the hydrocarbon and the unsaturated edge Ir (or Pt) atoms. Indeed, in the transition and final states of this reaction, the terminal C atom of carbyne type is adsorbed at a step edge site (Fig. 4.19a) rather than at a threefold hollow site as in the most stable adsorption mode on M(111).

Alternatively, the C–C bond breaking on Ir(211) can also occur after a migration step, which is similar to the reaction path over M(111) surfaces. Moreover, for the fifth-period elements (Rh and Pd), the migration step is necessary because the  $\parallel$ -bridge adsorbed intermediates cannot directly undergo C–C bond breaking. The geometries along the reaction pathway on Rh(211), Ir(211) and Pd(211) are similar to those on M(111) surfaces and will not be discussed in detail here. The obtained activation barriers of this reaction are not very high for the fifth-period elements,  $22 \text{ kJ mol}^{-1}$  on Rh(211) and  $5 \text{ kJ mol}^{-1}$  on Pd(211). Both reactions are slightly endothermic, by  $3\text{--}19 \text{ kJ mol}^{-1}$ . However, the reaction over Ir(211) is strongly endothermic by  $66 \text{ kJ mol}^{-1}$ , with no barrier for the reverse reaction.

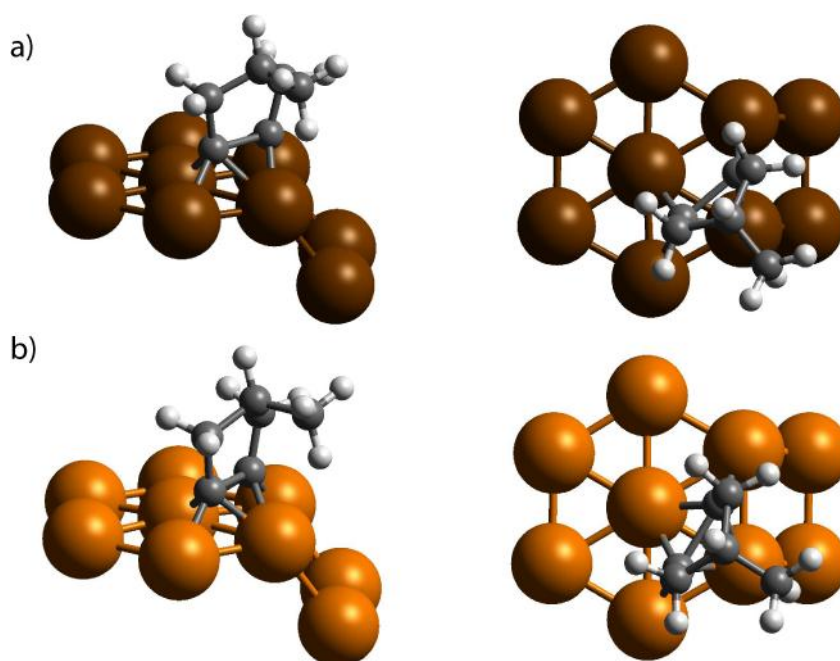


**Figure 4.19.** Optimized transition state structures for the C–C bond breaking step of the tetra-dehydrogenated intermediate on the way to 3MP over M(211): a) C–C bond breaking from the ||-bridge adsorbed intermediate on Ir(211); b) C–C bond breaking from the  $\mu$ -bridge adsorbed intermediate on Rh(211).

After the migration step, the C–C bond is broken on Rh(211), Ir(211) and Pd(211). In the transition states of the C–C cleavage, the two C atoms are adsorbed at two adjacent hollow sites, with the C–C bond elongated to 181–201 pm (Fig. 4.19b). In the final states, the adsorption mode of the intermediate is nearly the same as in the corresponding transition states, only with the longer C–C distance ( $>225$  pm). Energetically, this reaction step is endothermic by 14–76 kJ mol<sup>-1</sup> on fifth-period metals, whereas it is 7 kJ mol<sup>-1</sup> exothermic on Ir(211). The barrier heights are 27 kJ mol<sup>-1</sup> on Rh(211), 11 kJ mol<sup>-1</sup> on Ir(211), and 84 kJ mol<sup>-1</sup> on Pd(211). However, due to the 0–3 kJ mol<sup>-1</sup> reverse barrier of the preceding migration step on Rh(211) and Ir(211), the overall barrier for the C–C breaking step should be calculated relative to the most stable intermediate, the ||-bridge adsorbed one. Thus, the overall barriers are 46 kJ mol<sup>-1</sup> on Rh(211) and 77 kJ mol<sup>-1</sup> on Ir(211).

**C–C bond breaking on the reaction pathway to nHx over M(111).** The initial states of this reaction step are the tri-dehydrogenated MCP derivatives, with the methyl group attached at C2 [same as shown in Fig. 4.7 for Pt(111)]. The adsorbates are attached to the surface in  $\mu_3\text{-}\eta^2$  fashion. The C–C bond in the initial state is in the range of 148–151 pm. In the

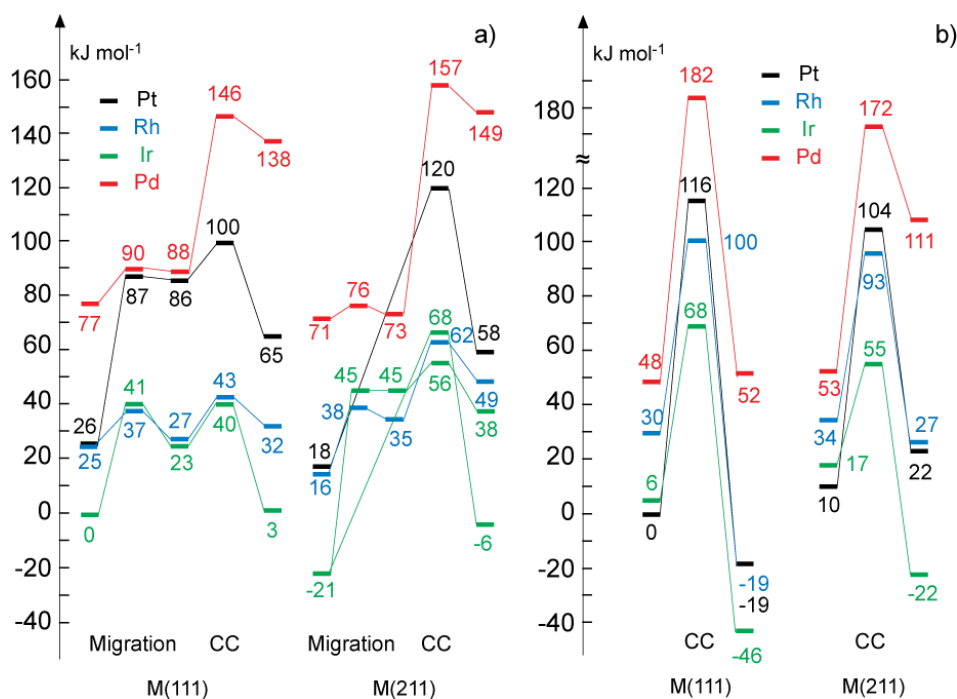


**Figure 4.20.** Energy profile of a) migration step and C–C bond breaking step on the way to 3MP over M(111) and M(211); b) C–C bond breaking step on the way to  $n\text{Hx}$  over M(111) and M(211). The reference system is the most stable adsorption mode of a) tetra-dehydrogenated intermediate on Ir(111); b) tri-dehydrogenated intermediate on Pt(111).

transition states, the terminal atom C2, with the methyl group attached to it, moves to a top site, while the other terminal carbon C1 moves slightly toward the center of the threefold hollow site initially shared by both C1 and C2. The C–C bond stretches to 190–219 pm in the transition states. In the final states, C2 moves further across a top site, forming two C–Pt bonds at an adjacent bridge site, whereas C1 remains at the threefold hollow site that initially hosted both C atoms. The C–C distance increases to 280–288 pm in the final state. This reaction is nearly thermoneutral on Pd(111) and is exothermic by  $\sim 50 \text{ kJ mol}^{-1}$  on Ir(111) and Rh(111). The highest activation energy for this reaction is obtained on Pd(111) at  $134 \text{ kJ mol}^{-1}$ . In the case of Rh(111) and Ir(111), the barriers are much lower, 70 and  $62 \text{ kJ mol}^{-1}$ , respectively.

**C–C bond breaking on the reaction pathway to  $n\text{Hx}$  over M(211).** The initial states of this reaction are similar to those on M(111). The adsorbate is attached in  $\mu_3\text{-}\eta^2$  fashion at a hollow site close to the terrace edge [same as shown in Fig. 4.11a for Pt(211)]. The C2 atom, with the attached methyl group, forms one C–Pt bond with the metal atom at the step edge of

the surface. The C–C bond length is calculated at 148–152 pm in the initial states. In the transition states, the C–C bond length stretches to 190–216 pm. In the final states, the two C terminals move farther away from each other, but the terminal C2 center holding the methyl group remains adsorbed at a top site of the terrace edge. The C–C distance increases to 280–288 pm. The reaction is strongly endothermic, by 58 kJ mol<sup>-1</sup>, on Pd(211) and has a high activation barrier of 119 kJ mol<sup>-1</sup>. On Rh(211) and Ir(211), this reaction step is exothermic by 7–39 kJ mol<sup>-1</sup>, with relatively low barriers at 59 and 38 kJ mol<sup>-1</sup>, respectively.

### 4.3.3 Activity on Pt, Pd, Ir, Rh surfaces

In general, there are two types of bond activation processes involved in the MCP conversion, C–H and C–C bond activation. All metals considered are experimentally shown to be active for the MCP ring-opening, which demonstrates that they can efficiently activate C–H and C–C bonds. In the following sections, the catalytic activity for the cleavage of these two types of bonds will be discussed separately.

**C–H activation.** On the selected metal surfaces, C–H bonds can easily be activated. For example, near room temperature, ethylene can easily convert to ethylidyne on Pt(111) via a series of hydrogenation / dehydrogenation reactions as discussed in Chapter 3. A similar behavior is also observed over Rh(111),<sup>55</sup> Pd(111),<sup>56</sup> and Ir(111).<sup>57</sup> In the current thesis, the loss of the first hydrogen atom by MCP was calculated on all selected surfaces. The obtained barriers of this reaction step on M(111) surfaces are not very high, in the range of 79–90 kJ mol<sup>-1</sup>. The barriers on different metals increase in the following order: Ir(111) < Rh(111) < Pt(111) < Pd(111), which is the same as the computationally predicted order of decreasing activity for methane dehydrogenation,<sup>160</sup> and is also consistent with the experimentally observed formation temperature of ethylidyne on these metal surfaces, Ir(111) at 180 K,<sup>57</sup> Rh(111) at 190 K,<sup>161</sup> Pt(111) at 250 K,<sup>9</sup> and Pd(111) at 300 K.<sup>162</sup>

On the stepped M(211) surfaces, the activation barriers for MCP dehydrogenation are calculated in the range from the lowest 35 kJ mol<sup>-1</sup> on Ir(211) to the highest 60 kJ mol<sup>-1</sup> on Pd(211). Compared to the same reaction on the M(111) surfaces, the barriers decrease by about 30 kJ mol<sup>-1</sup> on the step M(211) surfaces. Such decreasing of the dehydrogenation barrier at stepped surfaces was also reported by recent computational studies on the dehydrogenation of methane over Rh surfaces<sup>159</sup> and dehydrogenation of propane<sup>145</sup> or ethane<sup>163</sup> over Pt surfaces. Due to the structural similarity between the transition state and the

final state, this reaction passes through a “late” transition state. On the basis of the Brønsted–Evans–Polanyi (BEP) principle,<sup>164</sup> a “late” transition state leads to a strong correlation of the activation energy to the adsorption energy of the final state: the more stable the final state, the lower the activation energy of the reaction. On the M(211) surface, dehydrogenated MCP binds to an edge metal atom, with the binding energy that is 7–91 kJ mol<sup>-1</sup> stronger than on the planar M(111) surface, due to the higher uncoordinated nature of the edge atoms on M(211). Thus, the corresponding activation energies are lower on the M(211) surfaces.

*Adsorption site change (migration) of the tetra-dehydrogenated intermediate.* A change of an adsorption site (a migration step) is needed before the C–C bond breaking step of the tetra-dehydrogenated intermediate on M(111). During the reaction, the adsorption mode of the tetra-dehydrogenated intermediate changes from ||-bridge to  $\mu$ -bridge. Simultaneously, the C–C bond elongates by 3–11 pm, which is induced by the interaction between the metal s orbital and the  $\pi^*$  orbital of the C–C bond in the  $\mu$ -bridge mode.<sup>149</sup> This elongation facilitates the following C–C bond breaking.

The intermediates adsorbed in a  $\mu$ -bridge mode are less stable than the ||-bridge adsorbed ones. On Pd(111), Ir(111) and Rh(111), the energy difference between these two adsorption modes is 2–23 kJ mol<sup>-1</sup>. However, on Pt(111) the adsorption energy of the  $\mu$ -bridge adsorbed intermediate is significantly lower than that of the ||-bridge structure, by 60 kJ mol<sup>-1</sup>; at the same time, the barrier for the conversion from the  $\mu$ -bridge to ||-bridge mode is only 1 kJ mol<sup>-1</sup>. A similar behavior was also observed for the adsorption of acetylene, which is only stable in the ||-bridge adsorption mode on Pt(111).<sup>149</sup>

The activation energies for the conversion from the ||-bridge to  $\mu$ -bridge adsorption mode lie between 11 kJ mol<sup>-1</sup> and 61 kJ mol<sup>-1</sup>. On the investigated M(111) surfaces, the barriers increase in the following order: Rh(111) < Pd(111) < Ir(111) < Pt(111). The reaction on Pt(111) has the highest barrier due to the most unstable final state.

The  $\mu$ -bridge adsorbed tetra-dehydrogenated intermediate is unstable on Pt(211) or meta-stable with < 0.5 kJ mol<sup>-1</sup> barrier to ||-bridge mode on Ir(211), which might be due to a stronger binding between the C center and the step-edge metal atoms than on the corresponding (111) surfaces. This strong interaction has the consequence that the carbyne type C atom prefers to adsorb at a step-bridge site (||-bridge mode) rather than at a 3-fold

hollow site ( $\mu$ -bridge). Indeed, in the final state of the following C–C scission reaction, the terminal C atom of a carbyne type is adsorbed at a step-bridge site on the two considered stepped surfaces rather than at a 3-fold hollow site, which is the preferred adsorption mode on M(111).

**C–C activation.** Unlike the barriers of hydrogenation / dehydrogenation reactions, the barriers for the C–C bond breaking steps vary strongly from 15 kJ mol<sup>-1</sup> to 134 kJ mol<sup>-1</sup>. The large scatter of the barrier heights for C–C cleavage might be caused by more diverse structures of the transition states, whereas the hydrogenation / dehydrogenation reactions always exhibit similar transition structures with the typical C–H–Pt three member ring motif which leads to the fluctuations of the activation energies in a narrow range.

Two types of C–C bond breaking reactions were considered in this thesis: the reactions from tri-dehydrogenated and from tetra-dehydrogenated intermediates. In general, ring cleavage of the former was calculated to have a higher barrier compared with the analogous reaction of the latter on M(111). This can be rationalized by a more stabilized transition state for the ring-opening of a tetra-dehydrogenated intermediate or, in other words, by a flatter potential energy surface. In the initial state of this reaction, which on M(111) proceeds from the  $\mu$ -bridge adsorbed intermediate, the hydrocarbon ring is attached to two adjacent three-fold hollow sites, with each of the two binding C atoms attached to one hollow site. The C–C bond length in the initial state is around 150 pm. In the transition states, these two C atoms slightly move away from each other toward the respective centers of the binding hollow sites by 10–20 pm. Therefore, in the initial and transition states of the ring-opening, the bonding interactions between the C and surface Pt atoms should be similar due to the similar adsorption mode of the C centers. Moreover, the hollow site is the most stable site for adsorption of a carbyne species on M(111) surfaces. In contrast, the C–C bond breaking of a tri-dehydrogenated intermediate passes via a transition state where one of the reactive C atoms moves to a top site, which is not the most stable one (bridge site) for a carbene species. In addition, the displacements of the reacting C atoms along the whole transformation from an initial state to a final state are much larger in this case than during the C–C breaking in tetra-dehydrogenated intermediates. In the latter reaction, the C–C distance in the transition state on various metals is only 175–196 pm, which is shorter than a typical C–C distance in a transition state for C–C activation, >200 pm.<sup>165</sup> Even in the final state of the dissociation, the C–C distance is still only 224–237 pm, which is much shorter than the distance between the

dissociated C centers in the final state of the reaction from a tri-dehydrogenated intermediate, ~300 pm. Thus, the activation barrier of C–C breaking in a tetra-dehydrogenated intermediate, both with a flatter potential energy surface and a shorter reaction path, should be lower than that of C–C breaking in a tri-dehydrogenated intermediate. In this context, it is worth mentioning that the structure of an fcc lattice with interatomic distances suitable for optimal accommodation of neighboring carbon atoms on selected Pt group metals has been suggested by some researchers<sup>166</sup> to be crucial for the catalytic activity toward the ring-opening of MCP or other substituted cyclopentanes.

On M(211), the C–C bond breaking barriers of the tri-dehydrogenated intermediates, are lower than those on M(111). This reaction occurs at a terrace edge of M(211). The coordination number of the edge metal atoms is only 7, thus lower than the coordination number of metal atoms at (111) terraces, 9. In the initial states, tri-dehydrogenated intermediates on M(211) are 4–10 kJ mol<sup>-1</sup> less stable than those adsorbed on M(111), as shown in Fig. 4.20b. In the transition states, the terminal C atom with the methyl group on it, moves to a step-edge top site on M(211), where it builds one C–M interaction. Due to free bonding capacities, the edge metal atom interacts stronger with the unsaturated C center, with some degree of  $\pi$  bonding, which further stabilizes the transition state (Fig. 4.20b); therefore, the barrier of this reaction is low on M(211). Indeed, the interaction between the dissociated C and the edge metal atom is so strong that in the final state, the C center is still adsorbed at this top site in sp<sup>2</sup> hybridized fashion on M(211), while on the M(111) terrace, it moves further to a bridge site where it binds in sp<sup>3</sup> hybridized fashion. For comparison, the reaction from a ||-bridge adsorbed tetra-dehydrogenated intermediate has a more stable initial state on M(211) than on M(111), by 6–21 kJ mol<sup>-1</sup>. In both cases the reactant is adsorbed at a hollow site, which on M(211) is located at a terrace edge. On Pt(211), and Ir(211), the interaction between the adsorbed C and the surface edge is very strong which, on these surfaces, even prevents the adsorbate from migrating to a  $\mu$ -bridge adsorbed mode prior to C–C cleavage. The additional stabilization of the initial states leads to relatively higher barriers compared to the analogous reactions over M(111).

On different metals, the barrier heights of the C–C bond breaking steps increase in the following order: Ir  $\approx$  Rh < Pt < Pd. This observation is consistent with the experimentally observed MCP ring-opening activities.<sup>19</sup>

#### 4.3.4 Particle size effect on the ring-opening products selectivity

In Section 4.2, it was already discussed the particle size effect of Pt-based catalysts on the selectivity of the MCP RO products. When the conversion is catalyzed by large Pt particles, a selective mechanism is operating where formation of  $n\text{Hx}$  is suppressed. In contrast, small Pt particles non-selectively break the endocyclic C–C bond yielding the statistical distribution of 2MP, 3MP and  $n\text{Hx}$ . On other metal catalysts, like Rh and Ir, particle size does not affect the relative selectivity toward the three RO products. It has been observed that the branched 2MP and 3MP are always selectively produced no matter how large the metal particles are.

In this section, the particle size effect on the relative selectivity of the RO products of Rh, Ir and Pd-based catalysts will be discussed. Similarly to the assumptions invoked above to describe Pt-based catalysts, the flat M(111) surface is used to model the terrace-rich large metal particles. Small metal particles, with more defects, are described by the stepped M(211) surfaces.

**Rh-based catalyst:** Previous studies showed that the particle size did not affect the RO selectivity on Rh-based catalysts, where MCP RO always tends to produce selectively 2MP and 3MP. For example, Del Angel et al.<sup>167</sup> studied the particle size effect on the selectivity using silica or alumina supported Rh catalyst. In most cases, with Rh weight loading between 0.11 wt % and 1.4 wt %, the selectivity to  $n\text{Hx}$  was less than 4.5%. Only in two cases, with well-dispersed Rh (dispersion > 75%) on alumina, the selectivity toward  $n\text{Hx}$  could be increased to 8.9–9.3%, which is still much lower than the statistical ratio, 40%. The ratio of the other two products, 2MP and 3MP is between 1.9:1 and 2.9:1 in all tested systems, close to the ratio 2:1 which corresponds to an equal probability to break the endocyclic bisecundary C–C bonds. A later study by Teschner et al. covered a wider<sup>168</sup> range of Rh loadings, 0.3%, 3% and 10%, where the metal catalyst is supported on alumina. The selectivity toward  $n\text{Hx}$  is close to 10% in all cases of different Rh loadings. A recent study by Samoila et al.<sup>19</sup> using 0.6% wt loaded Rh also reported a similar selectivity toward  $n\text{Hx}$ , 7%–8%, at different reaction temperatures.

Coming back to the discussion of the calculated reaction landscapes, the barriers for the first dehydrogenation step and the C–C bond breaking step calculated in Sections 4.3.1 and 4.3.2 I shall now analyze in the context of experimental studies. Since the barriers for the

hydrogenation / dehydrogenation reactions are similar on the reaction path to the three isomeric hexanes, the discussion focuses on the C–C bond breaking steps. On the reaction path to 3MP, the calculated C–C bond breaking barrier is as low as 16 kJ mol<sup>-1</sup> on Rh(111) and 46 kJ mol<sup>-1</sup> (including migration) on Rh(211). However, on the reaction path to *n*Hx, the C–C bond breaking barriers, 70 kJ mol<sup>-1</sup> on Rh(111) and 59 kJ mol<sup>-1</sup> on Rh(211), are at least 13 kJ mol<sup>-1</sup> higher than on the path to 3MP. Therefore, both at terrace and step sites, the production of *n*Hx is depressed due to the substantially higher barrier of the C–C bond breaking, which well explains several experimental observations mentioned above.

***Ir-based catalyst:*** Similar to Rh, the distribution of the three RO products is not much influenced by the particle size of Ir catalysts. On large Ir particles, e.g. 10 wt % Ir supported by alumina, the ratio of 2MP, 3MP and *n*Hx was 64:32:3.<sup>169</sup> A more recent study by Samoila et al.<sup>19</sup> reported 3%–5% selectivity toward *n*Hx, with the ratio 2MP : 3MP close to 2:1.

First, the discussion is focused on large Ir particles. According to the calculated barriers reported in Sections 4.3.1 and 4.3.2, the reaction pathway to 3MP on Ir(111) contains a migration step with a barrier of 41 kJ mol<sup>-1</sup>; the following C–C bond breaking step has a barrier of 17 kJ mol<sup>-1</sup>. A higher C–C bond breaking barrier, 62 kJ mol<sup>-1</sup>, was calculated for the path to *n*Hx on Ir(111). This barrier is at least 21 kJ mol<sup>-1</sup> higher than that on the way to 3MP. Just like on Pt(111) and Rh(111) discussed above, the higher C–C bond breaking barrier on the way to *n*Hx over Ir(111) decreases the rate of formation of *n*Hx on (111) terraces, and, hence, the selectivity toward *n*Hx is lower than the statistical ratio on large Ir particles, which possess a large net surface area of flat facets.

On Ir(211), the situation is reversed. The calculated C–C bond breaking barrier on the way to *n*Hx decreases to 38 kJ mol<sup>-1</sup>, which is 13 kJ mol<sup>-1</sup> lower than the C–C bond breaking barrier on the way to 3MP. Moreover, it is also comparable with the barrier for the migration step in the reaction path to 3MP on Ir(111), which at first glance suggests that the formation of *n*Hx should be easier than of 3MP on Ir(211) and on small Ir particles. However, the ||-bridge adsorbed intermediate, which adsorbs quite strongly at sites close to step edges, probably blocks most of the near-edge hollow sites, required to accommodate the tri-dehydrogenated *n*Hx precursor, due to the high exit barriers for further conversion of the former: either via the direct C–C bond scission which has a barrier of 89 kJ mol<sup>-1</sup>, or a migration to a terrace three-fold site via a  $\mu$ -bridge which requires to surmount a barrier of 66 kJ mol<sup>-1</sup>, whereas the barrier for reverse migration is only 0.5 kJ mol<sup>-1</sup>. Thus, the production

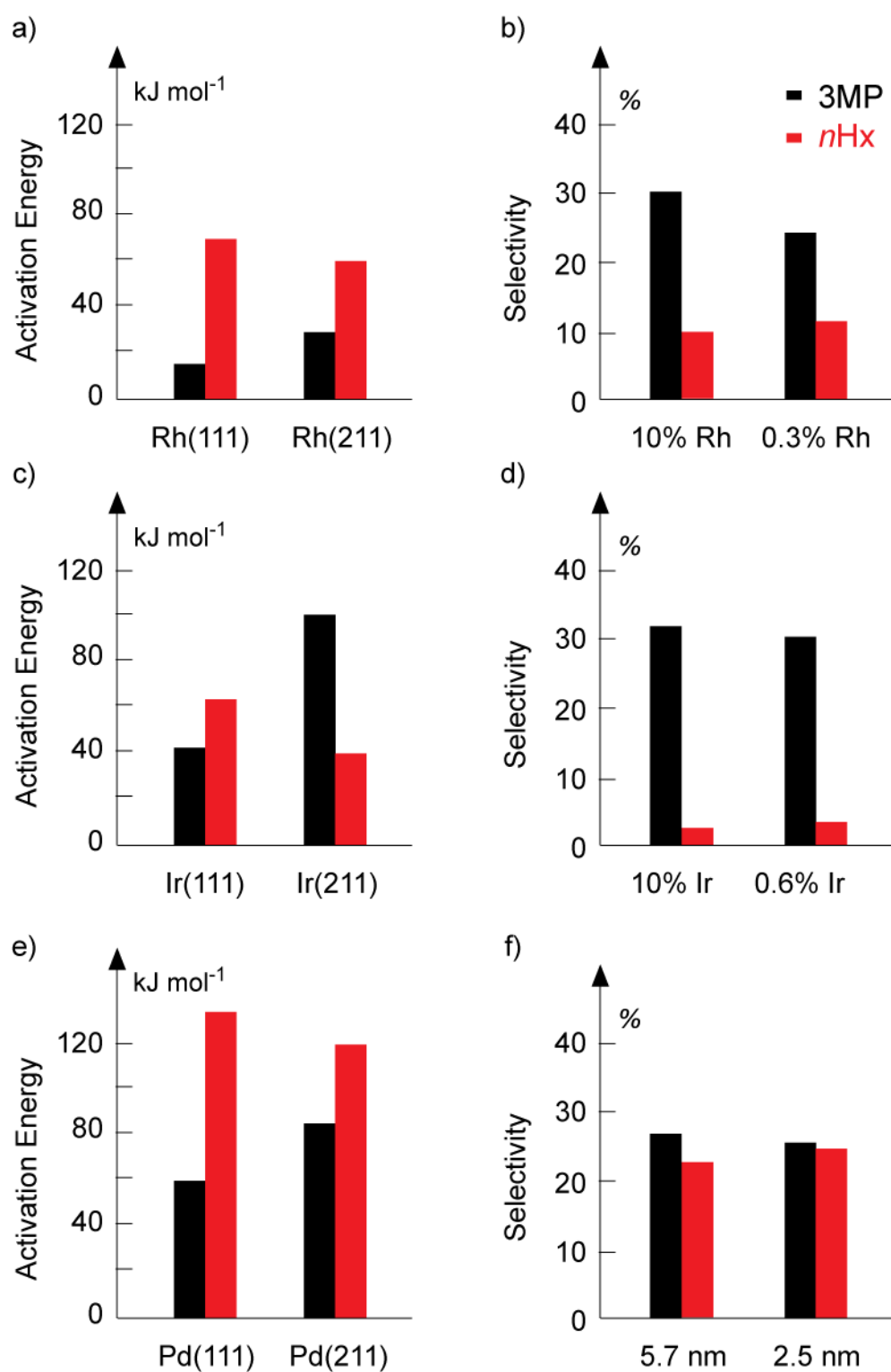


**Figure 4.21.** Calculated barrier heights of the C–C bond breaking step or migration step on flat and stepped surfaces of a) Rh; c) Ir and e) Pd. Experimental selectivity toward 3MP and *n*Hx catalyzed by b) supported Rh particles (Ref 168); c) supported Ir particles (Ref 19, 169) and d) supported Pd particles (Ref 137).

of  $n\text{Hx}$  is still depressed on small particles.

***Pd-based catalyst:*** Finally, the discussion returns of Pd-based catalysts. There are not as many published studies on the performance of Pd-based catalysts for MCP RO as on Pt-, Rh-, and Ir-based ones due to the relatively low activity of the former. A series of Pd/Al<sub>2</sub>O<sub>3</sub> catalysts, with Pd diameter between 1.5 and 12 nm, were prepared by Le Normand et al.<sup>137</sup> The reported selectivity toward the RO products was similar in all cases, with a factor of two decreased selectivity toward  $n\text{Hx}$ , between 18% and 24.5% compared to the statistical ratio, 40%. The ratio of 2MP : 3MP was between 1.3:1 and 2.3:1, which is close to the ratio 2:1 corresponding to breakage of endocyclic bissecondary C–C bonds with equal probability.

Recall from Sections 4.3.1 and 4.3.2 that the calculated barrier for C–C bond breaking, which is combined with the reaction energy of the preceding migration step in the reaction path to 3MP, is only 70 kJ mol<sup>-1</sup> on Pd(111). This value is notably lower, by 64 kJ mol<sup>-1</sup>, than the barrier for C–C bond breaking on the way to  $n\text{Hx}$ . The latter barrier is also 44 kJ mol<sup>-1</sup> higher than the barrier of the first dehydrogenation step. Thus, the selectivity toward  $n\text{Hx}$  should be lower than statistical on large Pd particles. On the stepped Pd(211) surface, the C–C bond breaking barrier on the way to  $n\text{Hx}$  is still very high, 119 kJ mol<sup>-1</sup>, which is 34 kJ mol<sup>-1</sup> higher than the barrier of the same step on the reaction pathway to 3MP. Therefore, similar to the reaction on Pd(111), the formation of  $n\text{Hx}$  is predicted to be slower than that of 3MP on Pd(211), and hence, the selectivity toward  $n\text{Hx}$  is expected to be lower than statistical on small Pd particles. However, according to the present calculations, the yield of  $n\text{Hx}$  cannot be as high as 25% due to at least 34 kJ mol<sup>-1</sup> higher activation barriers on the way to  $n\text{Hx}$  than those on the way to 3MP. Other side reactions could lead to the increased selectivity toward  $n\text{Hx}$ . For example, the formation of  $n\text{Hx}$  was reported to be significantly enhanced from ~20% to ~40% when the acidity of the Pd/Al<sub>2</sub>O<sub>3</sub> was increased via a pretreatment,<sup>170</sup> which indicates the similar activity of the sites on Pd metals and on acid support. On the more active metals considered above, the ring-opening directly on the acidic support does not take place to a large extent since the reaction proceeds much faster on metal particles.

#### 4.3.5 Final comments on the particle size effect

In Sections 4.2.5 and 4.3.4, the particle size dependence of the MCP RO product distribution was rationalized on various supported metal particle catalysts. Current calculations focused on the dissociative mechanism, similar to that proposed by Gault et

al.<sup>117,123</sup> (Fig. 4.2). The particle size effect is attributed to the different C–C bond breaking barriers on terrace and step sites of the metal particles.

In this thesis, the proposed mechanism successfully explained the particle size effect of Pt-, Rh- and Ir-based catalysts. However, it does not fully rationalize the experimental observations on Pd. There could be several reasons for this disagreement; the most likely ones can be summarized as follows. Among several suggested mechanisms outlined in Section 4.1.1, on the basis of the activation barriers calculated on Pt(111), preference was given to the “dissociative” mechanism in which a deep dehydrogenation of two neighboring C centers is required before ring cleavage. The same process is also assumed to be active on other noble metals; however, this assumption may not hold in all cases. For example, Teschner et al.<sup>171</sup>, who investigated the effect of hydrogen pressure on the MCP RO reaction over Rh catalysts, observed that RO reactions showed a positive order in the partial pressure of hydrogen, indicating that the dehydrogenation degree of the intermediate is not very deep. On Pd-based catalysts, Le Normand et al.<sup>137</sup> tried to explain the observed selectivity by invoking a mechanism via a  $\pi$ -olefin- $\sigma$ -alkyl 1,2-5 intermediate, in which only one dehydrogenation step precedes C–C bond breaking. According to this mechanism, a statistical distribution should be 2MP : 3MP :  $n$ Hx = 2:1:1, which is quite close to their experimental observations.

Another factor that could influence the selectivity of RO reactions is the catalyst support. For example, Kramer and Zuegg<sup>172</sup> reported that the selectivity toward  $n$ Hx was slightly increased at a phase boundary between Pt metal particle and the alumina support. A more important factor to affect the selectivity is the acidity of the support. For example, using differently pretreated catalysts, Łomot et al.<sup>170</sup> reported that the selectivity toward  $n$ Hx increased significantly from ~20% to ~40% with increasing Lewis acidity of the Pd/Al<sub>2</sub>O<sub>3</sub> samples. However, other reactions, like ring enlargement or aromatization, were simultaneously enhanced, with the net SRO selectivity (opening of endocyclic bonds) decreasing from ~90% to ~50%.

Another possible limitation of the current computational model is that only one coverage, 1/9, was considered, assuming weakly interacting adsorbates. In the discussion on ethylene transformations in Chapter 3 of this thesis, it was already shown that the activation energy of a hydrogenation / dehydrogenation reaction can change by 25 kJ mol<sup>-1</sup> while decreasing the coverage from 1/3 to 1/9 due to the changing of the absolute coverage, i.e. with / without co-adsorbed H atom on the surface. Experimentally, the MCP RO reaction is

performed in the presence of an excess of H<sub>2</sub>. Thus, at experimental conditions the surface is expected to be saturated with the H atoms and the barrier heights of those reactions, where the number of occupied adsorption sites changes during the reaction, can significantly differ from those calculated at 1/9 coverage. A better way to study coverage effects uses kinetic Monte Carlo simulations based on current DFT calculated barriers.

#### 4.4. Summary

In this chapter, methylcyclopentane ring-opening reactions were studied computationally. The selectivity toward the ring-opening products 2-methylpentane (2MP), 3-methylpentane (3MP), and *n*-hexane (*n*Hx) on the four metals Pt, Rh, Ir and Pd were discussed. In the reaction network considered, the conversion entailed three major steps: (i) dehydrogenation reactions to form an  $\alpha\alpha\beta\beta$ -tetra-dehydrogenated cyclic intermediate (as suggested by Maire et al.<sup>123</sup>) or an  $\alpha\alpha\beta$ -tri-dehydrogenated cyclic intermediate, (ii) endocyclic C–C bond breaking, and (iii) rehydrogenation to form saturated C6 hexanes. On Pt-based catalysts, a C–C cleavage in an  $\alpha\gamma$ -di-dehydrogenated intermediate was also considered as an alternative reaction route of the C–C bond breaking step on small particles (as suggested by Gault<sup>117</sup>). On the Pt(111) surface, all elementary steps of the MCP RO reaction were calculated according to the mechanism shown in Fig 4.2. On other metal surfaces, I mainly focused on the C–C bond breaking step because it is considered important for the relative selectivity toward various RO products. Along with the C–C bond breaking step, also the first dehydrogenation step on all metal surfaces under scrutiny was also computationally characterized, to estimate an upper bound of the dehydrogenation barriers on the metal surfaces of interest.

On the Pt(111) surface, the barriers for the hydrogenation / dehydrogenation reactions mainly fall in the range 60–90 kJ mol<sup>-1</sup>. The activation barriers for the same dehydrogenation / hydrogenation step on the way to different RO products have a similar height. The barrier for the C–C bond breaking step on the reaction pathway to *n*Hx, 116 kJ mol<sup>-1</sup>, is higher than on the way to 2MP or 3MP, only 74–75 kJ mol<sup>-1</sup>. The relative barrier heights are reversed on the stepped Pt surface, with a low barrier at 79 kJ mol<sup>-1</sup> on the way to *n*Hx and high barriers at 98–102 kJ mol<sup>-1</sup> on the way to 2MP or 3MP.

On the four calculated M(111) surfaces, the dehydrogenation barrier heights follow the order Ir < Rh < Pt < Pd from 79 kJ mol<sup>-1</sup> to 92 kJ mol<sup>-1</sup>. Slightly lower barriers are obtained

on M(211), between  $35 \text{ kJ mol}^{-1}$  and  $60 \text{ kJ mol}^{-1}$ , increasing in the same order as on M(111). Similar to the results calculated on Pt surfaces, a stronger variation of barrier heights is obtained for the C–C bond breaking steps. The C–C bond breaking barriers are between  $11 \text{ kJ mol}^{-1}$  and  $75 \text{ kJ mol}^{-1}$  on M(111) and  $27\text{--}102 \text{ kJ mol}^{-1}$  on M(211) on the reaction path to 3MP. The same step on the way to *n*Hx shows higher barriers on M(111), between  $62 \text{ kJ mol}^{-1}$  and  $134 \text{ kJ mol}^{-1}$ , and the barriers on M(211) are between  $38 \text{ kJ mol}^{-1}$  and  $119 \text{ kJ mol}^{-1}$ .

On the basis of the calculated barriers, the particle size effect on the distribution of the ring-opening products was rationalized. The flat M(111) surfaces were used to model large metal particles with extended terraces, while the stepped M(211) and Pt(322) surfaces were used to model small metal particles, which contain more low-coordinated metal atoms. Due to the similar barrier height of the same hydrogenation / dehydrogenation steps on the way to three isomeric RO products, the product distribution should not be strongly affected by these steps. Thus, the different selectivity on small and large metal particles is mainly due to the notably different barrier heights of the C–C bond breaking steps.

On Pt-based catalysts, experimental studies had shown that large Pt particles or Pt single crystals selectively produce branched 2MP and 3MP. The current calculation predicts low barriers (at most  $75 \text{ kJ mol}^{-1}$ ) for the C–C bond breaking step on Pt(111) on the way to 2MP and 3MP, which is notably lower than the barrier of the same step on the way to *n*Hx,  $116 \text{ kJ mol}^{-1}$ . In fact, the latter barrier is also higher than the barriers of all calculated elementary steps on Pt(111). Thus, this higher barrier prevents the formation of *n*Hx on Pt(111) or large Pt particles. However, the C–C cleavage barrier in the reaction pathway to *n*Hx decreases to  $94 \text{ kJ mol}^{-1}$  on Pt(211), which is lower than the C–C cleavage barrier on the way to 2MP and 3MP on the stepped Pt(211),  $\sim 100 \text{ kJ mol}^{-1}$ . Moreover, the C–C cleavage barrier of an alternative path to form only *n*Hx is as low as  $79 \text{ kJ mol}^{-1}$  on Pt(322). Therefore, a stepped surface, or small particles with more defects, should preferentially produce *n*Hx.

On Rh-based catalysts, past experiments demonstrated that the selectivity of MCP ring-opening was not strongly affected by the metal particle size. The branched products, 2MP and 3MP, were always selectively produced. Indeed, the current calculation found that the C–C bond breaking barrier on the way to 3MP is lower than the barrier on the way to *n*Hx by  $32\text{--}54 \text{ kJ mol}^{-1}$  over both Rh(111) and Rh(211) surfaces. Therefore, the production of *n*Hx is always depressed independent of the Rh-particles size.

Similarly to Rh-based catalysts, Ir particles also preferentially produce branched 2MP and 3MP. The corresponding C–C bond breaking barrier on Ir(111) is as low as 17 kJ mol<sup>-1</sup>, even lower than the previous migration step, with 41 kJ mol<sup>-1</sup> barrier. Both of them are lower than the barrier on the way to *n*Hx, which is at 62 kJ mol<sup>-1</sup> on Ir(111), indicating faster formation of 3MP than *n*Hx on Ir(111). On Ir(211), the very strongly bound tetra-dehydrogenated intermediates probably block the step-edge sites, preventing the formation of *n*Hx on such sites.

On Pd-based catalysts, the selectivity toward *n*Hx is lower than the statistical ratio (40%) but remains at a stable level of about 25% for a range of particle sizes from 1.5 nm to 12 nm. The preferential formation of 2MP and 3MP is consistent with the higher barrier of C–C bond breaking step on the way to *n*Hx, which is 35–64 kJ mol<sup>-1</sup> higher than for the same step on the way to 3MP over both Pd(111) and Pd(211). However, the current mechanism does not allow one to explain why a relatively high and stable yield of *n*Hx is obtained on Pd catalysts. Probably, other mechanisms, favoring *n*Hx formation, operate in parallel to the considered one.

Finally, it is worth mentioning that the current study took as a basis a RO mechanism that was proposed on the basis of experimental observations pertaining to MCP RO on supported Pt catalysts. The current study does not exclude a possibility that other mechanisms, including those involving the acidic support,<sup>170</sup> might work in parallel or even prevail over the current one on Rh, Ir and Pd catalysts.

## Chapter 5

### Summary of the thesis

In this thesis, I studied the conversion of hydrocarbons catalyzed by transition metals, Pt, Rh, Pd and Ir, with density functional calculations on periodic slab models. Two model systems, the conversion of ethylene to ethylidyne (Chapter 3) and the methylcyclopentane ring-opening reactions (Chapter 4), were investigated.

In Chapter 3, the discussion focused on the conversion of ethylene to ethylidyne. Two types of surface reactions, hydrogenation / dehydrogenation reactions and 1,2-H shift reactions were considered. The results of calculations revealed relatively high barriers for 1,2-H shift reactions. Thus, the work focused on three possible pathways that contain only hydrogenation / dehydrogenation reactions: (i) via vinyl and ethylidene (M1), (ii) via vinyl and vinylidene (M2), and (iii) via ethyl and ethylidene (M3). Three surface coverages, 1/3, 1/4, and 1/9, were considered. The calculated results showed that the barrier heights of all hydrogenation-dehydrogenation steps considered on Pt(111) were in the range of 19–92 kJ mol<sup>-1</sup>. The surface coverage notably affects the relative barriers of the reactions on Pt(111). A general rule is that hydrogenation barriers decrease with increasing surface coverage; dehydrogenation barriers show the opposite trend, they increase with decreasing coverage.

In the absence of coadsorbed hydrogen, mechanisms M1 and M2 compete with each other. Both reactions share the first step, the dehydrogenation of ethylene to ethylidyne, and it is the rate-determining step at high surface coverage (1/3), with a 92 kJ mol<sup>-1</sup> activation barrier. At low coverage, both mechanisms pass the highest barriers of a comparable height, ~80 kJ mol<sup>-1</sup>, for vinyl hydrogenation to ethylidene in M1 and vinylidene hydrogenation to ethylidyne in M2.

Unlike M1 and M2, mechanism M3 starts with the hydrogenation of ethylene. Thus,

pre-adsorbed hydrogen atoms are required before ethylene conversion starts. The calculated activation energies of the three elementary reactions of M3 are lower than or comparable to the rate-limiting barriers of M1 and M2. Therefore, once co-adsorbed H atoms are available, ethylene tends to be hydrogenated to ethyl, followed by the full hydrogenation to ethane, which has a comparable or lower barrier than the dehydrogenation reaction of ethyl at various coverages. Furthermore, once ethane is formed, it easily desorbs from the surface due to the very low adsorption energy of this species, which makes this reaction irreversible.

A very low barrier, only 19–29 kJ mol<sup>-1</sup>, is calculated for the ethylidene conversion to ethylidyne. Thus, the previous assignment of spectroscopic evidence to ethylidene as intermediate in the conversion of ethylene to ethylidyne conversion is questionable, due to the quick conversion of ethylidene to ethylidyne.<sup>108,109</sup> The calculated barriers suggest that vinyl or vinylidene could be accumulated on the surface, due to a relatively slow conversion rate of these two species to ethylidene or ethylidyne. The accumulation of vinylidene is further confirmed by kinetic Monte Carlo simulations.<sup>115</sup>

In Chapter 4, I discussed the conversion of methylcyclopentane (MCP) to its ring-opening products 2MP, 3MP, and *n*Hx catalyzed by supported transition-metal particles. Four metals, M = Pt, Rh, Ir and Pd, were studied. The current model of the conversion involves three major steps: dehydrogenation of MCP to a  $\alpha\alpha\beta\beta$ -tetraadsorbed or  $\alpha\alpha\beta$ -triadsorbed cyclic intermediate, endocyclic C–C bond breaking, and rehydrogenation to form saturated alkanes. On Pt-based catalysts, the reaction through an additional intermediate, the  $\alpha\gamma$ -diadsorbed intermediate, was also calculated as suggested by some researchers in the past. The M(111) surface was used to model terrace-rich large metal particles, while the M(211) or Pt(322) surfaces were used to model defect-rich small metal particles.

The transition state structures and activation energies for all pertinent elementary steps on the Pt(111) surface were calculated. The results of our calculations show that the activation energies of most considered hydrogenation–dehydrogenation steps in the reaction paths to different products fall in the range between 60 kJ mol<sup>-1</sup> and 90 kJ mol<sup>-1</sup> over the Pt(111) surface. Moreover, the activation energies of the same step on the way to three different hexanes are very close to each other. However, the barrier for the C–C bond breaking step varies from about 74–75 kJ mol<sup>-1</sup> on the way to 2MP and 3MP, which is comparable with the hydrogenation–dehydrogenation barriers, to a considerably higher barrier, 116 kJ mol<sup>-1</sup>, on

the way to *n*Hx. In line with these observations, modeling over the stepped Pt(211) and Pt(322) surfaces focused on the C–C bond breaking reactions. The barrier of the C–C bond breaking step on the way *n*Hx decreases to 79 kJ mol<sup>-1</sup> on the stepped surfaces, whereas the activation energy for the ring-opening to form 2MP and 3MP increases to more than 100 kJ mol<sup>-1</sup>.

The calculated results shed some light on the particle size dependence of the distribution of ring-opening products. Previous experimental studies observed that the branched products, 2MP and 3MP, were favored on large Pt particles or Pt single crystals. This observation is supported by the results of our calculations, which predict that the activation energies of the C–C bond breaking step on the path to 2MP and 3MP are less than 75 kJ mol<sup>-1</sup>. On the other hand, the barrier for the C–C bond breaking in the reaction path to *n*Hx, 116 kJ mol<sup>-1</sup>, is about 27 kJ mol<sup>-1</sup> higher than the barriers of all other elementary steps, including the steps on the path to 2MP and 3MP. A higher rate-limiting barrier on the path to *n*Hx explains its lower yields compared to 2MP and 3MP. However, this barrier drops to 79 kJ mol<sup>-1</sup>, on the Pt(322) surface and falls in the barrier range of the dehydrogenation–hydrogenation steps. In contrast, the C–C bond breaking barriers on the paths to 2MP and 3MP are raised to about 100 kJ mol<sup>-1</sup>, on the stepped surface. The combination of these effects explains why the product distribution becomes close to statistical on small defect-rich Pt particles.

For the other three transition metal catalysts, I only studied the C–C bond breaking step, as it was proven to be crucial for the selectivity of the ring-opening products. In addition, the first dehydrogenation step was also calculated, to get an idea of a typical barrier height for the hydrogenation / dehydrogenation reactions on different surfaces.

The results of calculations show that the barrier height of C–C scission follows the order Rh  $\approx$  Ir < Pt < Pd, which is consistent with the experimentally observed activity for ring-opening of MCP. On the basis of the calculated barriers, the particle size dependence of the selectivity to 2MP, 3MP and *n*Hx catalyzed by different metals can be rationalized as follows.

- 1) On Pt and Ir, the preferential formation of branched 2MP and 3MP on large particles is due to the high activation barrier for ring cleavage of the tri-dehydrogenated intermediate on flat (111) surfaces. On the stepped Pt surface, the barrier height for the C–C bond cleavage of the tri-dehydrogenated intermediate drops slightly below that of the tetra-

dehydrogenated MCP, consistent with the observed statistical product distribution of ring opening. On stepped Ir(211), the step edge sites are expected to be blocked by the strongly adsorbed tetra-dehydrogenated intermediate, which should suppress the formation of nHx at such sites, in accordance with the experimental observations.

- 2) On Rh and Pd, the calculated C–C scission barrier for the tetra-dehydrogenated intermediate is always lower than for the tri-dehydrogenated intermediate. Therefore, the production of 2MP and 3MP is favored irrespective of the particle size. Our results thus rationalize the experimentally reported lack of particle-size dependence for MCP ring-opening reactions on Rh and Pd catalysts and the preference for forming 2MP and 3MP.

Although the current thesis has answered some important questions on the reaction mechanisms under scrutiny, comments on several aspects are in order regarding further computational studies, especially for the MCP ring-opening reactions. *i)* The selected mechanism is mainly based on the experimental observations on Pt catalysts. The selectivity of ring-opening on the other three transition metals may be governed by other mechanisms or a combination thereof. *ii)* Kinetic simulations, either based on micro-kinetic modeling or on the kinetic Monte Carlo method, is beneficial for gaining a deeper understanding of the ring-opening process, e.g. the dependence of the selectivity on the temperature or hydrogen partial pressure, etc. *iii)* Calculations on model metal nanoparticles, with or without support, would be also desirable to investigate the effect of electronic structure and geometry of the metal nanocatalysts on the product selectivity.

## Appendix: List of Abbreviations

2MP	2-methylpentane
3MP	3-methylpentane
BE	binding energy
CN	cetane number
DFT	density functional theory
HREELS	high resolution electron energy loss spectroscopy
KS	Kohn and Sham
LEED	low-energy electron diffraction
MCP	methylcyclopentane
NEXAFS	near-edge X-ray adsorption fine structure
<i>n</i> Hx	<i>n</i> -hexane
ON	octane number
PM	particulate matter
RAIRS	reflection adsorption infrared spectroscopy
RO	ring-opening
SFG	sum frequency generation
SRO	selectively ring-opening
TS	transition state (structure)
UHV	ultra high vacuum
<i>wt</i>	weight

## References

- <sup>1</sup> Borken, J.; Briggs, D.; Forsberg, B.; Gulliver, J.; Heinrich, J.; Janssen, N.; Jantunen, M.; Jobson, E.; Keuken, M.; Krasenbrink, A.; Krzyzanowski, M.; Kuna-Dibbert, B.; Martini, G.; Medina, S.; Momas, I.; Ntziachristos, L.; Samaras, Z.; Sanderson, E.; Schneider, J.; Schwarze, P. E.; Šrám, R. J.; Stilianakis, N.; Svartengren, M.; van Aalst, R.; Wass, U.; *Health effects of transport-related air pollution*, M. Krzyzanowski, B. Kuna-Dibbert, J. Schneider, eds. World health organization, Copenhagen, **2005**.
- <sup>2</sup> Stanislaus, A.; Cooper, B. H. *Catal. Rev. –Sci. Eng.* **1994**, *36*, 75.
- <sup>3</sup> Scherzer, J.; Gruia, A. J. *Hydrocracking Science and Technology*, Marcel Dekker: New York, **1996**.
- <sup>4</sup> Pallassana, V.; Neurock, M. *J. Catal.* **2000**, *191*, 301.
- <sup>5</sup> Neurock, M.; van Santen, R. A. *J. Phys. Chem. B* **2000**, *104*, 11127.
- <sup>6</sup> Jones, G.; Jakobsen, J. G.; Shim, S. S.; Kleis, J.; Andersson, M. P.; Rossmeisl, J.; Abild-Pedersen, F.; Bligaard, T.; Helveg, S.; Hinnemann, B.; Rostrup-Nielsen, J. R.; Chorkendorff, I.; Sehested, J.; Nørskov, J. K. *J. Catal.* **2008**, *259*, 147.
- <sup>7</sup> Joubert, J.; Delbecq, F.; Sautet, P.; Le Roux, E.; Taoufik, M.; Thieuleux, C.; Blanc, F.; Coperet, C.; Thivolle-Cazat, J.; Basset, J.-M. *J. Am. Chem. Soc.* **2006**, *128*, 9157.
- <sup>8</sup> Greeley, J.; Mavrikakis, M. *J. Am. Chem. Soc.* **2004**, *126*, 3910.
- <sup>9</sup> Steininger, H.; Ibach, H.; Lehwald, S. *Surf. Sci.* **1982**, *117*, 685.
- <sup>10</sup> Cassuto, A.; Mane, M.; Jupille, J. *Surf. Sci.* **1991**, *249*, 8.
- <sup>11</sup> Cassuto, A.; Kiss, J.; White, J. M. *Surf. Sci.* **1991**, *255*, 289.
- <sup>12</sup> Stöhr, J.; Sette, F.; Johnson, A. L. *Phys. Rev. Lett.* **1984**, *53*, 1684.
- <sup>13</sup> Koestner, R. J.; Stöhr, J.; Gland, J. L.; Horsley, J. A. *Chem. Phys. Lett.* **1984**, *105*, 332.
- <sup>14</sup> Cremer, P. S.; Somorjai, G. A. *J. Chem. Soc., Faraday Trans.* **1995**, *91*, 3671.
- <sup>15</sup> Hugenschmidt, M. B.; Dolle, P.; Jupille, J.; Cassuto, A. *J. Vac. Sci. Technol. A* **1989**, *7*, 3312.
- <sup>16</sup> Kubota, J.; Ichihara, S.; Kondo, J. N.; Domen, K.; Hirose, C. *Surf. Sci.* **1996**, *357-358*, 634.
- <sup>17</sup> Kesmodel, L. L.; Dubois, L. H.; Somorjai, G. A. *J. Chem. Phys.* **1979**, *70*, 2180.
- <sup>18</sup> Gyórfy, N.; Bakos, I.; Szabó, S.; Tóth, L.; Wild, U.; Schlögl, R.; Paál, Z. *J. Catal.* **2009**, *263*, 372.
- <sup>19</sup> Samoila, P.; Boutzeloit, M.; Especel, C.; Epron, F.; Marécot, P. *Appl. Catal. A* **2009**, *369*, 104.
- <sup>20</sup> Wang, Z.; Nelson, A. E. *Catal. Lett.* **2008**, *123*, 226.
- <sup>21</sup> Chimentão, R. J.; Valença, G. P.; Medina, F.; Pérez-Ramírez, J. *Appl. Surf. Sci.* **2007**, *253*, 5888.

- 22 Györfly, N.; Wootsch, A.; Szabó, S.; Bakos, I.; Tóth, L.; Paál, Z. *Top. Catal.* **2007**, *46*, 57.
- 23 Parr, R. G.; Yang, W. *Density-Functional Theory of Atoms and Molecules*. New York: Oxford University Press. **1989**.
- 24 Thomas, L. H. *Proc. Cambridge Phil. Soc.* **1927**, *23*, 542.
- 25 Fermi, E. *Rend. Accad. Naz. Lincei* **1927**, *6*, 602.
- 26 Hohenberg, P.; Kohn W. *Phys. Rev. B* **1964**, *136*, 864.
- 27 Kohn, W.; Sham, L. J. *Phys. Rev. A* **1965**, *140*, 1133.
- 28 Kresse, G.; Hafner, J. *Phys. Rev. B* **1994**, *49*, 14251.
- 29 Kresse, G.; Furthmüller, J. *Comput. Mater. Sci.* **1996**, *6*, 15.
- 30 Perdew, J. P.; Wang, Y. *Phys. Rev. B* **1992**, *45*, 13244.
- 31 Blöchl, P. E. *Phys. Rev. B* **1994**, *50*, 17953.
- 32 Kresse, G.; Joubert, D. *Phys. Rev. B* **1999**, *59*, 1758.
- 33 Monkhorst, H. J.; Pack, J. D. *Phys. Rev. B* **1976**, *13*, 5188.
- 34 Methfessel, M.; Paxton, A. T. *Phys. Rev. B* **1989**, *40*, 3616.
- 35 Blöchl, P. E.; Jepsen, O.; Andersen, O. K. *Phys. Rev. B* **1994**, *49*, 16223.
- 36 Sutton, P. W.; Dahl L. F. *J. Am. Chem. Soc.* **1967**, *89*, 261.
- 37 Motyl, K. M.; Norton, J. R.; Schauer, C. K.; Anderson, O. P. *J. Am. Chem. Soc.* **1982**, *104*, 7325
- 38 Orpen, A. G.; Rivera, A. V.; Bryan, E. G.; Pippard, D.; Sheldrick, G. M. *J. Chem. Soc., Chem. Commun.* **1978**, 723.
- 39 Henkelman, G.; Jónsson, H. *J. Chem. Phys.* **1999**, *111*, 7010.
- 40 Mills, G.; Jónsson, H.; Schenter, G. K. *Surf. Sci.* **1995**, *324*, 305.
- 41 Jónsson, H.; Mills, G.; Jacobsen, K.W. In *Classical and Quantum Dynamics in Condensed Phase Simulations*; Berne, B. J., Ciccotti, G., Coker, D. F., Eds.; World Scientific: Singapore, **1998**; p. 385.
- 42 Conti, J.; Holtberg, P. *International Energy Outlook 2011*, U.S. Energy Information Administration, **2011**.
- 43 Wilson, J.; Guo, H.; Morales, R.; Podgornov, E.; Lee, I.; Zaera, F. *Phys. Chem. Chem. Phys.* **2007**, *9*, 3830.
- 44 Somorjai, G. A.; Contreras, A. M.; Montano, M.; Rioux, R. M. *PNAS*, **2006**, *103*, 10577.
- 45 Vincent, R. S.; Lindstedt, R. P.; Malik, N. A.; Reid, I. A. B.; Messenger, B. E. *J. Catal.* **2008**, *260*, 37.
- 46 Essen, J. M.; Haubrich, J.; Becker, C.; Wandelt, K. *Surf. Sci.* **2007**, *601*, 3472.
- 47 Nieminen, V.; Honkala, K.; Taskinen, A.; Murzin D. Y. *J. Phys. Chem. C* **2008**, *112*, 6822.
- 48 Jacob, T.; Goddard III, W. A. *J. Phys. Chem. B* **2005**, *109*, 297.
- 49 Watwe, R. M.; Cortright, R. D.; Mavrikakis, M.; Nørskov, J. K.; Dumesic, J. A. *J. Chem. Phys.* **2001**, *114*, 4663.
- 50 Watson, G. W.; Wells, R. P. K.; Willock, D. J.; Hutchings, G. J. *J. Phys. Chem. B* **2000**, *104*, 6439.

- 51 Watwe, R. M.; Cortright, R. D.; Nørskov, J. K.; Dumesic, J. A. *J. Phys. Chem. B* **2000**, *104*, 2299.
- 52 Ge, Q.; King, D. A. *J. Chem. Phys.* **1999**, *110*, 4699.
- 53 Hirschl, R.; Eichler, A.; Hafner, J. *J. Catal.* **2004**, *226*, 273.
- 54 Kua, J.; Goddard III, W. A. *J. Phys. Chem. B* **1998**, *102*, 9492
- 55 Koestner, R. J.; Van Hove, M. A.; Somorjai, G. A. *Surf. Sci.* **1982**, *121*, 321.
- 56 Kesmodel, L. L.; Gates, J. A. *Surf. Sci.* **1981**, *111*, L747.
- 57 Marinova, Ts.; Kostov, K. L. *Surf. Sci.* **1987**, *181*, 573.
- 58 Hills, M. M.; Parmeter, J. E.; Mullins, C. B.; Weinberg, W. H.; *J. Am. Chem. Soc.* **1986**, *108*, 3554.
- 59 Somorjai, G. A.; Van Hove, M. A.; Bent, B. E. *J. Phys. Chem.* **1988**, *92*, 973.
- 60 Zaera, F. *J. Am. Chem. Soc.* **1989**, *111*, 4240.
- 61 Ditlevsen, P. D.; Van Hove, M. A.; Somorjai, G. A. *Surf. Sci.* **1993**, *292*, 267.
- 62 Cremer, P.; Stanners, C.; Niemantsverdriet, J. W.; Shen, Y. R.; Somorjai, G. *Surf. Sci.* **1995**, *328*, 111.
- 63 Deng, R.; Herceg, E.; Trenary, M. *Surf. Sci.* **2004**, *560*, L195.
- 64 Moskaleva, L. V.; Chen, Z. X.; Aleksandrov, H. A.; Mohammed, A. B.; Sun, Q.; Rösch, N. *J. Phys. Chem. C* **2009**, *113*, 2512.
- 65 Moskaleva, L. V.; Aleksandrov, H. A.; Basaran, D.; Zhao, Z.-J.; Rösch, N. *J. Phys. Chem. C* **2009**, *113*, 15373.
- 66 Zaera, F. *J. Am. Chem. Soc.* **1989**, *111*, 8744.
- 67 Zaera, F. *Surf. Sci.* **1989**, *219*, 453.
- 68 Zaera, F.; Bernstein, N. *J. Am. Chem. Soc.* **1994**, *116*, 4881.
- 69 Zaera, F. *Langmuir*, **1996**, *12*, 88.
- 70 Zaera, F.; French, C. R. *J. Am. Chem. Soc.* **1999**, *121*, 2236.
- 71 Zaera, F.; Janssens, T. V. W.; Öfner, H. *Surf. Sci.* **1996**, *368*, 371.
- 72 Anghel, A. T.; Wales, D. J.; Jenkins, S. J.; King, D. A. *Chem. Phys. Lett.* **2005**, *413*, 289.
- 73 Anghel, A. T.; Wales, D. J.; Jenkins, S. J.; King, D. A. *J. Chem. Phys.* **2007**, *126*, 044710.
- 74 Döll, R.; Gerken, C. A.; Van Hove, M. A.; Somorjai, G. A. *Surf. Sci.* **1997**, *374*, 151.
- 75 Cremer, P. S.; Su, X. C.; Shen, Y. R.; Somorjai, G. A. *J. Am. Chem. Soc.* **1996**, *118*, 2942.
- 76 Windham, R. G.; Bartram, M. E.; Koel, B. E. *J. Phys. Chem.* **1988**, *92*, 2862.
- 77 Stacchiola, D.; Azad, S.; Burkholder, L.; Tysoe, W. T. *J. Phys. Chem. B.* **2001**, *105*, 11233.
- 78 Hammer, B.; Hansen, L. B.; Nørskov, J. K. *Phys. Rev. B* **1999**, *59*, 7413.
- 79 Kesmodel, L. L.; Dubois, L. H.; Somorjai, G. A. *Chem. Phys. Lett.* **1978**, *56*, 267.
- 80 Starke, U.; Barbieri, A.; Materer, N.; Van Hove, M. A.; Somorjai, G. A. *Surf. Sci.* **1993**, *286*, 1.
- 81 Yeo, Y. Y.; Stuck, A.; Wartnaby, C. E.; King, D. A. *Chem. Phys. Lett.* **1996**, *259*, 28.

- 82 Natal-Santiago, M. A.; Podkolzin, S. G.; Cortright, R. D.; Dumesic, J. A. *Catal. Lett.* **1997**, *45*, 155.
- 83 Shen, J. Y.; Hill, J. M.; Watwe, R. M.; Spiewak, B. E.; Dumesic, J. A. *J. Phys. Chem. B* **1999**, *103*, 3923.
- 84 Ford, D. C.; Xu, Y.; Mavrikakis, M. *Surf. Sci.* **2005**, *587*, 159.
- 85 Janssens, T. V. W.; Zaera, F. *J. Phys. Chem.* **1996**, *100*, 14118.
- 86 Ogle, K. M.; Creighton, J. R.; Akhter, S.; White, J. M. *Surf. Sci.* **1986**, *169*, 246.
- 87 Erley, W.; Li, Y.; Land, D. P.; Hemminger, J. C. *Surf. Sci.* **1994**, *301*, 177.
- 88 Godbey, D.; Zaera, F.; Yeates, R.; Somorjai, G. A. *Surf. Sci.* **1986**, *167*, 150.
- 89 Öfner, H.; Zaera, F. *J. Phys. Chem. B* **1997**, *101*, 396.
- 90 Ko, M. K.; Frei, H. *J. Phys. Chem. B* **2004**, *108*, 1805.
- 91 Wasylenko, W.; Frei, H. *J. Phys. Chem. B* **2005**, *109*, 16873.
- 92 kMC paper, need to be added.
- 93 Zaera, F. *Chem. Rev.* **1995**, *95*, 2651.
- 94 Anson, C. E.; Sheppard, N.; Bender, B. R.; Norton, J. R. *J. Am. Chem. Soc.* **1999**, *121*, 529.
- 95 Ibach, H.; Lehwald, S. *J. Vac. Sci. Technol.* **1978**, *15*, 407.
- 96 Dwivedi, Y.; Rai, S. B. *Vib. Spectrosc.* **2009**, *49*, 278.
- 97 Perez-Delgado, Y.; Lewis, E. K.; Moehnke, C. J.; Salazar, M. C.; Hernandez, A. J.; Manzanares, C. E. *Mol. Phys.* **2009**, *107*, 1367.
- 98 Alparone, A. *Chem. Phys.* **2006**, *327*, 127, and references therein.
- 99 Fan, J.; Trenary, M. *Langmuir*, **1994**, *10*, 3649
- 100 Malik, I. J.; Brubaker, M. E.; Mohsin, S. B.; Trenary, M. *J. Chem. Phys.* **1987**, *87*, 5554.
- 101 Deng, R. P.; Jones, J.; Trenary, M. *J. Phys. Chem. C* **2007**, *111*, 1459.
- 102 Parker, S. F.; Marsh, N. A.; Camus, L. M.; Whittlesey, M. K.; Jayasooriya, U. A.; Kearley, G. J. *J. Phys. Chem. A* **2002**, *106*, 5797.
- 103 Skinner, P.; Howard, M. W.; Oxtton, I. A.; Kettle, S. F. A.; Powell, D. B.; Sheppard, N. *J. Chem. Soc., Faraday Trans. 2*, 1981, 77, 1203.
- 104 Anson, C. E.; Johnson, B. F. G.; Lewis, J.; Powell, D. B.; Sheppard, N.; Bhattacharyya, A. K.; Bender, B. R.; Bullock, R. M.; Hembre, R. T.; Norton, J. R. *J. Chem. Soc., Chem. Commun.* 1989, 703
- 105 Andrews, J. R.; Kettle, S. F. A.; Powell, D. B.; Sheppard, N. *Inorg. Chem.* **1982**, *21*, 2874
- 106 Evans, J.; McNulty, G. S. *J. Chem. Soc. Dalton Trans.* **1983**, *4*, 639.
- 107 Rechien, W.; Kirchner, B.; Janetzko, F.; Bredow, T. *J. Phys. Chem. C*, **2009**, *113*, 10541.
- 108 Obtained with an estimate of the life time,  $\tau (s) = 10^{-13} \times [(\varepsilon - \varepsilon^*)/\varepsilon]^{1-s}$ , from RRK theory (see Ref. 109) where  $\varepsilon$  is the total internal energy available to the intermediate and  $\varepsilon^*$  is the activation energy,  $s$  is the number of active vibrational modes. In the present case, take  $\varepsilon$  to be equal to the reverse barrier of reaction  $e$ , from ethylidene to vinyl. At least this energy should be available to the newly formed intermediate. For 1/9 coverage, one has  $\varepsilon \geq 60$  kJ/mol,  $\varepsilon^* = 20$  kJ/mol,  $s \leq 12$ . Therefore  $\tau < 1$  ps.
- 109 Laidler, K.J. *Chemical Kinetics*; 3rd ed.; Harper & Row: New York, **1987**, pp. 157.

- 110 Liu, Z.-M.; Zhou, X.-L.; Buchanan, D. A.; Kiss, J.; White, J. M. *J. Am. Chem. Soc.* **1992**, *114*, 2031.
- 111 Cremer, P. S.; Su, X. C.; Shen, Y. R. Somorjai, G. A. *J. Phys. Chem. B* **1997**, *101*, 6474.
- 112 Hsiao, G. S.; Erley, W.; Ibach, H. *Surf. Sci.* **1998**, *396*, 422.
- 113 Anson, C. E.; Sheppard, N.; Powell, D. B.; Norton, J. R.; Fischer, W.; Keiter, R. L.; Johnson, B. F. G.; Lewis, J. Bhattacharrya, A. K.; Knox, S. A. R. Turner, M. L. *J. Am. Chem. Soc.* **1994**, *116*, 3058.
- 114 Valcárcel, A.; Ricart, J. M.; Closet, A.; Illas, F.; Markovits, A.; Minot, C. *J. Catal.* **2006**, *241*, 115.
- 115 Aleksandrov, H. A.; Moskaleva, L. V.; Zhao, Z.-J.; Basaran, D.; Chen, Z.-X.; Mei, D.-H.; Rösch, N. *J. Catal.* **2012**, *285*, 187.
- 116 Du, H.; Fairbridge, C.; Yang, H.; Ring, Z. *Appl. Catal. A* **2005**, *294* 1.
- 117 Gault, F. G.; *Adv. Catal.* **1981**, *30*, 1.
- 118 Hagedorn, C. J.; Weiss, M. J.; Kim, T. W.; Weinberg, W. H. *J. Am. Chem. Soc.* **2001**, *123*, 929.
- 119 Do, P. T.; Alvarez, E.; Resasco, D. E. *J. Catal.* **2006**, *238*, 477.
- 120 Kalakkad, D.; Anderson, S. L.; Logan, A. D.; Pena, J.; Braunschweig, E. J.; Peden, C. H. F.; Datye, A. K. *J. Phys. Chem.* **1993**, *97*, 1437.
- 121 Weisz, P. B.; Swegler, E. W. *Science* **1957**, *126*, 31.
- 122 Roessner, F.; Roland, U. *J. Mol. Catal. A* **1996**, *112* 401.
- 123 Maire, G.; Plouidy, G.; Prudhomme, J. C.; Gault, F. G. *J. Catal.* **1965**, *4*, 556.
- 124 Kramer, R.; Zuegg, H. *J. Catal.* **1984**, *85*, 530.
- 125 Garin, F.; Aeiyaich, S.; Legare, P.; Maire, G. *J. Catal.* **1982**, *77*, 323.
- 126 Zaera, F.; Godbey, D.; Somorjai, G. A. *J. Catal.* **1986**, *101*, 73.
- 127 McVicker, G. B.; Daage, M.; Touvelle, M. S.; Hudson, C. W.; Klein, D. P.; Baird W. C. Jr.; Cook, B. R.; Chen, J. G.; Hantzer, S.; Vaughan, D. E. W.; Ellis, E. S.; Feeley, O. C. *J. Catal.* **2002**, *210*, 137.
- 128 Espinosa, G.; Del Angel, G.; Barbier, J.; Bosch, P.; Lara, V.; Acosta, D. *J. Mol. Catal. A.* **2000**, *164*, 253.
- 129 Rao, R. N.; You, N.; Yoon, S.; Upare, D. P.; Park, Y.-K.; Lee, C. W.; *Catal. Lett.* **2011**, *141*, 1047.
- 130 Samoila, P.; Boutzeloit, M.; Especel, C.; Epron, F.; Marécot, P. *J. Catal.* **2010**, *276*, 237.
- 131 Teschner, D.; Pirault-Roy, L.; Naud, D.; Guérin, M.; Paál, Z. *Appl. Catal. A* **2003**, *252*, 421.
- 132 Hayek, K.; Kramer, R.; Paál, Z. *Appl. Catal. A: General* **1997**, *162*, 1.
- 133 Luck, F.; Schmitt, J. L.; Maire, G. *React. Kinet. Catal. Lett.* **1982**, *21*, 219.
- 134 Bragin, O.V. ; Liberman, A.L. *Uspekhi Khimii (Russ. Chem. Rev.)* **1970**, *39*, 21.
- 135 Anderson, J. R.; Baker, B. G. *Proc. Roy. Soc. (London)* **1963**, *A271*, 402.
- 136 Zimmer, H.; Paál, Z. *React. Kinet. Catal. Lett.* **1989**, *39*, 227.
- 137 Le Normand, F.; Kili, K.; Schmitt, J. L. *J. Catal.* **1993**, *139*, 234.
- 138 Brizuela, G.; Simonetti, S.; Pronsato, E.; Juan, A. *Surf. Sci.* **2004**, *556*, 11.

- <sup>139</sup> Simonetti, S.; Jasen, P.; Gonzalez, E.; Juan, A.; Brizuela, G. *Appl. Surf. Sci.* **2006**, *252*, 7515.
- <sup>140</sup> Comelli, N. C.; López, M. B.; Castro, E. A. *J. Mol. Struct.: THEOCHEM* **2005**, *726*, 197.
- <sup>141</sup> Becker, C.; Delbecq, F.; Breitbach, J.; Hamm, G.; Franke, D.; Jäger, F.; Wandelt, K. *J. Phys. Chem. B* **2004**, *108*, 18960.
- <sup>142</sup> Germán, E.; López-Corral, I.; Juan, A.; Brizuela, G. *J. Mol. Catal. A*, **2008**, *290*, 23.
- <sup>143</sup> Brizuela, G.; Castellani, N. *J. Mol. Catal. A* **1999**, *139*, 209.
- <sup>144</sup> Chen, Z.-X.; Aleksandrov, H. A.; Basaran, D.; Rösch, N. *J. Phys. Chem. C*, **2010**, *114*, 17683.
- <sup>145</sup> Yang, M.-L.; Zhu, Y.-A.; Fan, C.; Sui, Z.-J.; Chen, D.; Zhou, X.-G. *Phys. Chem. Chem. Phys.* **2011**, *13*, 3257.
- <sup>146</sup> Axe, F. U.; Andzelm, J. W. *J. Am. Chem. Soc.* **1999**, *121*, 5396.
- <sup>147</sup> Graham, A. P.; Menzel, A.; Toennies, J. P. *J. Chem. Phys.* **1999**, *111*, 1676.
- <sup>148</sup> Zhao, Z.-J.; Moskaleva, L. V.; Aleksandrov, H. A.; Basaran, D.; Rösch, N. *J. Phys. Chem. C* **2010**, *114*, 12190.
- <sup>149</sup> Medlin, J. W.; Allendorf, M. D. *J. Phys. Chem. B* **2003**, *107*, 217.
- <sup>150</sup> Blakely, D. W.; Somorjai, G. A. *J. Catal.* **1976**, *42*, 181.
- <sup>151</sup> Yudanov, I. V.; Matveev, A. V.; Neyman, K. M.; Rösch, N. *J. Am. Chem. Soc.* **2008**, *130*, 9342.
- <sup>152</sup> Schauermaun, S.; Hoffmann, J.; Johánek, V.; Hartmann, J.; Libuda, J.; Freund, H.-J. *Angew. Chem., Int. Ed.* **2002**, *41*, 2532.
- <sup>153</sup> Lundwall, M. J.; McClure, S. M.; Goodman, D. W. *J. Phys. Chem. C* **2010**, *114*, 7904.
- <sup>154</sup> Honkala, K.; Hellman, A.; Remediakis, I. N.; Logadottir, A.; Carlsson, A.; Dahl, S.; Christensen, C. H.; Nørskov, J. K. *Science*, **2005**, *307*, 555.
- <sup>155</sup> Alayoglu, S.; Aliaga, C.; Sprung, C.; Somorjai, G. A. *Catal. Lett.*, **2011**, *141*, 914.
- <sup>156</sup> Basaran, D.; Aleksandrov, H. A.; Chen, Z.-X.; Zhao, Z.-J.; Rösch, N. *J. Mol. Catal. A* **2011**, *344*, 37.
- <sup>157</sup> Mavrikakis, M.; Rempel, J.; Greeley, J. *J. Chem. Phys.* **2002**, *117*, 6737.
- <sup>158</sup> Mitsui, T.; Rose, M. K.; Fomin, E.; Ogletree, D. F.; Salmeron, M. *Surf. Sci.* **2003**, *540*, 5.
- <sup>159</sup> van Grootel, P. W.; van Santen, R. A.; Hensen, E. J. M. *J. Phys. Chem. C* **2011**, *115*, 13027.
- <sup>160</sup> Xing, B.; Pang, X.-Y.; Wang, G.-C. *J. Catal.* **2011**, *282*, 74.
- <sup>161</sup> Borg, H. J.; van Hardeveld, R. M.; Niemantsverdriet, J. W. *J. Chem. Soc., Faraday Trans.* **1995**, *91*, 3679.
- <sup>162</sup> Gates, J. A.; Kesmodel, L. L. *Surf. Sci.* **1982**, *124*, 68.
- <sup>163</sup> Chen, Y.; Vlachos, D. G. *J. Phys. Chem. C* **2010**, *114*, 4973.
- <sup>164</sup> van Santen, R. A.; Neurock, M.; Shetty, S. G. *Chem. Rev.* **2010**, *110*, 2005.
- <sup>165</sup> Cheng, J.; Hu, P.; Ellis, P.; French, S.; Kelly, G.; Lok, C. M. *J. Phys. Chem. C* **2008**, *112*, 6082.
- <sup>166</sup> Paál, Z.; Tétényi, P. *Nature* **1977**, *267*, 234.
- <sup>167</sup> Del Angel, G.; Coq, B.; Dutartre, R.; Figueras, F. *J. Catal.* **1984**, *87*, 27.

- <sup>168</sup> Teschner, D.; Matusek, K.; Paál, Z. *J. Catal.* **2000**, *192*, 335.
- <sup>169</sup> Sárkány, A. *J. Chem. Soc., Faraday Trans. 1* **1989**, *85*, 1523.
- <sup>170</sup> Łomot, D.; Juszczak, W.; Karpiński, Z. *Appl. Catal. A* **1997**, *155*, 99.
- <sup>171</sup> Teschner, D.; Paál, Z.; Duprez, D. *Catal. Today* **2001**, *65*, 185.
- <sup>172</sup> Kramer, R.; Zuegg, H. *J. Catal.* **1983**, *80*, 446.